THÈSE

En vue de l'obtention du

DOCTORAT DE L'UNIVERSITÉ DE TOULOUSE

Délivré par :

Institut National Polytechnique de Toulouse (Toulouse INP)

Discipline ou spécialité :

Dynamique des fluides

Présentée et soutenue par :

M. MOSTAFA SULAIMAN
le vendredi 19 octobre 2018

Titre :

Etude par simulations numériques de l'effet d'une réaction chimique sur le transfert de matière dans un lit fixe de particules

Ecole doctorale :

Mécanique, Energétique, Génie civil, Procédés (MEGeP)

Unité de recherche :
Institut de Mécanique des Fluides de Toulouse (I.M.F.T.)

Directeur(s) de Thèse :
M. ERIC CLIMENT
M. ANTHONY WACHS

Rapporteurs :
M. JOS DERKSEN, UNIVERSITY OF ABERDEEN
M. NIELS DEEN, TECHNISCHE UNIVERSITEIT EINDHOVEN

Membre(s) du jury :
M. SERGE SIMOENS, CNRS, Président
M. ANTHONY WACHS, UNIVERSITY OF BRITISH COLUMBIA VANCOUVER, Membre
M. ERIC CLIMENT, INP TOULOUSE, Membre
M. GUILLAUME VINAY, IFPEN, Membre
Mme CARINE JULCOUR, CNRS TOULOUSE, Membre

Résumé

Mots clés : Transfert de matière, particule de catalyseur, réaction chimique, nombre de Damkohler, nombre de Sherwood, Sharp Interface Method, simulation numérique.

Nous avons étudié l'effet d'une réaction chimique sur le transfert de matière pour des systèmes à deux phases sous écoulement. La phase continue est une phase fluide et la phase dispersée est constituée de particules de catalyseur au sein desquelles une réaction chimique irréversible de premier ordre a lieu. Le soluté réactif est transporté par l'écoulement externe de fluide et pénètre dans la particule par diffusion, il se produit alors une réaction chimique qui consomme cette espèce. Nous modélisons le problème par un couplage interne-externe des équations de bilan et au moyen de deux conditions limites de raccordement : continuité de la concentration et équilibre des flux de masse à la surface des particules. Le cas d'une seule sphère isolée est traitée en premier lieu de manière théorique et numérique. Nous proposons un modèle pour prédire le coefficient de transfert de masse (nombre de Sherwood «réactif») en tenant compte de la convection-diffusion externes et du couplage diffusion-réaction internes. Nous validons le modèle en le comparant à des simulations numériques directes pleinement résolues (DNS boundary-fitted) sur un maillage adapté à la géométrie des particules. Pour la simulation de systèmes multi-particules, nous mettons en œuvre une méthode d'interface «Sharp» pour traiter les fronts raides de concentration. Nous validons la mise en œuvre de la méthode sur des solutions analytiques existantes en cas de diffusion, de diffusion-réaction et par comparaison avec des corrélations de convection-diffusion disponibles dans la littérature. Dans le cas d'une réaction chimique en présence de convection-diffusion, nous validons la méthode et nous évaluons sa précision en comparant avec les simulations pleinement résolues de référence. Ensuite, nous étudions le problème de l'écoulement et du transfert autour de trois sphères alignées soumis à une réaction chimique interne. Nous proposons un modèle de nombre de Sherwood «réactif» en complément d'une prédiction de transfert pour chaque sphère disponible dans la littérature. Nous validons le modèle par comparaison avec des simulations numériques directes pour une large gamme de paramètres adimensionels. Ensuite, nous étudions la configuration du lit fixe de particules de catalyseur. Nous modélisons le profil de concentration moyenne, en tenant compte de la réaction chimique dans le lit et les profils de concentration moyenne surfacique et volumique des particules. Nous introduisons un modèle pour le nombre de Sherwood «réactif» qui est comparé à des simulations numériques pour en évaluer les limites de validité.

Abstract

Keywords : Mass transfer, Catalyst particle, Chemical reaction, Damkohler number, Sherwood number, Sharp Interface Method, Numerical simulation.

We studied the effect of a first order irreversible chemical reaction on mass transfer for two-phase flow systems in which the continuous phase is a fluid and the dispersed phase consists in catalyst spherical particles. The reactive solute is transported by the fluid flow and penetrates through the particle surface by diffusion. The chemical reaction takes place within the bulk of the particle. We handle the problem by coupling mass balance equations for internal-external transfer with two boundary conditions : continuity of concentration and mass flux at the particle surface. We start with the case of a single isolated sphere. We propose a model to predict mass transfer coefficient ('reactive' Sherwood number) accounting for the external convection-diffusion along with internal diffusion-reaction. We validate the model through comparison with fully resolved Direct Numerical Simulations (DNS) performed by means of a boundary-fitted mesh method. For the simulation of multi-particle systems, we implemented a Sharp Interface Method to handle strong concentration gradients. We validate the implementation of the method thoroughly thanks to comparison with existing analytical solutions in case of diffusion, diffusion-reaction and by comparison with previously established correlations for convection-diffusion mass transfer. In case of convection-diffusion-reaction, we validate the method and we evaluate its accuracy through comparisons with single particle simulations based on the boundary-fitted method. Later, we study the problem of three aligned-interacting spheres with internal chemical reaction. We propose a 'reactive' Sherwood number model based on a known non-reactive prediction of mass transfer for each sphere. We validate the model by comparison with direct numerical simulations for a wide range of dimensionless parameters. Then, we study the configuration of a fixed bed of catalyst particles. We model the cup-mixing concentration profile, accounting for chemical reaction within the bed, and the mean surface and volume concentration profiles of the particles. We introduce a model for 'reactive' Sherwood number that accounts for the solid volume fraction, in addition to the aforementioned effects. We compare the model to numerical simulations to evaluate its limitations.

Acknowledgements

I would like to start by expressing my sincere gratitude to those who believed in me, especially my brother Abdelmotaleb. Without you, accomplishing this goal would not have been possible.

My friend Monzer, in 2012, we had been both accepted to the same engineering program in Toulouse, unless you had no enough luck to obtain a visa due to war in Syria. I always thought of you.

IMFT - Toulouse - France

I would like to thank Professor Dominique Legendre, my professor at EN-SEEIHT, and my first research supervisor with whom I had the chance to start my research trip as an intern at IMFT. Dominique, thanks for your encouragement. It was a nice start, for me, to see my small name written beside yours in an international conference.

I would like to thank Professor Eric Climent, for all what he is. Eric, it has been more than five years I'm getting in touch with you, as a professor in my Engineering courses at ENSEEIHT, graduation project supervisor with IFPEn, master thesis supervisor, and my PhD thesis director. You taught me, beside science, how to be a multi-task man, who never complains. I was always impressed by your immense knowledge and calmness. I can't imagine a better supervisor than you.

I would sincerely like to thank my imft colleagues and friends, those who rendered IMFT an affectionate place. Guiquan Wang, you're so kind, beside many other things, thanks for having sent me the passport from Toulouse to Lyon.

Soléne chevrier, you gave me your new chair (with asking you) when you knew I had back-pain, and you took my old chair. Thank you for that attitude, I'll never forget what you have done, you're really nice.

Azeddine Rachih, thanks for having spent time in developing the part I use of JADIM code, the willingness you always showed to give help, and for your karaoke songs !

Amine, thanks for the fruitful discussions, I'm really happy to have shared the office with you.

Ainur NIGMETOVA, thanks for the black tea and the Kazakh chocolate. Valentin GOSSELIN, Thiam Elhadji (Ibrahima), and BOUTSIKAKIS Athanasios, thank you for the time we spent together, I discovered my Bowling skills thanks to you !

I wouldn't forget to thank my batch friend and colleague at ENSEEIHT and IMFT Hamza Oukili, for the nice endless discussions, and the exchange of ideas.

Good better best. Never let it rest.
Till your good is better, and your
better is best.

<div style="text-align: right;">

St. Jérôme

</div>

Contents

Contents

Part I

Introduction

Contents

1   Context

The interactions of solid and fluid phases are prominent through a wide range of industrial and energetic engineering applications, where the two phases interact and diverse complex physical and chemical phenomena occur between them. The interactions are present in, but not limited to, the following systems:

In ***Fluid Catalytic Cracking*** (FCC) systems [Shah et al., 2018], which are operated in petrochemical refineries to treat heavy crude oil compounds to break them into desirable lighter products [Abul-Hamayel, 2003]. Different modes of interactions can take place in these processes, such as adsorption and diffusion [Song et al., 2007] in zeolite crystals through molecules exchange at the zeolite-matrix interface, and diffusion in the meso and macro-pores of the matrix [Qin et al., 2015], where chemical reaction takes place in the form of heterogeneously catalyzed gas or liquid reaction, within the catalyst particles.

In ***Biomass gasification*** [Bridgwater, 1995, Turn et al., 1998], and biomass complete combustion [Baxter, 1993] processes, which are prospectively considered to be a sustainable alternative for fossil fuel [Naik et al., 2010] through extracting liquid bio-fuel from abundant organic bio-substances. These processes comprise most of solid-fluid interaction complexities, where gas diffusion takes place from fluid bulk phase to solid particle, then chemical reaction takes place within the particle.

In **catalytic converters**, which are post-treatment facilities used to treat exhaust gases resulting from internal imperfect combustion engines in automotive vehicles [Islam et al., 2018]. These systems incorporate physical and chemical coupled phenomena resulting from gas flow through a porous catalytic medium [Ozhan et al., 2014].

On the other hand, solid-fluid interactions are present in many other applications such as heavy-oil or bitumen extraction [Shokrlu and Babadagli, 2014]. Heated metal particles can alter the usage of expensive technology to heat reservoirs, such as steam injection that requires costly infrastructure, hot air injection [Dunn et al., 1989], electric/electro-magnetic methods [Mutyala et al., 2010] or flow improvers [Li et al., 2016]. The bitumen viscosity can rather be decreased through heat transfer between heated metal particles and the viscous oil [Hamedi Shokrlu et al., 2010].

Catalytic cracking processes, biomass gasification, or combustion, are usually operated at the industrial scale by means of two different types of reactors. The first type involves a network of fixed solid particles forming a porous medium with high solid volume fraction, through which the fluid flows. This system is called a 'fixed' bed reactor [Lu and Nikrityuk, 2018, Lemos et al., 2018]. The second type is when gas flows through particles of lower solid volume fraction and particles move, the particles' movement is termed as 'fluidization' [Kunii and Levenspiel, 2013] and the system is referred to as a 'fluidized' bed reactor [Yaghoobi-Khankhajeh et al., 2018, Wenzel et al., 2018].

The process modeling, operation, maintenance and optimization within these reactors require an advanced comprehension of their physical and chemical phenomena coupling. The challenges that impede the complete comprehension of these systems fall into two parts. The first part is the existence of multi-length scales [Radl et al., 2018], the smallest scale is at the particle level, which is an order of *mm* and the largest scale is an order of meters. We expect that the large scale behavior of the system is affected by the small scale interactions. The second challenge arises from the complex coupling among many physical and chemical phenomena. A comprehensive example of these complexities is a catalytic fluidized bed reactor [Bizon, 2017]. In this system, a gas enters with an imposed uniform inlet velocity, concentration and temperature. Momentum transfer [Kraft et al., 2018] occurs when fluid moves the solid particles maintaining them in a 'fluidized state'. Mass transfer [Voncken et al., 2018] occurs through chemical species diffusion and adsorption within the catalyst particles, where exothermic chemical reactions [Li et al., 2018] take place. Heat transfer [Bellan et al., 2018] occurs through the whole system, that is highly affected by the temperature distribution and has a direct impact on the reaction rate. The three mentioned phenomena interact with each other and this is referred to as 'phenomena coupling'. Understanding these systems has been a central objective for decades by means of experimental and numerical studies to probe phenomena coupling in particle-laden flows. Gunn [1978] was a pioneer with his experimental study to quantify heat or mass transfer within fixed and fluidized bed reactors. He introduced a correlation for the Nusselt number. Running experimental setups along with simplified analytical studies was the only research path

for decades, before the emergence of large supercomputers of increasing capacity over time, that enables one to perform Particle Resolved (PR) or Direct Numerical (DN) Simulations (PR/DNS) to simulate these systems. PRS has arisen as a powerful tool that is able to provide local-reliable information about the interactions at the particle scale. However, systems which can be fully resolved through PRS can comprise thousands, or up to tens of thousand of particles only. Exceeding this number of particles is still unaffordable in terms of computational cost. Because of that, larger scale numerical models have been developed to meet the demand to consider a bigger number of particles. Although it is able to treat a large number of particles, the large-scale 'meso' models suffer from inaccuracy as the local interactions at the particle level are unresolved. An approach that links the micro and meso scale models has been adopted in order to take the advantage of the fully resolved-reliable information provided at the micro scale to boost the meso scale models through providing the missing-unresolved information at the particle scale, by means of closure laws or correlations. The approach is referred to in literature as the multi-scale approach, and it has been previously detailed by [van der Hoef et al., 2008]. In this context, [Deen et al., 2014] and [Sun et al., 2015] introduced correlations for the heat transfer Nusselt number based on fitting with PRS data sets. In both studies, a comparison with the pioneering work of Gunn [1978] was performed. The Nusselt number correlations established for heat transfer can alternately be used for mass transfer, as Sherwood number correlations, in the so called mass transfer controlled or diffusion limited systems. In this case the reaction rate is infinite with respect to diffusion. Apart from systems where an infinite reaction is prominent, the Sherwood number correlations are invalid and modeling efforts are required to account for the effect of chemical reaction on mass transfer through these systems, which is the aim of this work.

1.1   Objectives and synthesis

We aim in this work at studying the effect of a first order irreversible reaction on mass transfer in systems composed of two fluid-solid phases, where chemical species diffuse from fluid bulk to solid spherical catalyst particles which undergo an internal chemical reaction. The study necessitates solving the convection-diffusion-reaction equation in both phases. Our numerical platform PeliGRIFF is originally based on the Distributed Lagrange Multiplier- Fictitious Domain method that is suited to treat particulate flows dynamics. This necessitates the implementation of a numerical model that is able to solve the required equations in both phases. The method must be able to handle sharp gradients at solid-fluid interface. The Sharp Interface Method is chosen to be implemented in our in-house code.

The objectives of this work can briefly be summarized as follows:

— The implementation of a Sharp Interface Method, and its complete parallelization to be able to treat multi-particle systems. The method must be able to solve accurately the convection-diffusion-reaction equation in both solid and fluid phases. The validation of the implemented method is done against analytical solutions and existing correlations in cases of diffusion and convection-diffusion, respectively. In case of convection-diffusion-reaction, an-

alytical solutions or previously established correlations are unavailable to be used for comparison and validation. We used a boundary fitted mesh method that fully resolves boundary layers to perform direct comparison between the two methods in order to validate and assess the accuracy of Sharp Interface Method.

— The establishment of a physical model that couples the external convection-diffusion with the internal diffusion-reaction for a 'single' particle system is required, before addressing complex multi-particle systems. The model depends on four parameters, the Reynolds number Re, the Schmidt number Sc, the Damkohler number Da, and the diffusion coefficient ratio between solid and fluid phases γ. The model is validated by means of direct numerical simulations issued from the boundary fitted method. The single particle system is used for direct comparison between the two numerical methods, the Sharp Interface and boundary fitted mesh method.

— The thoroughly validated Sharp Interface Method has been used to study multi-particle systems. An extension of the single particle physical model has been proposed for a system of three aligned interacting particles experiencing an external convection with diffusion.

— Systems composed of multiple-particles have been studied and a new physical model that describes mass transfer of the system in the presence of chemical reaction is established. The model for a single and three spheres is extended and this time it accounts for the solid volume fraction α_s in addition to the aforementioned four dimensionless numbers. The model is validated with numerical simulations.

As a complement to this Part(I), we give an overview on applications involving chemical reactions. We briefly describe our numerical platform PeliGRIFF and the multi-scale approach. Then, we give a quick review on mass transfer for a single catalyst particle undergoing a first order irreversible reaction.

In Part (II), we study the single particle system and we present a physical model with its complete validation through boundary fitted direct numerical simulations.

In Part (III), we implement a Sharp Interface Method and we couple it to the DLM-FD Method. We present a series of validation tests and we compare the method to reliable simulations of a boundary fitted mesh method that fully resolves boundary layers. We then study a system of three interacting particles under forced convective-diffusive stream coupled with an internal diffusion-reaction. We extend the established model for a single particle to three particles system. We validate the model by means of direct numerical simulation.

In Part (IV), we extend the established model for single and three particles to a network of fixed catalyst particles. We compare the model to numerical simulations and we show and discuss its limits. In Part(V), we give our concluding remarks and perspectives.

1.2   Applications involving chemical reaction

Fluid Catalytic Cracking

Cracking is a process of breaking long-chain heavy crude oil molecules, derived from atmospheric distillation and vacuum fractionators [Dupain et al., 2006], into lighter products, that can be used to produce gasoline and diesel fuel engines. Cracking process can be achieved without catalyst at high pressure and temperature, or with catalyst at lower temperature. Fluidized catalytic cracking processes, are able to produce fuels with lower benzene content, which is environmentally preferable because benzene is considered as a toxic material able to cause acute and chronic poisoning [Verma and Tombe, 2002]. Benzene undergoes an incomplete combustion, discharged into atmosphere and induces harmful effects on human body [Wang et al., 2018]. FCC units are operated worldwide and they provide 45% of the total car fuel consumption [Jarullah et al., 2017]. FCC system consists of three main parts: Preheating system, riser, and generator. As a process, feedstock is firstly preheated using heat exchangers up to 300-350 °C. Then, it gets atomized in the riser by means of atomization nozzles. Feedstock injection process determines 60-70% of the cracking reactions yield [Chen et al., 2016b], as desirable atomization nozzles may insure fast and uniform contact between feedstock and catalyst particles [Chen et al., 2016a]. Meanwhile, catalyst particles are being heated in the generator up to temperature 600 °C [Chang et al., 2014].
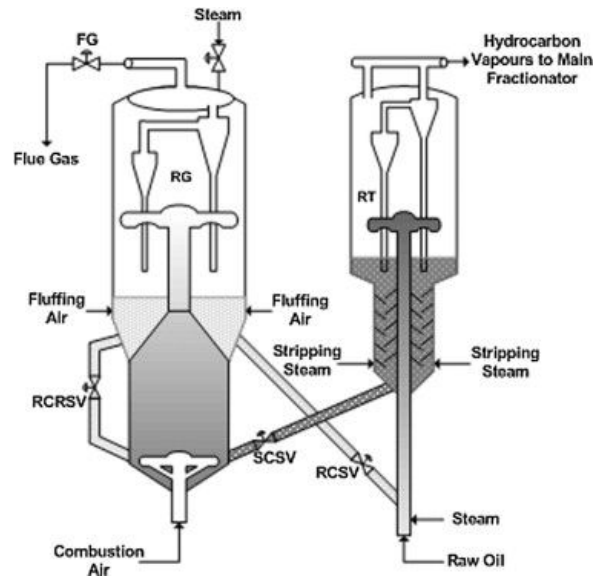
Figure I.1: Schematic diagram of a Fluid Catalytic Cracking system [Fernandes et al., 2012].

Catalyst particles enter the riser and gets in contact with vaporised hydrocarbons through fluidization. During this contact, hydrocarbon feedstock gets heated by the catalyst particles, which are providing heat for the endothermic reaction. The catalyst residence time in the riser ranges from 2 to 10 seconds [Alvarez-Castro et al., 2015], during which chemical reaction takes place in vapor phase and conversion occurs. Carbon deposit deactivates gradually the catalyst during its residence in riser, through coating the active sites and blocking the pores [Singh and Gbord-

zoe, 2017]. After, catalyst particles are separated by means of cyclones and pumped through regenerator for regeneration process. In generator, air enters the system where coke deposits are burned providing heat to catalyst particles. Then, regenerated catalyst is sent back to the riser. Many parameters can directly affect the efficiency of a FCC process. Hydrodynamic performance of the riser [John et al., 2018], catalyst-to-oil (CTO) ratio, catalyst properties and partial pressures.

Biomass gasification processes

Biomass gasification [Baruah and Baruah, 2014] is the process of biomass conversion into gaseous fuel through heating it in a gasified medium such as air, oxygen, steam, or their mixture. Distinguished from combustion [Sahu et al., 2014], gasification converts the intrinsic chemical energy of the carbon in the biomass into a flammable gas. During biomass gasification, its feedstock is promptly heated up and de-volatilized, forming tar, permanent gas, and solid char. Then, the tar and solid char undergo cracking, oxidization, and reduction to form gaseous products as the final products. Mainly, these products consist of carbon monoxide, carbon dioxide, methane, hydrogen, water vapor, and some light hydrocarbons, known as syngas which can be used to power gas engines and gas turbines or as a chemical feedstock to produce high rank fuels, such as liquid fuels, hydrogen, and carbon containing chemicals [Yang and Chen, 2014]. Chemical reactions take place in the gasification process are basically thermal biomass cracking [Wurzenberger et al., 2002] incorporating the partial and complete reactions, water gas shift and methanation reaction. For char gasification and water shift reaction, high temperatures are favorable to produce more H_2 and CO. When the gas yield is above 80% and the gas contains no excess tar, no nitrogen and no methane, the gasification process is considered as an ideal process. Achieving the high gas yield with low tar content is still the problem limiting the dependence on the biomass usage. Tar removal is a complex technical problem that has to be taken in consideration when developing gasifiers. The formed tar during pyrolysis processes experiences cracking, condensing and reformation. During cracking, tar is converted from mixed oxygenates to larger polycyclic aromatic hydrocarbon at temperature ranges from 400°C to more than 900° C. Dolomite catalysts, alkali metal and alkali earth metal are used for catalytic cracking of tar.

Biomass gasification processes are of two types, steam and CO_2 gasification. Steam gasification [Zhang et al., 2015] is more rapid than the CO_2 gasification and is more used in industrial applications. The carbon steam gasification is given by the following equation:

$$C + H_2O \leftrightarrows CO + H_2 \quad \Delta H = 118.5\,kJ\,mol^{-1} \tag{I.1}$$
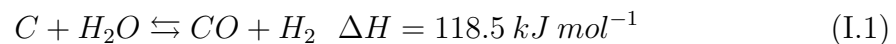
The reaction is endothermic and usually occurs at temperature in the range of 800° − 1200° C in the presence of H_2O. The influence of operating conditions on the kinetics requires more comprehension to design and operate the gasifiers because reaction kinetics depend strongly on the operating temperature, particle size, steam or CO_2 partial pressure.
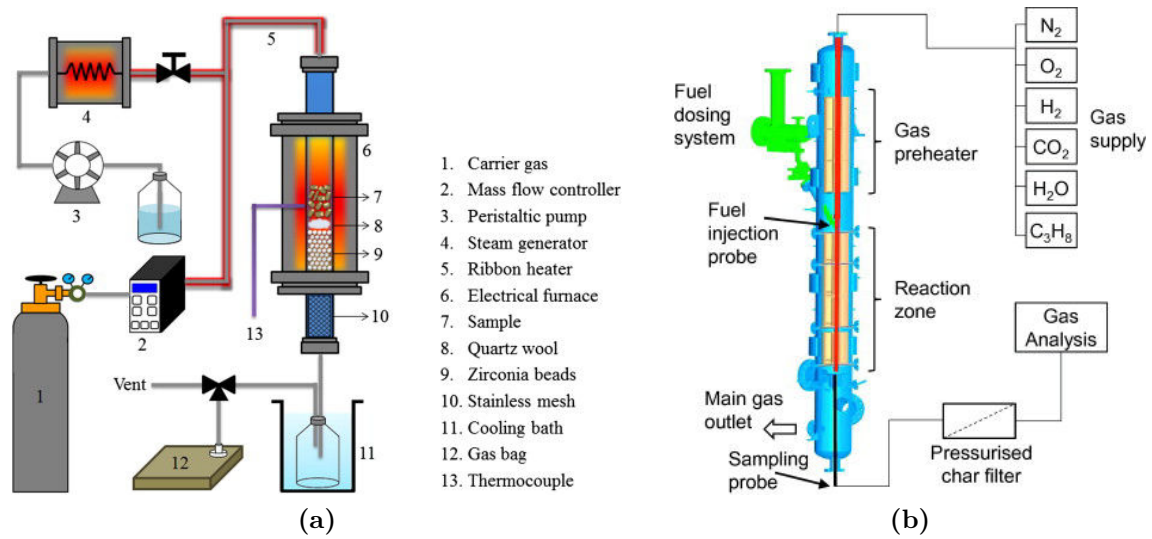
Figure I.2: Schematic diagram of gasification systems. a) Steam fixed bed reactor [Kaewpanha et al., 2014]. b) Entrained fluidized bed reactor [Tremel and Spliethoff, 2013]

The CO_2 gasification reaction [Jeremiáš et al., 2018] or Boudouard reaction is given by the following equation:

$$C + CO_2 \leftrightarrows 2CO \quad \Delta H = 159.9 \, kJ \, mol^{-1} \tag{I.2}$$
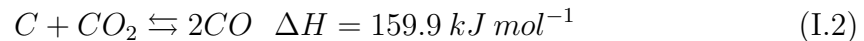
Both reactions (I.1) and (I.2) are reversible. The high temperature and low pressure favor the production of hydrogen and carbon monoxide whereas high pressure favors carbon dioxide formation [Roddy and Manson-Whitton, 2012]. The operating conditions, pressure and temperature, affect the gas products at the gasifier exit as well as the steady state equilibrium. High pressure and temperature push the reaction toward the equilibrium state whereas low temperature slows down the tendency toward equilibrium.

The design of gasifier or its selection depends on the feedstock material and the desired output product. Gasification processes can be carried out in a fixed bed reactor shown in FIG. I.2-a, fluidized bed, or an entrained flow gasifier shown in FIG. I.2-b. Gasification processes are of two types, low temperature < 1000 °C and high temperature > 1200 °C. Produced products at low temperature have half the energy in the gas stream whereas the rest half is in the methane and the tar. At high temperature, methane and tar formation are formed. Ash melting temperature is taken into consideration during the process, the adequate temperatures are either below the softening point (agglomeration) or above slagging temperature (melting) where the tar removal is straightforward. Complex phenomena are prominent in biomass gasification and combustion, strong mass transfer due to heterogeneous reactions alters the particle size, referred to as shrinkage. The hydrodynamic behavior of the systems gets affected due to particle shrinkage, that has a direct impact on drag force, and thus, on mass and heat transfer.

2 PeliGRIFF and the multiscale approach

PELIGRIFF Wachs [2011a], the **P**arallel **E**fficient **LI**brary for **GR**ains **I**n **F**luid **F**lows , is a numerical research code developed to treat particulate flows from moderate to high concentration through direct numerical simulation (DNS). These flows are prominent in a wide range of industrial applications and they are still partially understood even for simple particles geometries. Their complexity stems from the interaction between different scales, the smallest at the particle level, to the largest at the whole flow scale. The interaction between the solid and fluid phases needs to be accounted for once the solid volume fraction exceeds a specific value due to the induced effect by the solid phase on the flow structure. Along with their effect on the flow, the solid particles collision needs to be taken into consideration which necessitates the use of a contact law or model to handle particle-particle collisions. In PeliGRIFF, a micro/meso approach has been developed to treat these flows.

2.1 The multiscale approach

Multi-scale interactions in particulate flows are prominent in fluidized/fixed bed reactors which are widely used in chemical/petro chemical, environmental, and energetic engineering applications where the size of bed can be of the order of meters and the size of the fluidized particle is of the order of mm. The design and optimization of these beds require a better understanding of their momentum, mass and heat transfer. Experimental pilot-scale reactors can be used to do preliminary tests to understand and optimize their design. However, the use of experiments needs repetitive trials which is time consuming and thereby an expensive procedure.

Earth, micro scale   Solar system, meso-scale   Universe, macro-scale
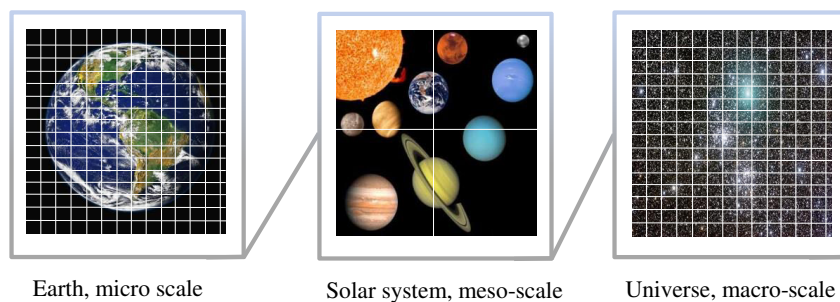
Figure I.3: The multi-scale approach, Earth: mostly all details are resolved - Solar system: less details are known - Universe: less and less details are known

Numerical simulations can be used to understand and help to optimize/design these beds and to understand the phenomena related to the effective gas-particle interaction, the drag force, as well as the particle-particle or particle-wall interaction, the collision. Large scale interactions (cluster formation) can be influenced by small

scale interactions (collisions, short range hydrodynamic force and torque) which represent a prime difficulty preventing from the use of a single numerical method to simulate the whole system from the largest to the smallest flow scales. In a way, this is partly due to the inability to perform fully resolved simulation of the industrial scale reactors [van der Hoef et al., 2008]. As a consequence, different models have been developed at different length and time scales with different levels of details, keeping the choice between highly resolved small systems and partially resolved large systems. An approach, called the multi-scale approach is being used to simulate these systems. The method consists of 3 scales, the micro scale at which the particle contains a few grid points per diameter and the whole interaction with fluid, i.e, to the velocity and the pressure fields around it are resolved. The second scale is the meso scale, at which the size of the grid is an order of magnitude larger than the particle diameter. The macro scale, is the largest scale where real systems can be simulated, and it is generally based on the Euler-Euler approach, or Multi Fluid Model (MFM). The spirit of the multi-scale approach is that the fully resolved systems accounting for all the important effects are used to find new correlations and closure laws which can be used at larger length scales to represent interactions effectively. The representation of the important interactions is not guaranteed through correlations based on micro scale, however, they are still able to describe the main characteristics of the flow in many cases.

2.2 The DLM/FD Method: Micro-Scale

Micro-scale flows are simulated in PeliGRIFF using the Distributed Lagrange Multiplier/Fictitious Domain method (**DLM/FD**), to resolve the solid/fluid interactions along with the Discrete Element Method (**DEM**) for the solid-solid interactions. The **DLM/FD** Method, firstly presented by Glowinski et al. [2001], combines the particle and fluid equations of motion into a single, weak, and general equation of motion called total momentum equation. It can be applied to any fluid-particle system. The combined equations are derived through the combined velocity space incorporating the rigid body motion (no-slip) on the particle.

- Governing equations:

The equations are non-dimensionlized by taking L_c^* for length, U_c^* for velocity and $T = L_c^*/U_c^*$ for time. For pressure $\rho_f^* U^{*2}$ and $\rho_f^* U^{*2}/L_c$ for the lagrange multiplier of the rigid body motion, with ρ_f^* is the fluid density.

The combined momentum equation:

$$\int_\Omega \left(\frac{\partial \boldsymbol{u}}{\partial t} + \boldsymbol{u}\nabla \cdot \boldsymbol{u}\right)\cdot\boldsymbol{\nu}d\boldsymbol{x} - \int_\Omega p\nabla \cdot \boldsymbol{\nu}d\boldsymbol{x} + \frac{1}{Re_c}\int_\Omega \nabla\boldsymbol{u} : \nabla\boldsymbol{\nu} + \int_{p(t)} \lambda \cdot \nu d\boldsymbol{x} = \boldsymbol{0}, \forall\boldsymbol{\nu} \in \nu_0(\Omega) \tag{I.3}$$

$$(\rho_r - 1)\left[V_p\left(\frac{d\boldsymbol{U}}{dt} - Fr\frac{\boldsymbol{g}^\star}{g^\star}\right)\cdot\boldsymbol{V} + \left(\boldsymbol{I}_p\frac{d\boldsymbol{\omega}}{dt} + \boldsymbol{\omega} \wedge \boldsymbol{I}_p \cdot \boldsymbol{\omega}\right)\cdot\xi\right] - \sum_j (\boldsymbol{F}_c)_j \cdot \boldsymbol{V} -$$
$$\sum_j (\boldsymbol{F}_c)_j \cdot \boldsymbol{\xi} \times \boldsymbol{R_j} - \int_{p(t)} \lambda \cdot (\boldsymbol{V} + \xi \times \boldsymbol{r})d\boldsymbol{x} = \boldsymbol{0}, \forall\boldsymbol{V} \in \mathbb{R}^d, \xi \in \mathbb{R}^{\breve{d}} \tag{I.4}$$

$$\int_{P(t)} \boldsymbol{\alpha} \cdot \boldsymbol{u} - (\boldsymbol{U} + \boldsymbol{\omega} \times \boldsymbol{r}) d\boldsymbol{x} = \boldsymbol{0}, \ \forall \boldsymbol{\alpha} \in \Lambda(t) \tag{I.5}$$

where Ω is a bounded domain $\in \mathbb{R}^d$, $d \in [2,3]$ and $\partial\Omega$ its boundary. Dirichlet boundary conditions are assumed on the boundary $\partial\Omega$ for the fluid velocity field. Continuity equation:

$$-\int_{\Omega} q\nabla \cdot \boldsymbol{u} d\boldsymbol{x} = \boldsymbol{0}, \ \forall q \in p_0(\Omega) \tag{I.6}$$

where $\boldsymbol{u} \in \nu_{\partial\Omega}(\Omega)$ denotes the fluid velocity vector, $p \in P(\Omega)$ the pressure, $\boldsymbol{\lambda} \in \boldsymbol{\Lambda}(t)$ the velocity distributed langrange multiplier, $\boldsymbol{U} \in \mathbb{R}^d$ the particle translational velocity vector, $\boldsymbol{\omega} \in \mathbb{R}^d$ the particle angular velocity vector, d the number of nonzero components of $\boldsymbol{\omega}$. $(\boldsymbol{\nu}, \boldsymbol{q}, \boldsymbol{\alpha}, \boldsymbol{V}, \boldsymbol{\zeta})$ the test functions for $(\boldsymbol{u}, \boldsymbol{p}, \boldsymbol{\lambda}, \boldsymbol{U}, \boldsymbol{\omega})$, respectively. $\boldsymbol{F}_c \in \mathbb{R}^d$ the contact forces, $\boldsymbol{R} \in \mathbb{R}^d$ the vector between paticle gravity center and the contact point, $\boldsymbol{r}$ the position vector with respect to particle gravity center, $V_p = M^*/(\rho_s^* L_c^{*d}) \in \mathbb{R}$ the dimensionless particle volume, M^* the particle mass, $\boldsymbol{I}_p = \boldsymbol{I}_p^*/(\rho_s^* L_c^{*(d+2)}) \in \mathbb{R}^{d\times d}$ the dimensionless particle inertia tensor, $\rho_s^* \in \mathbb{R}$ the particle density, $\boldsymbol{g}^*$ the gravity acceleration and $g^* \in \mathbb{R}$ the gravity acceleration magnitude. Where the introduced functional spaces are defined as the following

$$\nu_0(\Omega) = \{\boldsymbol{\nu} \in H^1(\Omega)^d | \boldsymbol{\nu} = \boldsymbol{0} \ on \ \partial\Omega\} \tag{I.7}$$

$$\nu_{\partial\Omega}(\Omega) = \{\boldsymbol{\nu} \in H^1(\Omega)^d | \boldsymbol{\nu} = \boldsymbol{u}_{\partial\Omega} \ on \ \partial\Omega\} \tag{I.8}$$

$$P(\Omega) = \left\{q \in \mathcal{L}^2(\Omega) | \int_{\Omega} q d\boldsymbol{x} = 0\right\} \tag{I.9}$$

$$\Lambda(t) = H^1(t)(P(t))^d \tag{I.10}$$

The Reynolds number, Froude number and the density ratio are defined as :

$$Re_c = \frac{\rho^\star U_c^\star L_c^\star}{\eta^\star} \quad (\text{I.11}) \qquad Fr_c = \frac{g^\star L_c^\star}{U_c^{\star 2}} \quad (\text{I.12}) \qquad \rho_r = \frac{\rho_s^\star}{\rho_f^\star} \quad (\text{I.13})$$

3   Mass transfer through a single catalyst particle

$\mathbf{M}$ASS transport is a physical phenomenon that occurs when mass gets transported from one location to another under the effect of a driving force, e.g., concentration gradient or fluid flow. Mass transfer is prominent in a wide range of chemical engineering applications such as Adsorption [Hou and Hughes, 2002, Tatler et al., 1999], Absorption [Chilton and Colburn, 1934, Qi and Cussler, 1985], Distillation [Schofield et al., 1987, Qtaishat et al., 2008], Drying Plumb et al. [1985], Hernandez et al. [2000], Precipitation [Reuvers et al., 1987, Boom et al., 1994], and many other applications that comprise diffusion, convection and reaction. The rate at which the material gets transported from one phase to another, under concentration gradient, is referred to as mass transfer coefficient [Seader et al., 2011]. For a spherical particle with an initial concentration C_A, diffusing in a medium of fluid with an initial concentration $C_{A,fluid}$, we can relate the mass transfer coefficient, the effective mass transfer area $S_{particle}$, the driving force $(C_{A,p} - C_{A,fluid})$, and the mass transfer rate, $dN_{A,particle}/dt$, by the following equation [Kunii and Levenspiel, 2013]:

$$- \frac{1}{S_{particle}} \frac{dN_{A,particle}}{dt} = k_{d,p}(C_{A,p} - C_{A,fluid}) \tag{I.14}$$

For a single particle of initial concentration $C_A = C_{0,particle}$, immersed in a domain with fluid at rest, of different concentration $C_{fluid} = C_{0,fluid} < C_{0,particle}$, pure diffusion takes place. When the fluid around the particle flows, the material diffused by the particle gets convected by the moving fluid. The mass transport by the movement of fluid is called convection. In the presence of chemical reactions, diffusion occurs in the fluid film surrounding the particle, then, through its pores, forming an active catalyst site. Based on conservation laws, mass transfer can be described mathematically in case of chemical reaction, for a volume element in the fluid film surrounding the particle, as follows:

$$(N_i S_i)_{in} + r_i \Delta V = (N_i S_i)_{out} + \frac{dn_i}{dt} \tag{I.15}$$

Where N_i is the flux density, r_i is the generation rate, S is the surface area, n_i is the amount of material in the volume element ΔV. In case of a catalytic system, n_i is the concentration in the fluid, expressed as $\epsilon \Delta V c_i$, where ϵ is the voidage. By taking $\Delta((N_i S_i)_{in/out}) = (N_i S_{i_{in}} - N_i S_i)_{out}$, dividing by ΔV, and ΔV tending to 0, we obtain the following equation:

$$\epsilon \frac{dc_i}{dt} = -\frac{dN_i}{dr} + r_i \tag{I.16}$$

For a spherical particle, $S = 4\pi r^2$, $dV = 4\pi r^2 dr$. At steady state, $dc_i/dt = 0$, leading to the following equation:

$$\frac{d^2 c_i}{dr^2} + \frac{2}{r}\frac{dc_i}{dr} = -\frac{r_i}{D_s} \tag{I.17}$$

In the above equation D_s is considered to be constant inside the catalyst particle. The equation is valid in case of a first order reaction and can be transformed to

a Bessel differential equation by taking $c = rc_i$ [Murzin and Salmi, 2005], and it writes as follows:

$$\frac{d^2c}{dr^2} - \gamma^2 c = 0 \tag{I.18}$$

where $\gamma^2 = \phi^2/r_p^2$, ϕ is the Thiele modulus [Thiele, 1939], expressed in (I.19) and represents the reaction to diffusion rate. Low Thiele modulus corresponds to reaction limited or kinetics controlled system, and high Thiele modulus corresponds to diffusion limited or mass transfer controlled system.

$$\phi = d_p \sqrt{\frac{k}{D_s}} \tag{I.19}$$

Using boundary conditions $c = c_0|_{r=r_p}$ and $dc/dr = 0|_{r=0}$, the solution of (I.18) can be written as (I.20) and it represents the concentration profile inside the particle:

$$C(x) = \frac{\sinh(\phi x/2)}{x\sinh(\phi/2)} \tag{I.20}$$

with $x = r/d_p$. The flux density at the surface of the particle can be derived through the following equation:

$$N_s = -D_s \frac{dc}{dr}\bigg|_{r=r_p} \tag{I.21}$$

Where D_s is the effective diffusion coefficient, used because the diffusional cross section is smaller than the geometric cross section, and due to the irregular pore structure of the particle, or tortuosity τ. For a molecule diffusing into a particle through its surface, the tortuosity can be described as the ratio of path length L', covered by the molecule divided by the initial length L, if there were no deviations, $\tau = L/L'$. The effective diffusion coefficient is defined as:

$$D_s = \frac{\epsilon D_f}{\tau} \tag{I.22}$$

Thus, in case of reaction taking place inside the particle, the flux at the surface can be evaluated by deriving (I.20) at $x = 1$ (r=R). It can be written as follows:

$$N_s = -\frac{D_s C_s}{\sinh(\phi/2)}\left((\phi/2)\cosh(\phi/2) - \sinh(\phi/2)\right) \tag{I.23}$$

Catalyst particles attain lower reaction rates than bulk rates due to diffusion limitation. The ratio of reaction rate inside the catalyst particle to the reaction rate that would be obtained if there was no diffusion limitation is referred to as an effectiveness factor. This factor can be evaluated by considering the ratio of the total molar flux and the molar N' that would be obtained in the absence of diffusion limitation:

$$\eta = \frac{N_s S_p}{r_s V} \tag{I.24}$$
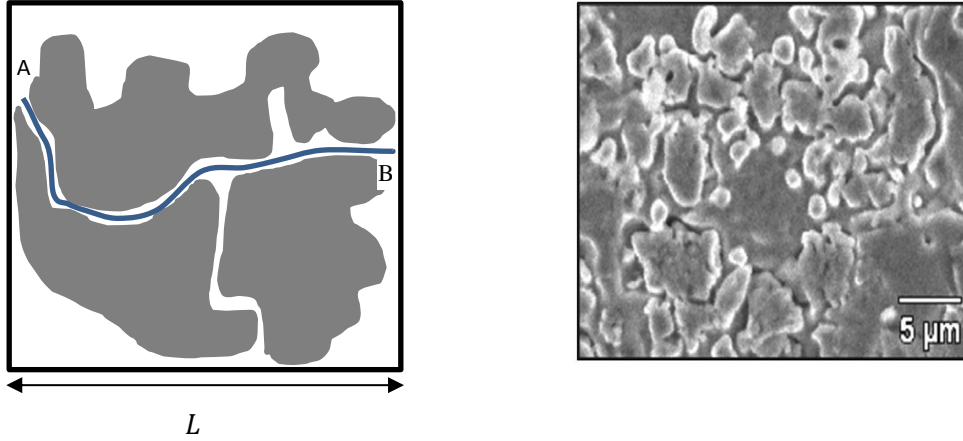
(a) Illustration of tortuosity concept

(b) Pores inside a porous particle Dey et al. [2013]

Figure I.4: Tortuosity, L' is the path length (blue line) traveled by a molecule moving from point A to point B due to deviations caused by the curved pore structure, $\tau = L'/L$.

Using (I.23), (I.20), and (I.24), the effectiveness factor can be written as:

$$\eta = \frac{6}{\phi}\left(\frac{1}{\tanh(\phi/2)} - \frac{1}{\phi/2}\right) \tag{I.25}$$

When diffusion rate is limited compared to reaction rate, i.e. high Thiele modulus, (I.25) has an asymptotic limit $6/\phi$. The higher the Thiele modulus is, the steeper the concentration profile inside the particle, and the lower the effectiveness factor. Fig. I.5 shows the dependence of concentration profile as well as effectiveness factor on the Thiele modulus. The concentration profile is expressed in (I.20) and it describes the concentration variation along the particle diameter.

Mass transfer can be quantified by means of some dimensionless numbers which help to understand the coupled effects of diffusion, convection and reaction. In systems incorporating convection and diffusion, convective to diffusive mass transfer rates can be represented, for a single particle, by the Sherwood number:

$$Sh = \frac{kd_p}{D_f} \tag{I.26}$$

(a) Concentration profile   **(b)** Effectiveness factor
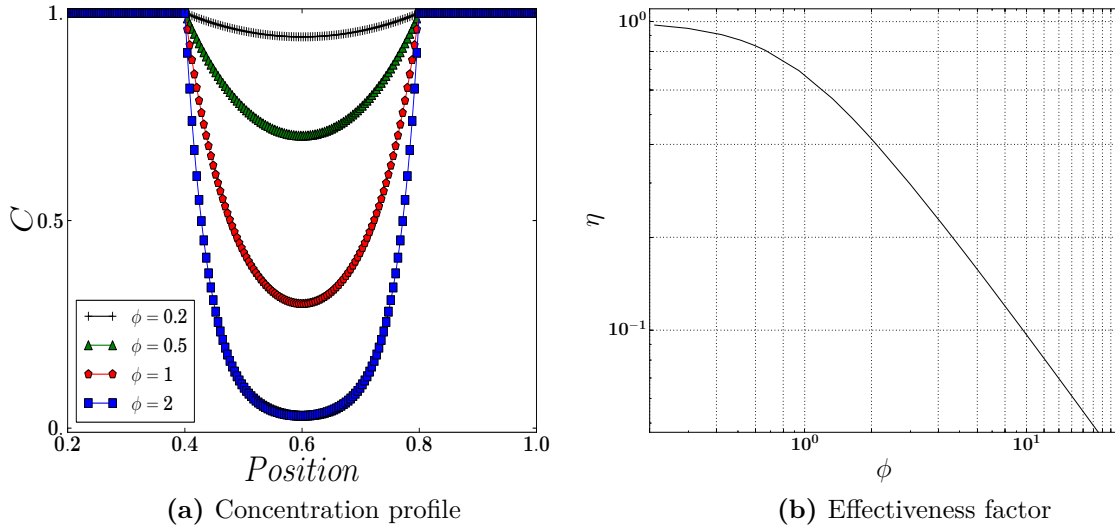
Figure I.5: Variation of concentration profile and effectiveness factor as function of Thiele modulus

Where k is the mass transfer coefficient, d_p is the particle diameter, and D_f is the bulk diffusion coefficient. For pure diffusion, and in an infinite domain, the Sherwood number has an analytical solution $Sh = 2$. In the presence of convection, there is no analytical solution. The Sherwood number can be estimated by empirical correlations that have been previously established through experimental and numerical studies, such as the Ranz-Marshell correlation Ranz et al. [1952], (I.27), and Frossling correlation (I.28):

$$Sh = 2 + 0.6Re^{\frac{1}{2}}Sc^{\frac{1}{3}}, \quad 0 \leq Re \leq 200 \ , \ 0 \leq Sc \leq 2.5 \tag{I.27}$$

$$Sh = 2 + 0.552Re^{\frac{1}{2}}Sc^{\frac{1}{3}}, \quad 0 \leq Re \leq 800 \ , \ 0 \leq Sc \leq 2.7 \tag{I.28}$$

Another correlation has been numerically established by [Feng and Michaelides, 2000] for the problem of single particle heat transfer. The effect of the variation of the Peclet number, Reynolds number with Nusselt number (the Sherwood number for mass transfer) has been derived from DNS data. The correlation is valid in the range of $0 \leq Re \leq 2000$ and $0 \leq Pe \leq 1000$.

$$Sh = 0.922 + Pe^{1/3} + 0.1Re^{1/3}Pe^{1/3} \tag{I.29}$$

In the previous correlations, Sc is the Schmidt number and it represents the viscous diffusive rate to the molecular diffusive rate, (I.30).

$$Sc = \frac{\mu}{\rho D_f} \tag{I.30}$$

μ is the fluid viscosity and ρ its density. Along with (I.30) and (I.31), the Peclet number which measures the advective transport rate to the diffusive transport rate, can be defined as follows:

$$Re = \frac{\rho u d_p}{\mu} \qquad (I.31) \qquad Pe = ReSc = \frac{d_p u}{D_f} \qquad (I.32)$$

The presence of convection is associated with a boundary layer surrounding the particle. The boundary layer is a layer where velocity magnitude is less than the bulk due to friction or no slip condition, $\mathbf{u} = 0$ at the particle surface. The ratio of the thickness of mass boundary layer δ_m to hydrodynamic boundary δ layer scales as:

$$\frac{\delta_m}{\delta} = Sc^{-1/3} \tag{I.33}$$

In systems where solid particle is undergoing an internal diffusion-reaction coupled with an external convection-diffusion, three regimes might be predominant. (i) When the reaction rate is very slow compared to diffusion rate, the particle surface concentration approaches that of bulk, and the system is said to be kinetics controlled. (ii) When the reaction rate is infinite compared to diffusion, the surface concentration of the particle approaches zero, and the system is mass transfer controlled. (iii) When the reaction rate is high but finite, the surface concentration is unknown and the system is neither mass transfer nor kinetics controlled. Established correlations for Sherwood number are able to describe mass transfer in case where no chemical reaction is taking place in the solid particle, or, in case where an infinite reaction is taking place. In this case the system is analogous to that of heat transfer and only external effects in the system need to be accounted for. In the other cases, the internal and external effects need to be taken in account through an external-internal coupling, which is the aim of this work.

Un moment de patience dans un
moment de colère empêche mille
moments de regrets.

Ali Bin Abi Talib

A moment of patience in a moment
of anger prevents a thousand
moments of regret.

Ali Bin Abi Talib

Part II

Mass transfer from a single particle in a fluid flow coupled with internal diffusion and chemical reaction

This chapter has been submitted to Chemical Engineering Science and it is in revision process.

Contents

Mass transfer towards a reactive particle in a fluid flow : numerical simulations and modeling

Mostafa Sulaiman[a], Eric Climent[b], Abdelkader Hammouti[a], Anthony Wachs[c,d]

[a] *IFP Énergies Nouvelles, Fluid Mechanics Department, Rond-point de l'échangeur de Solaize, BP 3, 69360 Solaize, France*
[b] *Institut de Mécanique des Fluides de Toulouse (IMFT), Université de Toulouse,CNRS - Toulouse, France*
[c] *Department of Mathematics, University of British Columbia, 1984 Mathematics Road, Vancouver, BC V6T 1Z2, Canada*
[d] *Department of Chemical and Biological Engineering, University of British Columbia, 2360 East Mall, Vancouver, BC V6T 1Z3, Canada*

Abstract

Keywords: Catalyst particle, Mass transfer, Sherwood number, Chemical reaction, Thiele modulus.

We study mass transfer towards a solid spherical catalyst particle experiencing a first order irreversible reaction coupled to an external laminar flow. Internal chemical reaction and convective-diffusive mass transfer in the surrounding fluid flow are coupled by concentration and flux boundary conditions at the particle surface. Through this coupling, the mean particle surface and volume concentrations are predicted and the internal/external Sherwood numbers are obtained. We investigate the interplay between convection, diffusion, and reaction by direct numerical simulations (DNS) and establish a model for the mass transfer coefficient accounting for diffusion and internal first-order chemical reaction. We derive an equivalent "reactive Sherwood number" that quantifies mass transfer in the system through general mass balance or using the classic additivity rule. The model is numerically validated by DNS over a wide range of Reynolds and Schmidt numbers and Thiele modulus. Finally, we also test the unsteady response of the model. The model predicts the evolution of the mean volume concentration for a particle placed in a steady convective-diffusive stream. Predictions of the unsteady model are shown to be in very good agreement with DNS results.

Graphical Abstract

Part II. Mass transfer from a single particle in a fluid flow coupled with internal diffusion and chemical reaction
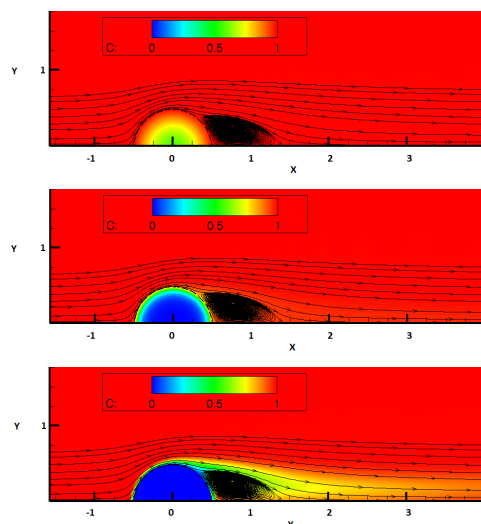
1 Introduction

1.1 Industrial context

Interactions of solid and fluid phases are prominent in a wide range of industrial-chemical engineering applications of energy or raw material transformation. While the two phases are in contact, mass transfer occurs between them. In petrochemical processes, fluid-solid interactions occur in fluidized and fixed bed reactors that are used for catalytic cracking of large scale basic compounds into desirable molecules, that can be used as fuel for engines (Jarullah et al. [2017]). Different modes of mass transfer take place in these systems. When a liquid or a gas flows through a randomly stacked batch of solid-catalytic particles, referred to as a fixed bed, or through fine catalytic particles maintained in a fluidized state, referred to as a fluidized bed, adsorption and diffusion in zeolite material occur. Molecules exchange takes place at the zeolite-matrix interface and diffusion in meso and macro-pores. In these systems, reactants are usually transferred from the continuous "bulk" phase to the dispersed phase where a chemical reaction takes place in the form of a heterogeneously catalyzed gas or liquid reaction (Rossetti [2017]), within the catalyst particles. Biomass gasification processes also represent an active engineering field for solid-fluid interactions. These processes aim at extracting liquid bio-fuel from abundant organic material through pyrolysis. They are usually operated in fluidized bed gasifiers (Ismail et al. [2017] & Neves et al. [2017]) or fixed bed gasifiers (Baruah et al. [2017] & Mikulandrić et al. [2016]) where solid biomass particles undergo complex mass transfer enhanced by chemical reaction, coupled to heat transfer and hydrodynamics. The strong mass transfer experienced by the solid particle is associated with conversion that occurs through phase change leading to severe particle deformations. The same interactions are encountered in many other industrial applications. Modeling the interaction between solid and fluid phases, and the interplay among fluid flow, heat and mass transfer with chemical reaction, is of tremendous importance for the design, operation and optimization of all the aforementioned industrial operating systems. Investigating mass transfer coefficients between the dispersed solid phase and the continuous fluid phase at the particle scale, referred to as micro-scale, where the interplay between the two phases is fully resolved, helps to propose closure laws which can be used to improve the accuracy of large scale models through multi-scale analysis.

1.2 Literature overview

Many studies have been carried out to analyze and model coupling phenomena in particulate flow systems. For dilute regimes, (Ranz et al. [1952], Clift et al. [2005], Whitaker [1972]) and more recently (Feng and Michaelides [2000]) have carried out studies to characterize the coupling of mass/heat transfer with hydrodynamics for a single spherical particle. This configuration is characterized by the Reynolds number for the flow regime and the Schmidt number (ratio of momentum to molecular diffusion coefficients). They established correlations for the Sherwood number in diffusive-convective regimes in the absence of chemical reaction for an isolated particle. For dense regimes, (Gunn [1978]) measured the heat transfer coefficient within a fixed bed of particles including the effect of the particulate volume concentration.

Part II. Mass transfer from a single particle in a fluid flow coupled with internal diffusion and chemical reaction

(Piché et al. [2001]) and (Wakao and Funazkri [1978]) investigated mass transfer coefficients in packed beds for different applications.

There has also been a considerable interest in systems incorporating chemical reaction. (Sherwood and Wei [1957]) studied experimentally the mass transfer in two-phase flow in the presence of slow irreversible reaction. (Ruckenstein et al. [1971]) studied unsteady mass transfer with chemical reaction and deduced analytical expressions for transient and steady state average Sherwood numbers for bubbles and drops. This has been extended to the case of a rising bubble under creeping flow assumptions (Pigeonneau et al. [2014]). (Losey et al. [2001]) measured mass transfer coefficient for gas-liquid absorption in the presence of chemical reaction for a packed-bed reactor loaded with catalytic particles. (Kleinman and Reed [1995]) proposed a theoretical prediction of the Sherwood number for coupled interphase mass transfer undergoing a first order reaction in the diffusive regime. For a solid spherical particle experiencing first order irreversible reaction in a fluid flow, (Juncu [2001] and Juncu [2002]) investigated the unsteady conjugate mass transfer under creeping flow assumption. The effect of Henry's law and diffusion coefficient ratio on the Sherwood number were investigated when the chemical reaction is occurring either in the dispersed or continuous phases. [Lu et al., 2018] employed an Immersed Boundary Method (IBM) to study mass transfer with a first order irreversible surface chemical reaction and applied it to a single stationary sphere under forced convection. The external mass transfer coefficients were numerically computed and compared to those derived from the empirical correlation of Frössling. [Wehinger et al., 2017] also performed numerical simulations for a single catalyst sphere with three pore models with different complexities: instantaneous diffusion, effectiveness factor approach and three dimensional reaction-diffusion where chemical reaction takes place only within a boundary layer at the particle surface. In [Partopour and Dixon, 2017b], a computational approach for the reconstruction and evaluation of the micro-scale catalytic structure is employed to perform a pore-resolved simulations coupled with the flow simulations. [Dierich et al., 2018] introduced a numerical method to track the interface of reacting char particle in gasification processes. [Dixon et al., 2010] modeled transport and reaction within catalyst particles coupled to external 3D flow configuration in packed tubes. Through this method, 3D temperature and species fields were obtained. [Bohn et al., 2012] studied gas-solid reactions by means of a lattice Boltzmann method. Effectiveness factor for diffusion-reaction within a single particle was compared to analytical solutions and the shrinkage of single particle was quantitatively compared experiments.

In this paper, our efforts are devoted to the coupling of a first order irreversible reaction taking place within a solid catalyst particle experiencing internal diffusion and placed in a flow stream (external convection and diffusion). In order to fully understand the interplay between convection, diffusion and chemical reaction we have carried out fully coupled direct numerical simulations to validate a model which predicts the evolution of the Sherwood number accounting for all transport phenomena. The paper is organized as follows. First, we investigate the diffusive regime and then include external convection. The prediction of the mass transfer coefficient is validated through numerical simulations over a wide range of dimensionless parameters. Finally, the model is tested under unsteady conditions.

Part II. Mass transfer from a single particle in a fluid flow coupled with internal diffusion and chemical reaction

2 Diffusive regime

2.1 Internal diffusion and reaction

We consider a porous catalyst spherical bead of diameter $d_p^* = 2r_p^*$, effective diffusivity D_s^* within the particle, and effective reactivity k_s^*. Please note that dimensional quantities are distinguished from dimensionless quantities by a "*" superscript. A reactant is being transferred from the surrounding fluid phase to the solid phase, where it undergoes a first order irreversible reaction. We use the term effective for the molecular diffusion and reaction constant of the kinetics because these quantities are related to the internal microstructure of the porous media (porosity, tortuosity and specific area for the catalytic reaction). We assume that this can be approximated by a continuous model in which the effective diffusion coefficient is typically ten to hundred times lower than in unconfined environment (diffusion coefficient is D_f^* outside the particle). The constant k_s^* of a first-order irreversible chemical reaction is also assumed constant due to homogeneous distribution of the specific area within the porous media experiencing the catalytic reaction. The particle is immersed in an unbounded quiescent fluid of density ρ_f^* and viscosity μ_f^*. Based on these assumptions, we can write the balance equation for the reactant of molar concentration C^* in the solid phase :

$$\frac{\partial C^*}{\partial t^*} = D_s^* \nabla^2 C^* - k_s^* C^* \tag{II.1}$$

At steady state, the concentration profile inside the catalyst particle can be found by integrating (II.1) and using two boundary conditions, shortly summarized : $C^* = C_s^*|_{r^*=r_p^*}$ and $dC^*/dr^* = 0|_{r^*=0}$. The solution is available in transport phenomena textbooks such as [Bird et al., 2015]:

$$C_r = \frac{C^*}{C_s^*} = \frac{\sinh(\phi r)}{2r \sinh(\phi/2)} \tag{II.2}$$

where $r = r^*/d_p^*$ is the dimensionless radial position, C_s^* the surface concentration, and $\phi = d_p^* \sqrt{\frac{k_s^*}{D_s^*}}$ is the Thiele modulus.

The dimensional mass flux density at the particle surface $r^* = r_p^*$ can be found by deriving (II.2) with respect to r^* and inserting it in (II.3):

$$N_S^* = -D_s^* \frac{dC^*}{dr^*}\bigg|_{r^*=r_p^*} = -\frac{D_s^* C_s^*}{d_p^*}\left(\frac{\phi}{tanh(\phi/2)} - 2\right) \tag{II.3}$$

The effectiveness factor η (II.4) for a catalyst particle is defined as the internal rate of reaction inside the particle, to the rate that would be attained if there were no internal transfer limitations. For a catalyst bead of given surface concentration C_s^*, the effectiveness factor is:

$$\eta = \frac{6}{\phi}\left(\frac{1}{tanh(\phi/2)} - \frac{2}{\phi}\right) \tag{II.4}$$

2.2 Particle surface concentration with external diffusion

Assuming a purely diffusive regime, mass transfer in the fluid phase is governed by the following equation:

$$\frac{\partial C^*}{\partial t^*} = D_f^* \nabla^2 C^* \tag{II.5}$$

The concentration profile in the fluid phase can be found through integrating (II.5), at steady state, with two Dirichlet boundary conditions, $C^*|_{r^*=r_p^*} = C_s^*$ and $C^*|_{r=\infty} = C_\infty^*$. We aim in this section at finding the particle surface concentration at steady state. Once the surface concentration is known, the external concentration gradient between the particle surface and the bulk can be found. Also, the mean volume concentration of the particle can be evaluated, which will then permit to evaluate the internal and external Sherwood numbers as a measure of dimensionless mass transfer.

The external diffusive problem can be coupled to the internal diffusive-reactive problem through two boundary conditions at the solid-fluid interface : (*i*) continuity of mass flux and (*ii*) continuity of concentration. At steady state, a balance is reached between diffusion from the fluid phase and consumption due to internal reaction in the solid particle, resulting in a specific (unknown) concentration C_s at the particle surface. The flux density within the fluid film surrounding the particle can be written as:

$$N_f^* = k_f^*(C_s^* - C_\infty^*) \tag{II.6}$$

which is equal to the flux density through the solid surface (II.3), yielding:

$$k_f^*(C_s^* - C_\infty^*) = -D_s^* \frac{C_s^*}{d_p^*}\left(\frac{\phi}{tanh(\phi/2)} - 2\right) \tag{II.7}$$

k_f^* represents the mass transfer coefficient in the fluid phase which can be obtained from the Sherwood number $Sh = k_f^* d_p^*/D_f^*$. Then we can determine the surface concentration as:

$$C_s^* = \frac{C_\infty^*}{1 + \frac{1}{Bi}\left(\frac{\phi/2}{tanh(\phi/2)} - 1\right)} \tag{II.8}$$

where $Bi = k_f^* d_p^*/2D_s^*$ is the mass transfer Biot number. The external mass transfer coefficient $k_f^* = 2D_f^*/d_p^*$ defined in (II.6) is obtained analytically from Fick's law applied to the steady profile of external diffusion in an infinite domain, $C^*(r) = (C_s^* - C_\infty^*)\frac{r_p^*}{r^*} + C_\infty^*$. For this configuration, the surface concentration is prescribed analytically as follows :

$$C_s^* = \frac{C_\infty^*}{1 + \gamma\left(\frac{\phi/2}{tanh(\phi/2)} - 1\right)} \tag{II.9}$$

which explicitly depends on the kinetics of the chemical reaction. The dimensionless numbers governing the problem, in the absence of convection in fluid phase, are the Thiele modulus ϕ and the diffusion coefficient ratio $\gamma = \dfrac{D_s^*}{D_f^*}$.

2.3   General model including convection effects

When the particle is experiencing an external-convective stream, no analytical solution can be deduced for the surface concentration due to the inhomogeneity of the velocity and concentration fields. Similarly to the diffusion-reaction problem presented in the first case, where the Sherwood number was evaluated analytically, it will be instead evaluated from one of the correlations established for convective-diffusive problems by (Feng and Michaelides [2000], Whitaker [1972] and Ranz et al. [1952]). According to this, the mean surface concentration $\overline{C_s^*}$ can be obtained.

In a general case, the molar flux towards the particle surface (II.6) can be written as:

$$N_f^* = Sh\frac{D_f^*}{d_p^*}(\overline{C_s^*} - C_\infty^*) \tag{II.10}$$

which under steady state conditions is equal to the consumption rate in the particle

$$N_f^* = -\frac{d_p^*}{6}\eta k_s^* \overline{C_s^*} \tag{II.11}$$

where η is the effectiveness factor (II.4). The internal reaction changes only the concentration gradient inside the particle, and thus, does not change the value of the external Sherwood number. We assume that the concentration over the particle surface is equal to its average $\overline{C_s^*}$.

This gives the general expression for the surface concentration

$$\overline{C_s^*} = \frac{C_\infty^*}{1 + \frac{2\gamma}{Sh}\left(\frac{\phi/2}{tanh(\phi/2)} - 1\right)} \tag{II.12}$$

and the molar flux

$$N_f^* = \frac{-C_\infty^*}{\frac{d_p^*}{D_f^* Sh} + \frac{6}{d_p^* \eta k_s^*}} \tag{II.13}$$

where the Sherwood number Sh is a function of the Reynolds number $Re = \rho_f^* u_{ref}^* d_p^*/\mu_f^*$ and the Schmidt number $Sc = \mu_f^*/\rho_f^* D_f^*$, and u_{ref}^* is a characteristic velocity scale. Sh is equal to 2 for pure diffusion in the fluid recovering (II.9).

3   Transfer/Reaction in presence of a fluid flow

3.1   Numerical simulations

We define the full flow domain as Ω, the part of Ω occupied by the solid particle as P and the part of Ω occupied by the fluid as $\Omega\backslash P$. The whole numerical problem involves solving the Navier-Stokes equations (II.14) and (II.15) under the no-slip boundary condition at the particle surface $r^* = r_p^*$ together with the mass balance equations in the solid (II.16) and in the fluid (II.17) submitted to the continuity

of the concentration and the continuity of the mass flux at the particle surface ∂P defined by $r^* = r_p^*$, i.e., $C_{r_p^{*+}}^* = C_{r_p^{*-}}^*$ and $-D_f^* \frac{dC^*}{dr^*}|_{r_p^{*+}} = -D_s^* \frac{dC^*}{dr^*}|_{r_p^{*-}}$, respectively. A uniform flow $u_{in}^* = u_{ref}^*$ and a constant concentration are imposed at the inlet of the domain. The free-stream and symmetry conditions simply state that the normal velocity, the tangential stress, and the mass flux are zero on the boundary under consideration. The outflow condition allows the flow to leave the domain without significantly perturbing the computed field.

$$\nabla \cdot \mathbf{u}^* = 0 \quad , \quad \text{in } \Omega \backslash P \tag{II.14}$$

$$\rho_f^* \frac{D\mathbf{u}^*}{Dt^*} = -\nabla p^* + \mu \nabla^2 \mathbf{u}^*, \quad \text{in } \Omega \backslash P \tag{II.15}$$

$$\frac{\partial C^*}{\partial t^*} = D_s^* \nabla^2 C^* - k_s^* C^*, \quad \text{in} P \tag{II.16}$$

$$\frac{\partial C^*}{\partial t^*} + \mathbf{u}^* \cdot \nabla C^* = D_f^* \nabla^2 C^*, \quad \text{in } \Omega \backslash P \tag{II.17}$$

First, the Navier-Stokes equations are solved to reach steady state for the desired Reynolds number. Then equations (II.16)-(II.17) only are solved to determine the temporal evolution of the concentration. Starting from the initial conditions $C^* = 0$ in the particle and $C^* = C_\infty^*$ in the fluid, the conjugate problem is solved using the JADIM code developed in our group.

The basic numerical methods used in this code have been thoroughly described by (Magnaudet et al. [1995] and Calmet and Magnaudet [1997]). Consequently they will be only quickly summarized here. The JADIM code solves the incompressible Navier-Stokes equations and the concentration equation in general orthogonal curvilinear coordinates. Equations are integrated in space using a finite volume method in which advective and diffusive terms are evaluated with second-order centered schemes. The solution is advanced in time by means of a three-step Runge-Kutta time-stepping procedure where the nonlinear terms are computed explicitly while the diffusive terms are treated using the semi-implicit Crank-Nicholson algorithm. Incompressibility is satisfied after the third intermediate time step by solving a Poisson equation for an auxiliary potential from which the true pressure is deduced. The complete algorithm is second order accurate in both space and time.

The orthogonal mesh grid used in the present work is presented in Fig. II.1. The orthogonal axi-symmetric mapping is obtained by using the streamlines and the equipotential lines of the potential flow around a circular cylinder. The mesh is stretched in order to enforce at least four points in the external mass boundary layer thickness that scales as $Pe^{-1/3}$ ($Pe = Re.Sc$ is the Peclet number). Simulations are carried out under a 2D axi-symmetric configuration which reproduces the geometry of a spherical particle. The fluid computational domain is limited by the particle surface and by external boundaries on which inflow, free stream, axial symmetry, and outflow boundary conditions are imposed, respectively. The equations are solved inside the particle over a polar mesh adjusted to the fluid mesh at the particle surface. The internal mass boundary layer thickness gets thinner when the kinetics of the chemical reaction increases. The mesh is then refined following the scaling of the internal boundary layer as ϕ^{-1}. At least four grid points stand within

the internal boundary layer in order to compute properly the interface gradient of concentration. A particle of radius r_p is placed in domain with a spatial extension of at least $r_\infty^* = 100 r_p^*$, so that the assumption of infinite domain is physically valid.
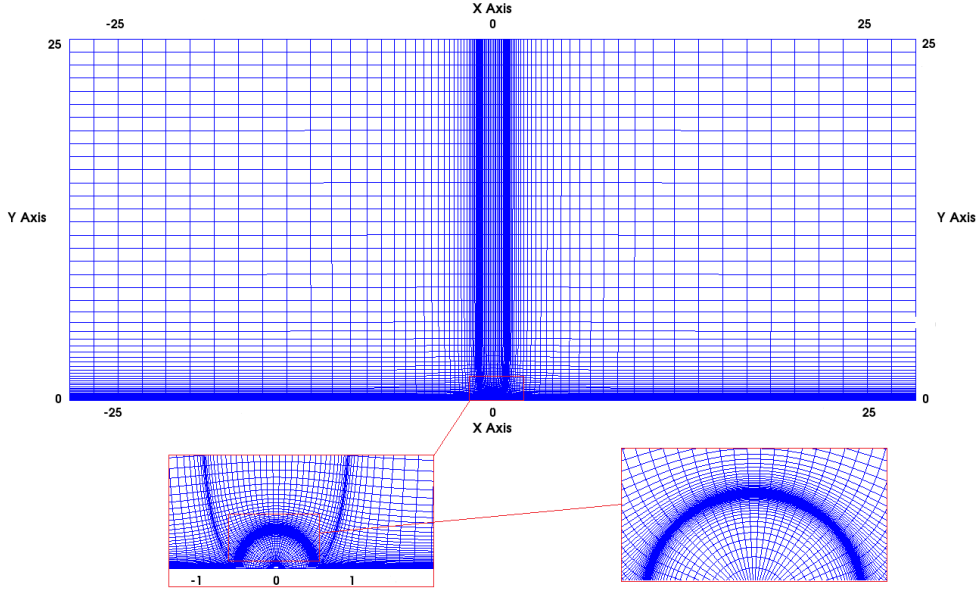
Figure II.1: Domain geometry and mesh grid

Validation of internal diffusion-reaction

The numerical method has been validated in case of diffusion-reaction inside the particle. The surface concentration has been fixed, $C_s^* = 1$, and the concentration profiles have been compared at steady state to those of the analytical solution for different values of Thiele moduli, representing slow, intermediate, and fast reaction rates. The numerical results show a very good agreement in FIG. II.2 with the analytical solution, (II.2).
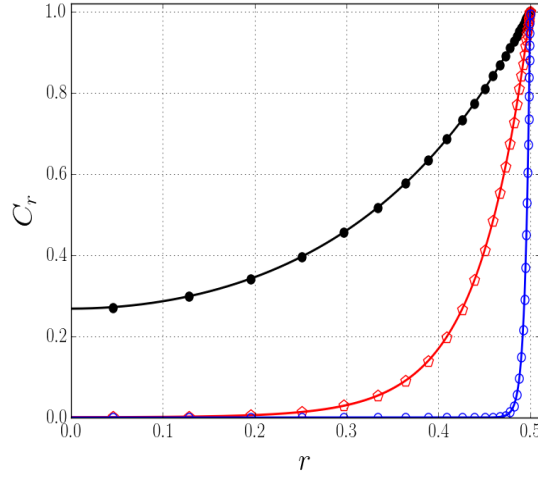
Figure II.2: Concentration profiles: comparison of simulations with analytical solution for different Thiele moduli. Analytical solution is represented by continuous lines and numerical simulations is represented by markers. Black line and black filled circles correspond to $\phi^2 = 40$. Red line and open red pentagons correspond to $\phi^2 = 4 \cdot 10^2$. Blue line and opened circles correspond to $\phi^2 = 4 \cdot 10^3$.

Validation of external convection-diffusion

The numerical method is firstly validated through the comparison of computed Sherwood numbers with existing correlations in a convective-diffusive problem without reaction. A spherical particle is placed at the center of a 2D axi-symmetric domain, FIG. II.1, of dimensions $L_x^* = L_y^* = L_z^* = 100r_p^*$. A constant inlet velocity is imposed with constant concentration $C_\infty^* = 0$ and a constant concentration $C_s^* = 1$ is imposed at the particle surface. The Sherwood number $Sh = \dfrac{k_f^* d_p^*}{D_f^*}$ is evaluated at steady state and compared with the reference correlations for Reynolds numbers ranging from diffusive regime to $Re = 200$. We chose the highest value of $Re = 200$ so that the flow remains 2D axi-symmetric. Beyond this regime, we would need to verify the validity of the model with 3D simulations. Our computed Sherwood numbers are in a very good agreement with those of (Feng and Michaelides [2000]) and are shown in FIG. II.3.
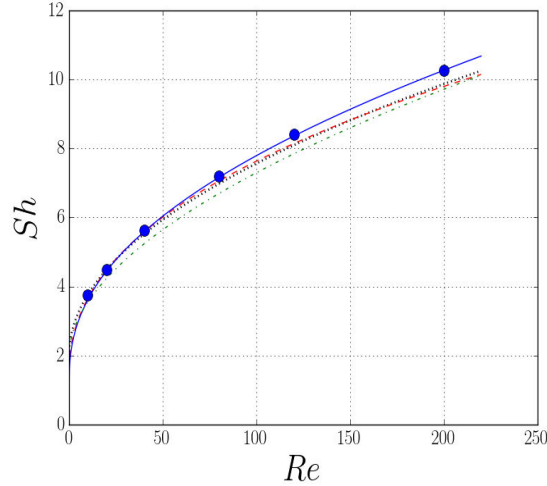
Figure II.3: Sherwood number comparison with previous references for Schmidt number $Sc = 1$. Numerical results are represented by filled blue circles. The blue continuous line stands for the correlation of (Feng and Michaelides [2000]), doted line for the correlation of (Ranz et al. [1952]), dashed-doted line for the correlation of (Whitaker [1972]) and dashed line for the correlation of (Clift et al. [2005]).

Diffusion-Reaction: Internal/External coupling

The analytical solution for the mean surface concentration found in (II.9) is compared to the simulation results. In a finite domain, the concentration profile in the fluid phase can be found through integrating (II.5), at steady state, with two Dirichlet boundary conditions, $C^* = C_s^*|_{r^*=r_p^*}$ and $C^* = C_\infty^*|_{r^*=r_B^*}$. The concentration profile due to diffusion in a bounded spherical domain of radius r_B^*, (II.18), is used to determined the mass transfer coefficient and the particle surface concentration.

$$C^*(r^*) = \frac{r_p^* r_B^*}{(r_p^* - r_B^*)r}(C_\infty^* - C_s^*) + \frac{C_s^* r_p^* - C_\infty^* r_B^*}{r_p^* - r_B^*} \tag{II.18}$$

To validate our numerical simulations, we use the surface concentration C_s^* provided by (II.9). We compare the dimensionless concentration profiles in the particle, i.e., (II.2) and in the fluid phase, i.e., (II.18) to our computed profiles. We consider two different cases. In the first case, we set the Thiele modulus to $\phi = 20$ and the diffusion ratio to $\gamma = 10$ and plot analytical and computed solutions in FIG. II.4. In the second case, we set the Thiele modulus to $\phi = 20$ and the diffusion ratio to $\gamma = 0.1$ and plot analytical and computed solutions in FIG. II.5. A very good agreement has been obtained between the analytical predictions and the numerical simulations.
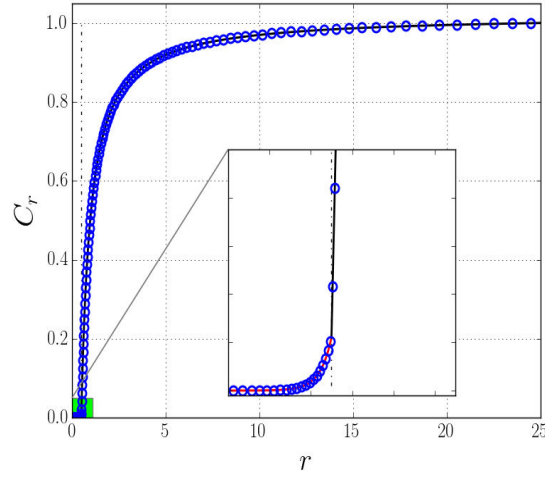
Figure II.4: Concentration profile as function of dimensionless radius for $\gamma = 10$ and $\phi = 20$. Inset stands for a zoom on the particle surface ($r^*/r_p^* = 1$). Particle interface is represented by vertical dashed-doted line, analytical solution corresponds to continuous line and numerical solution to open circles.
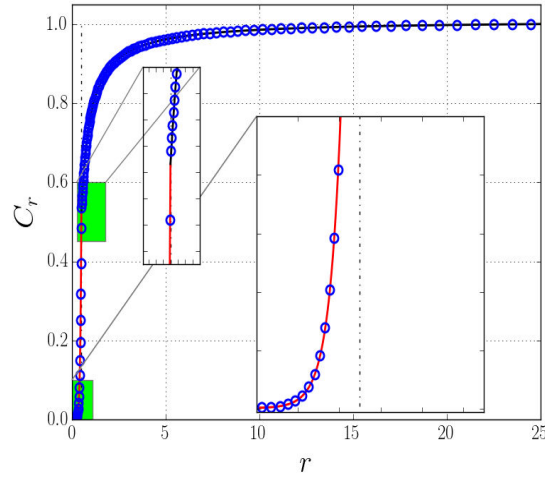
Figure II.5: Concentration profile as function of dimensionless radius for $\gamma = 0.1$ and $\phi = 20$. Inset stands for a zoom on the particle surface ($r^*/r_p^* = 1$). Particle interface is represented by vertical dashed-doted line, analytical solution corresponds to continuous line and numerical solution by open circles.

Then, we vary the Thiele modulus ϕ from 0 to 40 and we plot the surface concentration for $Re = 0$ corresponding to external diffusion only ($Sh = 2$) in FIG. II.6. Our computed results show again a very good agreement with the analytical prediction.
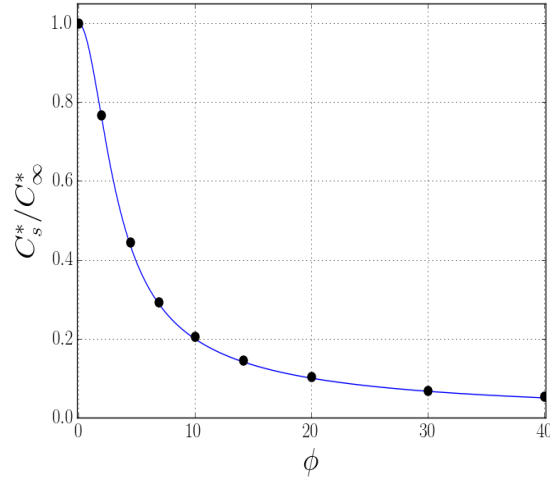
Figure II.6: Surface concentration as function of Thiele modulus at steady state in the diffusive regime. Continuous line and black circles correspond to analytical solution and simulation results respectively.

3.2 Fully coupled model and simulations

In this section the hydrodynamics is added to the problem and the particle experiences external convection with a uniform inlet velocity as sketched in FIG. II.7, i.e., at Reynolds number $Re \neq 0$.

The problem is treated as two coupled systems: an external problem involving convection-diffusion and an internal problem involving diffusion-reaction. In this case, the problem is governed by the following four dimensionless numbers: the Thiele modulus ϕ and the diffusion coefficient ratio γ for diffusion-reaction, and the Reynolds number Re and the Schmidt Sc for convection-diffusion.

The ranges of dimensional physical parameters generally encountered in gas-solid and liquid-solid industrial applications are summarized in Table(II.1). Liquids are typically hydrocarbons such as Heptane, Decane, or Hexadecane. Gases are a mixture of hydrogen gas and hydrocarbons. According to this table, the corresponding ranges of dimensionless numbers are: $\gamma \in [0.01, 1]$, $\phi \in [0.02, 6]$, $Re \in [0, 200]$, and $Sc \in [1, 1000]$.

Parameter	Catalyst particle	Liquid	Gas
$D^*\,(m^2 s^{-1})$	$10^{-6} - 10^{-10}$	$\sim 10^{-9}$	$10^{-6} - 10^{-5}$
$r_p^*\,(mm)$	$1 - 5$	$-$	$-$
$k_s^*\,(s^{-1})$	$10^{-6} - 10$	$-$	$-$
$u_f^*\,(cm\,s^{-1})$	$-$	$1 - 2$	$0.2 - 20$
$\mu_f^*\,(mPa\,s)$	$-$	$0.386 - 0.92$	~ 0.9
$\rho_f^*\,(kg\,m^{-3})$	$-$	$695 - 770$	~ 100

Table II.1: Physical properties of industrial gas-solid and liquid-solid reactive particulate systems.

Part II. Mass transfer from a single particle in a fluid flow coupled with internal diffusion and chemical reaction
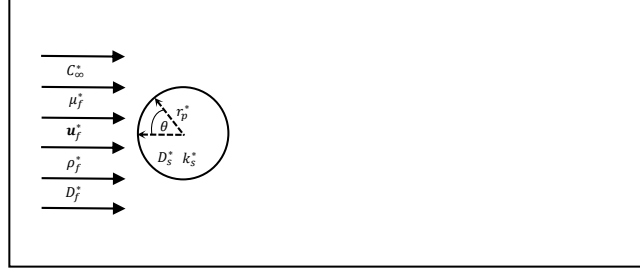
Figure II.7: Schematic diagram of the flow configuration and physical properties. The numerical domain size is $L_x^* \times L_y^* = 100 r_p^* \times 100 r_p^*$.

In this case, fluid flows with an imposed inlet concentration and reacts within the catalyst particle.

(a) $\phi = 2$, $Re = 100$, $Sc = 1$ and $\gamma = 10$.

(b) $\phi = 6$, $Re = 100$, $Sc = 1$ and $\gamma = 10$.

(c) $\phi = 200$, $Re = 100$, $Sc = 1$ and $\gamma = 10$.
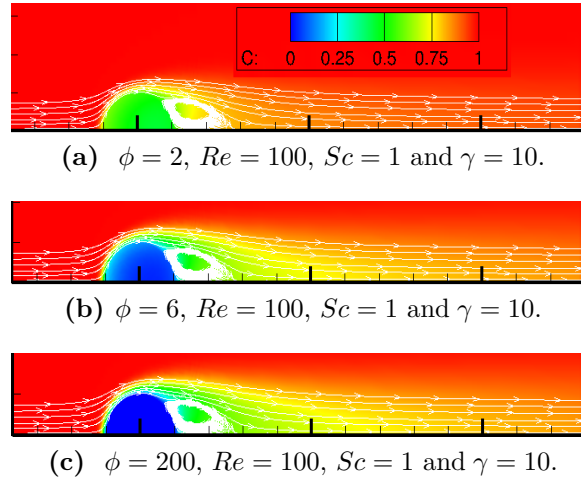
Figure II.8: Concentration spatial distribution for a) slow reaction b) intermediate, and c) fast reactions at Reynolds number $Re = 100$.

According to reaction kinetics, three regimes can be identified as follows.
1) If the reaction rate is sufficiently slow compared to the diffusion rate ($\phi \ll 1$), the concentration at the catalyst particle surface is the same as the inlet fluid concentration. This regime is referred to as reaction limited.
2) When the reaction rate is extremely fast ($\phi \gg 1$) compared to diffusion rate, the catalyst surface concentration approaches zero and the process is controlled by mass transfer resistance.
3) The third regime is when none of the two previous regimes is predominant and the catalyst surface concentration is unknown. The aim of our work is to propose a model covering the three regimes. The model for the prediction of the mean surface concentration is presented in (II.12) and compared to numerical simulations to test the validity of the range of physical parameters listed in Table(II.1).

The external Sherwood number is evaluated from the correlation of Feng and Michaelides [2000] given in (II.19). This correlation corresponds to a purely mass transfer controlled system and is valid for Peclet and Reynolds numbers above 10.

It exhibits the best agreement with our numerical results for convective-diffusive mass transfer as shown in FIG. II.3. Note that for a convection free, i.e., purely diffusive, problem the solution is analytical as the external Sherwood number has an exact value 2 which unfortunately is not the limit of the correlation towards low Peclet and Reynolds numbers.

$$Sh = 0.922 + Pe^{1/3} + 0.1Re^{1/3}Pe^{1/3} \tag{II.19}$$

In the presence of chemical reaction, the mean surface concentration $\overline{C_s^*}$ has been numerically evaluated according to (II.20) and computed results are compared with the model.

$$\overline{C_s^*} = \frac{1}{2} \int_0^\pi C^*(r^* = r_p^*, \theta) \sin(\theta) d\theta \tag{II.20}$$

First, we set the Schmidt number to $Sc = 1$ and the diffusion coefficient ratio to $\gamma = 0.1$. We plot in FIG. II.9 the mean surface concentration as a function of the Reynolds number from 20 to 200 for 3 values of the Thiele modulus $\phi = 60$, $\phi = 200$ and $\phi = 6 \cdot 10^4$. Second, we set the Schmidt number to $Sc = 10$ and the diffusion coefficient ratio to $\gamma = 0.1$. We plot in FIG. II.10 the mean surface concentration as a function of the Reynolds number from 20 to 200 for 3 values of the Thiele modulus $\phi = 200$, $\phi = 632$ and $\phi = 2 \cdot 10^4$. In all cases, the surface concentration is observed to be decreasing with the increase of Thiele modulus at constant Reynolds number and increasing with the increase of the Reynolds number at constant Thiele modulus. In general, our computed results match well our proposed model (II.12).
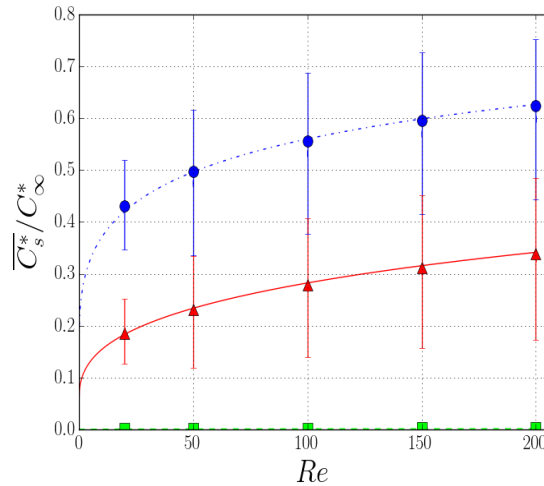
Figure II.9: Mean surface concentration as function of Reynolds number at steady state, $Sc = 1$, $\gamma = 0.1$ and three Thiele moduli. Case 1, $\phi = 60$, model represented by dashed-doted line and simulations by blue disks. Case 2, $\phi = 200$, model represented by red line and simulations by red triangles. Case 3, $\phi = 6 \cdot 10^4$, model represented by dashed-doted green line and simulations by green squares. The error bars correspond to minimum and maximum concentration values along θ.
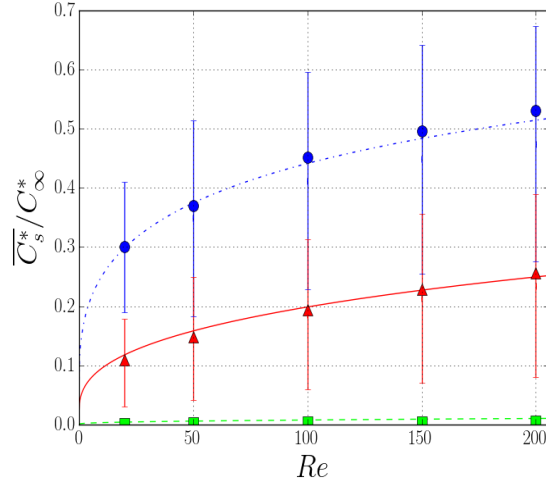
Figure II.10: Mean surface concentration as function of Reynolds number at steady state, $Sc = 10$, $\gamma = 0.1$ and 3 Thiele moduli. Case 1, $\phi = 200$, model represented by dashed-doted line and simulations by blue disks. Case 2, $\phi = 632$, model represented by red line and simulations by red triangles. Case 3, $\phi = 2 \cdot 10^4$, model represented by dashed-doted green line and simulations by green squares. The error bars correspond to minimum and maximum concentration values along θ.
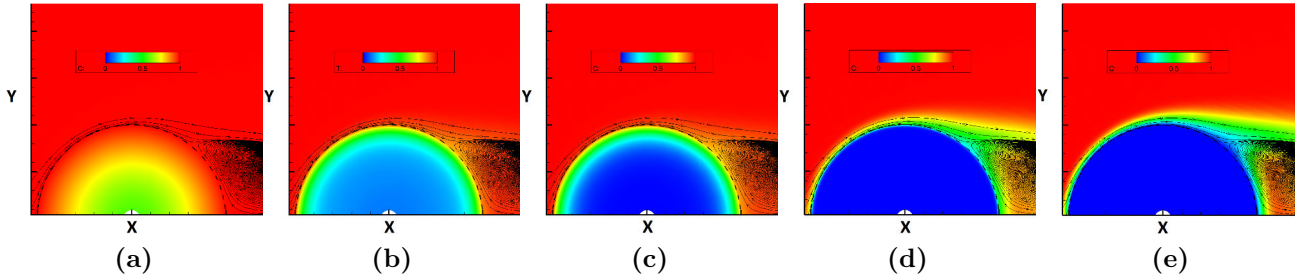
Figure II.11: Spatial distribution of concentration at Reynolds number $Re = 100$, $Sc = 10$ and $\gamma = 0.1$ for different Thiele moduli. a) $\phi = 2$, b) $\phi = 20$, c) $\phi = 200$, d) $\phi = 632$ and e) $\phi = 2 \cdot 10^4$.

The spatial distributions of concentration are shown in Fig. II.11 for four Thiele moduli. a) represents a slow reaction rate or kinetics limited system with $\phi = 2$. e) represents a mass transfer controlled system for Thiele modulus $\phi = 2 \cdot 10^4$, b), c) and d) represent a system that is neither reaction nor mass transfer controlled.

Figure II.12: Surface concentration variation along the arc length at Reynolds number $Re = 100$, $Sc = 10$ and $\gamma = 0.1$ for different Thiele moduli. Case A, $\phi = 2$ represented by continuous line and right triangles. Case B, $\phi = 20$ represented by continuous line and left triangles. Case C, $\phi = 200$ represented by continuous line and squares. Case D, $\phi = 632$, represented by continuous line and circles. Case E $\phi = 2 \cdot 10^4$, represented by continuous line and up-down triangles. Horizontal dashed doted lines correspond to mean surface concentration $\overline{C_s^*}$ and vertical dashed line locates the separation angle θ_s of the wake streamlines.

The concentration profiles along the arc length have been plotted in FIG. II.12. In case A, the surface concentration is constant and is equal to that of inlet fluid. In case E, the surface concentration is also constant and it approaches zero. In cases B, C and D the systems are neither controlled by kinetics nor by mass transfer and the surface concentration is non-uniform and attains a minimum near the separation angle θ_s of the wake. These spatial variations of the surface concentration may induce non-uniformity of the local mass flux. We investigate the variations of the local dimensionless flux $2\pi \frac{\partial C}{\partial r} r^2 sin(\theta) d\theta$ along the arc length θ. In FIG. II.13, the local flux has been normalized by its average for the cases A, C and E of FIG. II.12. For case A, the concentration gradient normal to the particle surface is almost constant while the surface concentration is equal to the bulk concentration. The local flux of mass follows the variation of the sine function corresponding to local element of surface (zero at the poles and maximum in the equatorial plane). For cases C and E, the gradient of concentration varies along θ in combination with the elementary surface yielding non-monotonous variation of the local mass flux. Mass flux is enhanced in the region of strong effect of convection (between $\pi/4$ in the front of the particle and the equatorial plane) while chemical reaction yields lower concentration at the rear of the particle. This can be observed in FIG. II.12. All those non-uniformities of concentration and mass flux distributions cancel out yielding good accuracy of our simple modeling based on uniform surface concentration. This is supported by FIG. II.14 showing that the concentration profiles for any angle within the particle is very close to the analytic Thiele profile when the concentration is made dimensionless by the local surface concentration $C_s^*(\theta)$.

Part II. Mass transfer from a single particle in a fluid flow coupled with internal diffusion and chemical reaction

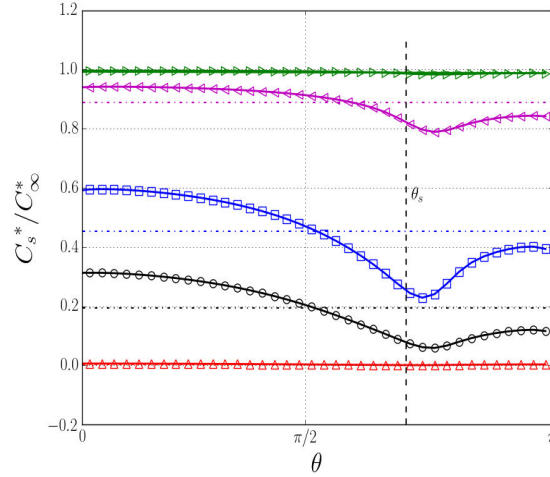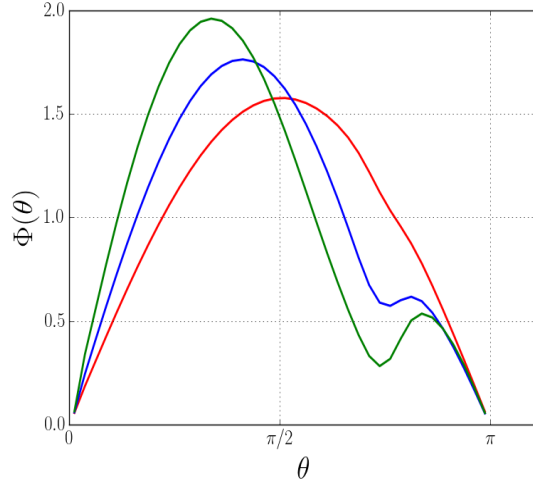**Figure II.13:** Local dimensionless mass flux along the arc length at Reynolds number $Re = 100$, $Sc = 10$ and $\gamma = 0.1$ for different Thiele moduli. Case A, $\phi = 2$ represented by red line. Case C, $\phi = 200$ represented by blue line. Case E, $\phi = 2 \cdot 10^4$ represented by green line.
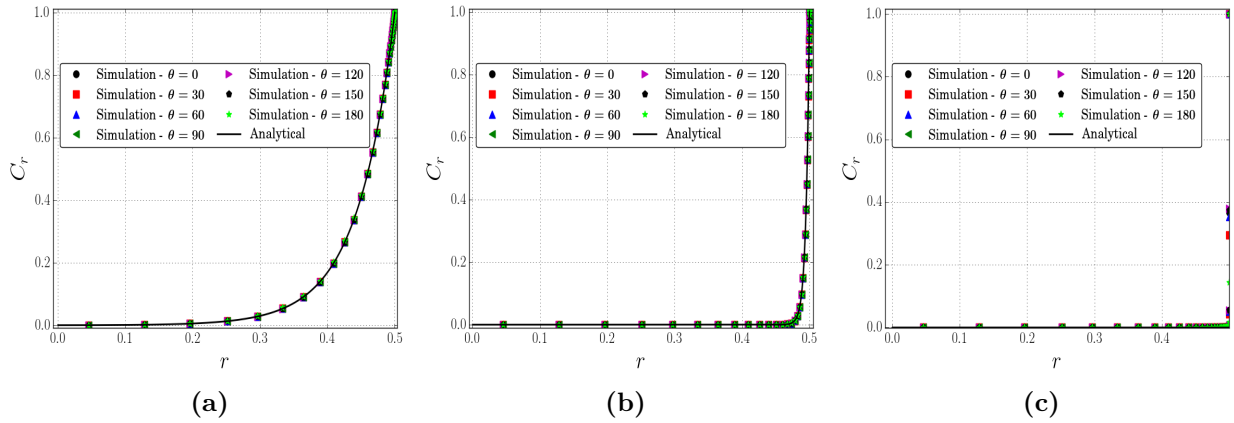
Figure II.14: Concentration profiles C_r inside the particle normalized by the local surface concentration for different angles θ for the three cases that correspond to $Re = 100$, $Sc = 10$ and $\gamma = 0.1$ for different Thiele moduli. a) corresponds to Case B, $\phi = 20$. b) corresponds to Case C, $\phi = 200$. c) corresponds to Case E, $\phi = 2 \cdot 10^4$.

We focus now on the mean volume concentration within the particle which can be determined numerically by integrating the spatial distribution of concentration:

$$\overline{C_v^*} = \frac{6}{\pi d_p^{*3}} \int_0^{2\pi} \int_0^\pi \int_0^{r_p^*} C(r^*, \theta) sin(\theta) r^{*2} d\varphi d\theta dr^* \tag{II.21}$$

When the mean surface concentration $\overline{C_s^*}$ is known, the mean volume concentration can be evaluated analytically as:

$$\overline{C_v^*} = \eta \overline{C_s^*} = \frac{6\overline{C_s^*}}{\phi} \left(\frac{1}{tanh(\phi/2)} - \frac{2}{\phi} \right) \tag{II.22}$$

---

3 Transfer/Reaction in presence of a fluid flow   34

$\overline{C_s^*}$ is estimated by the model (II.12) and therefore the mean volume concentration can be written as follows:

$$\overline{C_v^*} = \frac{3C_\infty^*}{1 + \frac{2\gamma}{Sh}\left(\frac{\phi/2}{tanh(\phi/2)} - 1\right)}\left(\frac{2}{\phi tanh(\phi/2)} - \frac{4}{\phi^2}\right) \tag{II.23}$$

The molar flux towards the particle at steady state is balanced by internal reaction. We can define the factor of enhancement in (II.24) that measures the effect of the chemical reaction to a reference case without any resistance to transfer. This factor for a catalyst particle is defined as the internal rate of reaction inside the particle, to the rate that would be attained with a particle at uniform concentration C_∞^* corresponding to maximum consumption rate. For a reactive catalyst particle experiencing an external convective-diffusive stream, the enhancement factor can be expressed as:

$$\tilde{E} = \frac{\int_0^{2\pi}\int_0^{\pi}\int_0^{r_p^*} -k_s^* C^*(r^*,\theta)sin(\theta)r^{*2}d\varphi d\theta dr^*}{-k_s^* \frac{\pi d_p^{*3}}{6}C_\infty^*} = \frac{3(\phi/2 - tanh(\phi/2))}{\frac{\phi^2}{4}tanh(\phi/2)\left[1 + \frac{2\gamma}{Sh}\left(\frac{\phi/2}{tanh(\phi/2)} - 1\right)\right]} \tag{II.24}$$

Depending on reaction kinetics, the enhancement factor has two asymptotic limits. For very slow reaction, i.e $\phi \ll 1$, the process is kinetics controlled and the catalyst surface concentration is equal to fluid inlet concentration, therefore $\tilde{E} \to 1$. For fast reaction, i.e $\phi \gg 1$, the process is limited by mass transfer and the surface concentration approaches zero, in this case $\tilde{E} \to 1/(1 + \frac{\gamma\phi^2}{6Sh})$ which is lower than one and may be very small for $\phi^2\gamma/Sh \gg 1$.

Figure II.15: Enhancement factor as function of Reynolds number at steady state, $Sc = 1$, $\gamma = 0.1$ and 3 Thiele moduli. Case 1, $\phi = 60$, model represented by dashed-doted line and simulations by blue disks. Case 2, $\phi = 200$, model represented by red line and simulations by red triangles. Case 3, $\phi = 6 \cdot 10^4$ model represented by dashed-doted green line and simulations by green squares.

Part II. Mass transfer from a single particle in a fluid flow coupled with internal diffusion and chemical reaction
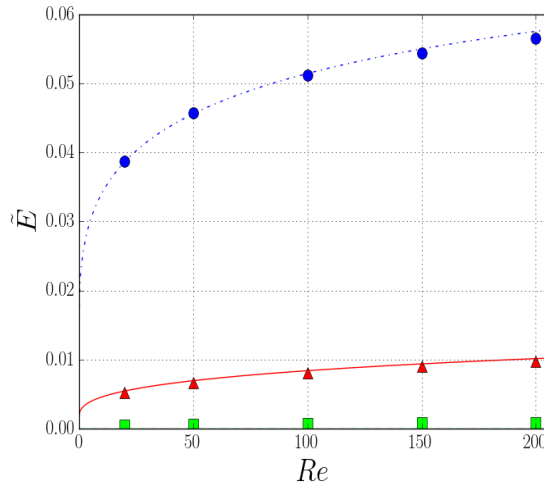

Figure II.16: Enhancement factor as function of Reynolds number at steady state, $Sc = 10$, $\gamma = 0.1$ and 3 Thiele moduli. Case 1, $\phi = 200$, model represented by dashed-doted line and simulations by blue disks. Case 2, $\phi = 632$, model represented by red line and simulations by red triangles. Case 3, $\phi = 6 \cdot 10^4$ model represented by dashed-doted green line and simulations by green squares.

We compare the enhancement factor $\tilde{E} = \eta \dfrac{\overline{C_s^*}}{C_\infty^*} = \dfrac{\overline{C_v^*}}{C_\infty^*}$ from the numerical simulations to the predictions of the model. The results shown in Fig. II.15 and Fig. II.16 correspond to cases presented for mean surface concentration in Fig. II.9 and Fig. II.10, respectively. A slight overestimation of the model occurs at high Reynolds number and $Sc = 10$.

4 Transient evolution

4.1 Unsteady mass balance

The aim of our work is to establish a model for a mass transfer coefficient which accounts for the effect of a first order irreversible reaction along with convection and diffusion. The model depends on mean volume concentration instead of mean surface concentration, and can be used as a closure law in meso-scale simulations such as DEM-CFD, where mean quantities are known at particle scale. In the DEM-CFD framework, the particle concentration is a Lagrangian quantity the evolution of which is integrated over time along the trajectory. Therefore, there is no resolution of the interior of the particle assuming homogeneous concentration. The purpose of our model is indeed to account for internal mass diffusion and reaction due to the coupling of internal and external transport phenomena corresponding to non-uniform concentration distributions that can not be resolved in DEM-CFD (particles are much smaller than the mesh cells). Thus, the mass flux balance is expressed as:

$$\frac{\pi d_p^{*3}}{6} \frac{d\overline{C_v^*}}{dt^*} = -4\pi r_p^{*2} h^* (\overline{C_v^*} - C_\infty^*) - \frac{\pi d_p^{*3}}{6} k_s \overline{C_v^*} \tag{II.25}$$

Part II. Mass transfer from a single particle in a fluid flow coupled with internal diffusion and chemical reaction

Mass conservation yields

$$4\pi r_p^{*2}h^*(\overline{C_v^*} - C_\infty^*) = 4\pi r_p^{*2}k_f^*(\overline{C_s^*} - C_\infty^*) \tag{II.26}$$

where k_f^* is the external mass transfer coefficient referring to concentration difference $\Delta C^* = (\overline{C_s^*} - C_\infty^*)$, and h^* is the overall mass transfer coefficient that accounts for internal and external effects and refers to the mean catalyst particle concentration, $\Delta \overline{C^*} = (\overline{C_v^*} - C_\infty^*)$. Thus, the mass transfer coefficient including the effect of chemical reaction can be obtained as:

$$h^* = k_f^*\frac{\Delta C^*}{\Delta \overline{C^*}} = k_f^*\frac{1 - \tilde{E}/\eta}{1 - \tilde{E}} \tag{II.27}$$

which can be written in a dimensionless form as an effective Sherwood number $\tilde{Sh} = \dfrac{h^*d_p^*}{D_f^*}$.

Substituting the effectiveness and enhancement factors, $\tilde{Sh}(Re, Sc, \phi, \gamma)$ can be written as:

$$\tilde{Sh}(Re, Sc, \phi, \gamma) = \frac{Sh(Re, Sc)}{\dfrac{Sh(Re, Sc)}{2\gamma}\left[\dfrac{tanh(\phi/2)}{\phi/2 - tanh(\phi/2)} - \dfrac{12}{\phi^2}\right] + 1} \tag{II.28}$$

This is equivalent to the additivity rule, i.e., the summation of the resistances to transfer:

$$\frac{1}{\tilde{Sh}} = \frac{1}{2\gamma}\left[\frac{tanh(\phi/2)}{\phi/2 - tanh(\phi/2)} - \frac{12}{\phi^2}\right] + \frac{1}{Sh} \tag{II.29}$$

The model presented in (II.29) has two asymptotic limits. For very fast reaction, i.e when Thiele modulus $\phi \to \infty$, the term $\left[\frac{tanh(\phi/2)}{\phi/2 - tanh(\phi/2)} - \frac{12}{\phi^2}\right] \to 0$ and therefore $\tilde{Sh} \to Sh$. In this case the system is controlled by mass transfer. For very slow reaction, i.e Thiele modulus $\phi \to 0$, the term $\left[\frac{tanh(\phi/2)}{\phi/2 - tanh(\phi/2)} - \frac{12}{\phi^2}\right] \to \infty$ yielding $\tilde{Sh} \to 0$. In this case, mass transfer is controlled by internal reaction kinetics. Between the asymptotic regimes, the system is neither mass transfer nor kinetics controlled. Numerical simulations have been performed and $\tilde{Sh}$ has been calculated numerically according to (II.30) to be compared to our model given by (II.28).

$$\tilde{Sh}_{sim} = \frac{d_p^*}{2(C_\infty^* - \overline{C_v^*})}\int_0^\pi \left(\frac{\partial C^*(r^*, \theta)}{\partial r^*}\right)_{r^*=r_p^*}\sin(\theta)d\theta \tag{II.30}$$

We present two sets of simulation to validate the model. In set 1, we set $Sc = 1$, $\gamma = 0.1$, consider three Thiele moduli : $[\phi = 60$, Case 1], $[\phi = 200$, Case 2] and $[\phi = 6 \cdot 10^4$, Case 3], and vary Re from 20 to 200. In set 2, we set $Sc = 10$, $\gamma = 0.1$, consider three Thiele moduli : $[\phi = 200$, Case 1], $[\phi = 632$, Case 2] and $[\phi = 2 \cdot 10^4$, Case 3], and vary Re from 20 to 200. Computed results from sets 1 and 2 are plotted in FIG. II.17 and FIG. II.18, respectively. They show a very good agreement with the predictions of our model.
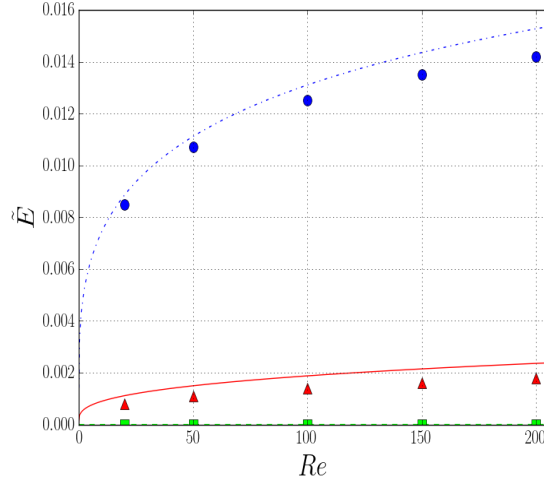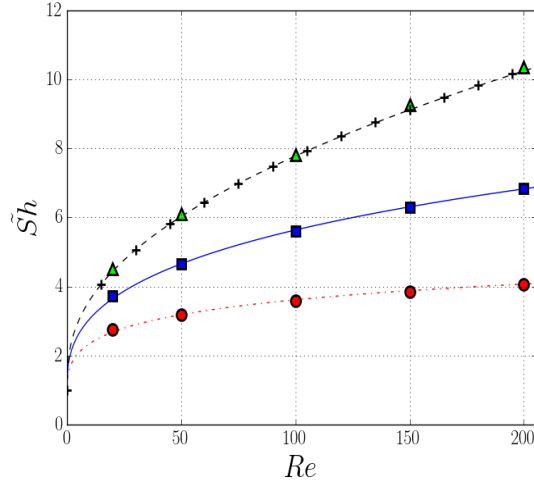
Figure II.17: $\tilde{Sh}$ as function of Reynolds number at steady state, $Sc = 1$, $\gamma = 0.1$ and three Thiele moduli. Case 1, $\phi = 60$, model represented by red dashed-doted line and simulation results by disks. Case 2, $\phi = 200$, model represented by blue continuous line and simulation results by squares. Case 3, $\phi = 6 \cdot 10^4$, model represented by red dashed line and simulation results by triangles. The + markers correspond to the correlation of (Feng and Michaelides [2000]).
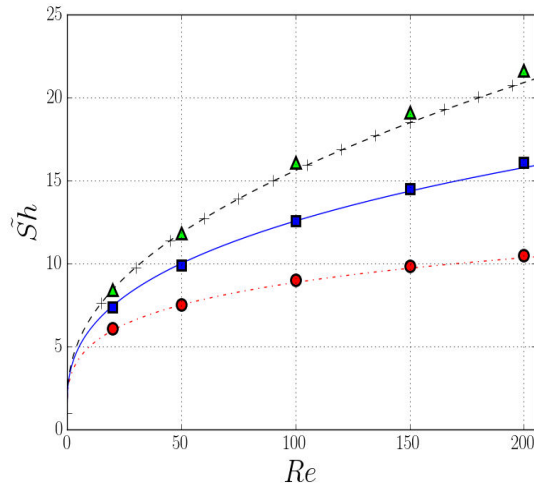
Figure II.18: $\tilde{Sh}$ as function of Reynolds number at steady state, $Sc = 10$, $\gamma = 0.1$ and three Thiele moduli . Case 1, $\phi = 200$, model represented by red dashed-doted line and simulation results by disks. Case 2, $\phi = 632$, model represented by blue continuous line and simulation results by squares. Case 3, $\phi = 2 \cdot 10^4$, model represented by red dashed line and simulation results by triangles. The + markers correspond to the correlation of (Feng and Michaelides [2000]).

4.2   Transient evolution of catalyst bead concentration

We consider here a particle of mean initial volume concentration $\overline{C_v^*}(t^* = 0) = 0$, placed in a steady stream of uniform concentration C_∞^*. A first order reaction is taking place within the particle. The temporal evolution of the mean volume

concentration within the particle is described by (II.25), which can be written in a dimensionless form as follows:

$$\frac{d\overline{C_v}}{dt} = -(\overline{C_v} - 1) - k_s\overline{C_v} \tag{II.31}$$

with $\overline{C_v} = \overline{C_v^*}/C_\infty^*$ and $k_s = k_s^* d_p^*/6h^*$. At steady state, $\dfrac{d\overline{C}}{dt} = 0$, which yields the mean volume concentration as:

$$\overline{C_f} = \left(1 + \frac{k_s^* d_p^*}{6h^*}\right)^{-1} = \left(1 + \frac{\gamma\phi^2}{6\tilde{Sh}}\right)^{-1} \tag{II.32}$$

$\overline{C_f}$ is equal to the mean volume concentration found by the steady balance in (II.23) normalized by C_∞. The analytic solution of (II.31) is:

$$\overline{C_v}(t) = \overline{C_f}\left(1 - exp\left(\frac{-t}{\overline{C_f}}\right)\right) \tag{II.33}$$

where $t = t^*/\tau^*$ is the dimensionless time and $\tau^* = d_p^*/6h^*$ with $h^* = \tilde{Sh}D_f^*/d_p^*$ is the mass transfer coefficient given by (II.28).

We compare the unsteady predictions of the model to computed results through two sets of simulations (each of them at a fixed Reynolds number). In set 1, we set $Re = 200$, $Sc = 10$, $\gamma = 0.1$ and vary ϕ from 0.6 to 20. We plot the results in Fig. II.19. In set 2, we set $Re = 100$, $Sc = 1$, $\gamma = 0.1$ and vary ϕ from 0.88 to 28.2. We plot the results in Fig. II.20. The model has shown its ability to predict the characteristic time of the mean concentration evolution and a good agreement has been observed between the model and the numerical simulations, although we assumed the mass transfer rate to be constant. The transient model allows to estimate the time needed for a catalyst bead to reach its steady mean concentration. Typically, the characteristic time is less than a second for a gas-solid system and around tens of seconds for liquid-solid systems.
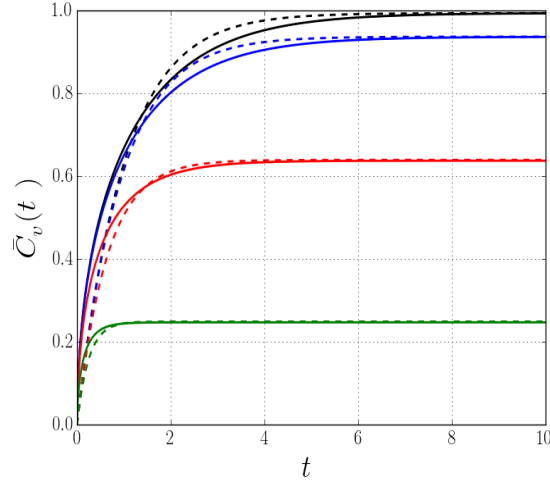
Figure II.19: Temporal evolution of the dimensionless mean volume concentration, model comparison with simulation for $Re = 200$, $Sc = 10$, $\gamma = 0.1$ and four Thiele moduli. Model represented by dashed and simulation by continuous lines, respectively. Case1, $\phi = 0.6$ - black color. Case 2, $\phi = 2$ - blue color. Case 3, $\phi = 6$ - red color. Case 4, $\phi = 20$ - green color.
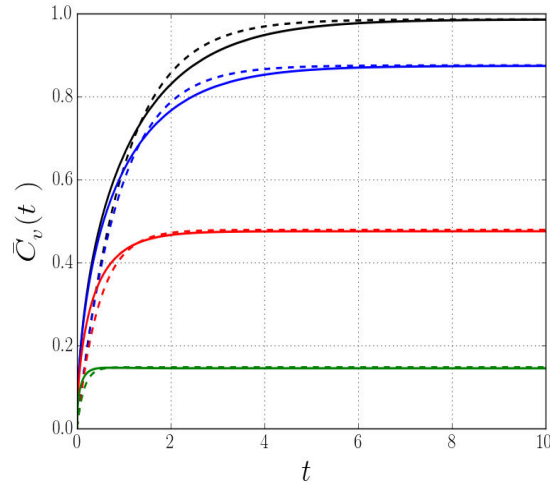
Figure II.20: Temporal evolution of the dimensionless mean volume concentration, model comparison with simulation for $Re = 100$, $Sc = 1$, $\gamma = 0.1$ and four Thiele moduli. Model represented by dashed and simulation by continuous lines, respectively. Case1, $\phi = 0.88$ - black color. Case 2, $\phi = 2.8$ - blue color. Case 3, $\phi = 8.8$ - red color. Case 4, $\phi = 28.2$ - green color.

5 Conclusion and future work

We investigated mass transfer for a system composed of an isolated solid spherical catalyst particle placed within a fluid stream. Reactant diffuses from the fluid phase to the solid phase where a first order irreversible chemical reaction takes place. The problem is treated by coupling external convection-diffusion in the fluid phase to diffusion-reaction in the solid phase through appropriate boundary conditions,

namely continuity of concentration and continuity of flux at the particle interface. We solved the whole problem in two ways: (i) through boundary fitted numerical simulations of the full set of equations and (ii) through a simple semi-analytical approach that couples a correlation for the external transfer to an analytical solution of the internal diffusion-reaction equation. The interplay between the different transport phenomena can be quantified through an effective Sherwood number assuming steady state. The prediction of this effective Sherwood number in such systems has a key role in terms of modeling while it allows to estimate the equilibrium internal mean concentration of the particle without using the determination of the surface concentration (unknown in such situations).

The model has been validated step by step. To start with, a diffusion-reaction problem has been considered in the absence of convection in the fluid phase. In this case, the external Sherwood number has an analytical solution $Sh = 2$. This allows to find the analytical solution for the surface concentration at steady state and to test the accuracy of our numerical simulations. Then, the particle was exposed to an external fluid stream with an inlet concentration C_∞. In this case, the mean surface concentration has been modeled using a classical correlation for the mass transfer coefficient. Our model was compared with numerical simulations over a wide range of dimensionless parameters. Both mean surface and mean volume concentrations predicted by our model showed a satisfactory agreement with numerical simulation results. This satisfactory agreement also support that notion that the assumptions of the model are appropriate.

An expression for the mass tranfer coefficient that accounts for internal and external effects in the system has been proposed, via general mass balance for the system and equivalently using additivity rule of resistances to mass transfer. It has also been validated through comparison with numerical simulations. The major result of our study is that our simple model based on decoupled treatment of internal and external mass transfer gives very accurate results. The asymptotic limits of the model have been analyzed and are in accordance with general expectations for slow and fast reaction rates. Finally, the unsteady response on the system has been tested. A model that predicts the time evolution of the mean volume concentration has been established. It is in a very good agreement with unsteady simulations results.

Possible extensions of this model are as follows. To be useful for engineering applications, such model should include the effect of neighboring particles corresponding to situations at higher solid volume fraction as a fixed bed or a fluidized bed. The effect of the particle volume fraction can be investigated with a particle-resolved numerical approach that solves both internal and external mass balances either with a boundary fitted mesh (Partopour and Dixon [2017a]) or with an immersed boundary/ghost fluid method (Shao et al. [2012]). Another extension of our work is to address more complex chemical reactions as, e.g., different reaction kinetics, second order reactions or multiple reactions with additional species.

Part II. Mass transfer from a single particle in a fluid flow coupled with internal diffusion and chemical reaction

Acknowledgments

Part III

Three interacting spheres in a row : coupling mass transfer and chemical reaction

This chapter has been submitted to Chemical Engineering Science and it is in revision process.

Contents

Coupling the fictitious domain and sharp interface methods for the simulation of convective mass transfer around reactive particles: towards a reactive Sherwood number correlation for dilute systems

Mostafa Sulaiman[a], Abdelkader Hammouti[a], Eric Climent[b], Anthony Wachs[c,d]

[a] IFP Énergies Nouvelles, Fluid Mechanics Department, Rond-point de l'échangeur de Solaize, BP 3, 69360 Solaize, France
[b] Institut de Mécanique des Fluides de Toulouse (IMFT) Université de Toulouse,CNRS - Toulouse, France
[c] Department of Mathematics, University of British Columbia, 1984 Mathematics Road, Vancouver, BC V6T 1Z2, Canada
[d] Department of Chemical and Biological Engineering, University of British Columbia, 2360 East Mall, Vancouver, BC V6T 1Z3, Canada

Abstract

Keywords: Sharp Interface Method, Catalyst particle Mass transfer Sherwood number Chemical reaction Thiele modulus.

We suggest a reactive Sherwood number model for convective mass transfer around reactive particles in a dilute regime. The model is constructed with a simple external-internal coupling and is validated with Particle-Resolved Simulation (PRS). The PRS of reactive particle-fluid systems requires numerical methods able to handle efficiently sharp gradients of concentration and potential discontinuities of gradient concentrations at the fluid-particle interface. To simulate mass transfer from reactive catalyst beads immersed in a fluid flow, we coupled the Sharp Interface Method (SIM) to a Distributed Lagrange Multiplier/Fictious Domain (DLM/FD) two-phase flow solver. The accuracy of the numerical method is evaluated by comparison to analytic solutions and to generic test cases fully resolved by boundary fitted simulations. A previous theoretical model that couples the internal diffusion-reaction problem with the external advection-diffusion mass transfer in the fluid phase is extended to the configuration of three aligned spherical particles representative of a dilute particle-laden flow. Predictions of surface concentration, mass transfer coefficient and chemical effectiveness factor of catalyst particles are validated by DLM-FD/SIM simulations. It is shown that the model captures properly the effect of an internal first order chemical reaction on the overall respective reactive Sherwood number of each sphere depending on their relative positions. The proposed correlation for the reactive Sherwood number is based on an existing non-reactive Sherwood number correlation. The model can be later used in Euler/Lagrange or Euler/Euler modelling of dilute reactive particle-laden flows.

Graphical Abstract

(a) $Re = 50$, $\gamma = 0.1$, $Sc = 1$ and $\phi^2 = 40$

(b) $Re = 50$, $\gamma = 0.1$, $Sc = 1$ and $\phi^2 = 200$

(c) $Re = 50$, $\gamma = 0.1$, $Sc = 1$ and $\phi^2 = \infty$
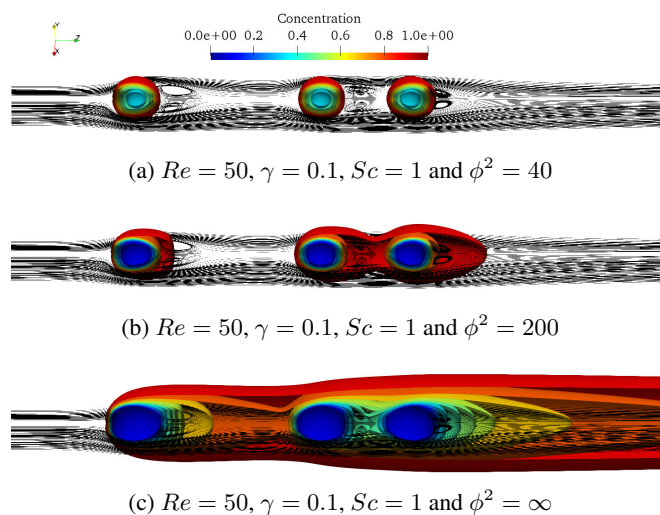
1 Introduction

Systems involving interactions of a dispersed solid phase with a continuous fluid phase through momentum, heat and mass transfer are ubiquitous in a wide range of industrial and energetic processes. A classical process in the chemical enginering industry is catalytic cracking in a reactor. If the dispersed solid phase, commonly referred to as particles, is fixed in the reactor, the system is known as a fixed bed and the flow is relevant of the flow through a porous medium represented by the network of randomly stacked catalytic particles [Furuta et al., 2006]. If particles are mobile, the system is known as a fluidized bed [Gidaspow, 1994, Montero et al., 2018]. In both reactors, the fluid enters the system with an imposed concentration of reactants and reactants are transferred from fluid phase bulk to catalytic particles bulk through diffusion, where chemical reactions take place in the form of heterogeneously catalyzed gas or liquid reaction. The modeling, operation, design and optimization of these systems necessitate an advanced comprehension of the coupling among the dominant transfer phenomena, namely momentum, heat, and mass transfer, that are usually associated to the presence of chemical reactions. For decades, operating experimental setups and deriving simplified analytical solutions were the two only ways to improve the comprehension of these systems. With the emergence of robust, accurate and computationally efficient numerical approaches/methods, we can complement and extend our comprehension with, e.g., reliable information about the micro-scale interactions in these systems that are not accessible through experiments or theory.

Over the past two decades, diverse Computational Fluid Dynamics (CFD) approaches/methods for the simulation of systems involving fluid/solid interactions have been developed. Combined to the increasing power of supercomputers that now enables one to perform Direct Numerical Simulations (DNS) at the scale of particles, CFD tools are now capable of supplying reliable and high quality detailed data in the flow. In this class of highly resolved CFD methods, Particle Resolved Simulation (PRS) has arisen as a mature method able to provide reliable local information about momentum, heat and mass transfer at the particle scale in particulate flows (Sun et al. [2016] among many others). PRS methods can be classified into two categories:

The first category comprises body-fitted mesh methods. The advantage of this type of method relies on the ease to enforce boundary conditions at the particle surface, i.e., at the fluid/particle interface. This technique has been used to investigate transport properties in a bed made of multiple fixed particles by Romkes et al. [2003], Augier et al. [2010a] and convective heat/mass transfer over a single particle by Feng and Michaelides [2000]. It has also been employed for moving particles by Hu et al. [2001] and moving boundaries by Duarte et al. [2004].

The second category comprises fixed mesh methods. The challenge of this type of method is the difficulty in enforcing the correct boundary conditions at the particle surface while the main advantage is the use of a regular cartesian grid. The Immersed Boundary Method (IBM) uses Lagrangian markers at the particle surface to impose boundary conditions and introduces an additional forcing term [Uhlmann,

2005]. Xia et al. [2014] applied IBM to study convective heat/mass transfer over a single particle. IBM was also used to evaluate the heat transfer Nusselt number in dense particulate flow systems by Deen et al. [2014] and Sun et al. [2015]. Both studies compared their results to the pioneering experimental work of Gunn [1978] and proposed corrections of Gunn's correlation based on their data sets. Recently, IBM has been used by Lu et al. [2018] to examine mass transfer in particulate flows with surface reaction. The Lattice Boltzmann Method (LBM) is another computational method that uses a fixed mesh. LBM has also been applied to particulate flows with heat transfer by Khiabani et al. [2010] and Kruggel-Emden et al. [2016]. Unlike conventional discretization schemes that solve the classical conservation equations, LBM solves convection-collision steps of probability density functions. Finally, the Distributed Lagrange Multiplier / Fictitious Domain Method (DLM/FD), firstly introduced by Glowinski et al. [2001], combines the particle and fluid equations of motion into a single, weak, and general equation of motion called combined momentum equation. The combined equations are derived through the combined velocity space incorporating the rigid body motion (no-slip) in the particle. The DLM/FD method has been extended to treat heat/mass transfer by Yu et al. [2006], Dan and Wachs [2010] and Wachs [2011b].

Apart from Yu et al. [2006] that considered diffusion inside particles, the common feature of the aforementioned fixed-mesh methods is that they solve the convection-diffusion equation by enforcing a uniform temperature (or concentration) in the whole solid particle volume. This type of method is inadequate for the treatment of systems where temperature/concentration gradients are prominent within the particle. In this case, the convection-diffusion (or convection-diffusion-reaction) equation must be solved in both domains, i.e., in the solid domain and in the fluid domain. Augier et al. [2010b] used a Volume of Fluid method (VOF) to study the efficiency of partially-wetted stacked catalyst particles. Catalyst efficiency was studied for different particles shapes as a function of Thiele modulus. Haroun et al. [2010] employed a VOF method to study interfacial-reactive mass transfer in two-phase flows. Although efficient, the VOF method necessitates a highly refined mesh at interfaces in order to accurately enforce the correct boundary conditions, which may render, for a fixed Cartesian mesh, the method computationally inefficient due to the huge computational cost. The main drawback of the VOF method is that it is not capturing discontinuities.

The Sharp Interface Method (SIM), also referred to as Ghost Fluid Method (GFM), is a fixed-mesh numerical method used to accurately capture boundary conditions with discontinuities along embedded interfaces [Shi et al., 2011]. In the SIM, jump conditions are incorporated in the discretization of the differential operators on the Cartesian grid in the vicinity of the interface. SIM was firstly introduced by Fedkiw et al. [1999] and employed to impose boundary conditions at a contact discontinuity in the inviscid Euler equations. SIM was later extended to treat more general discontinuities by Liu et al. [2000]. In their work, Liu et al. [2000] developed a version of SIM to address the problem of inhomogeneous Poisson equation in the presence of interfaces. The method is easy to implement in three dimensions and the matrix associated to the discrete Laplacian operator remains symmetric, allow-

ing to use 'black box' scientific libraries to solve the corresponding linear system. Gibou et al. [2002] considered the Poisson equation with a non-uniform coefficient and Dirichlet boundary conditions on an irregular domain and showed that a second order accuracy can be obtained with a simple discretization scheme that also preserves the matrix symmetry. Udaykumar and Mao [2002] and Gibou et al. [2003] employed the SIM to track the evolution of solidification fronts in the presence of heat and solute transport in the dendritic solidification of aqueous salt solutions. Kang et al. [2000] extended the SIM to treat multiphase incompressible flows including effects of viscosity, surface tension and gravity and applied the method to two-phase water-air mixtures. Marella et al. [2005] used a SIM to simulate immersed boundary problems while Liu et al. [2005] simulated droplet interactions with objects of different shapes using a SIM that accounts for surface tension and viscosity jumps. Kapahi et al. [2013] used a modified SIM to treat interfaces of embedded objects, with an application to shock-wave particulate flows. Finally, to end this non-exhaustive list of SIM-related works, Shao et al. [2012] combined the SIM with a Fictitious Domain method to simulate heat transfer in particulate flows with heat diffusion inside particles.

PRS is very powerful to supply high quality data inside the flow but is still limited to up to a few thousands, at best a few tens of thousands, of particles due to the large computing cost of these simulations. Finely resolved simulations as PRS can easily comprise hundreds of millions, and even a few billions, of grid cells, that represent highly challenging parallel computing problems, whether on multi-CPU or the emerging GPU/multi-GPU technology. Thereby, from a modelling viewpoint, there has been a sustained appeal to combine these particle-scale models to larger scale models, namely Euler/Lagrange at the so-called meso scale and Eulere/Euler at the so-called macro scale. The conceptual features of a fully integrated multi-scale modeling of particle-laden flows is comprehensively described by Deen et al. [2014]. The vast majority of the multi-scale approaches suggested in the field of particle-laden flows assume a bottom-up strategy or phrased in a more emphatic way an upwards cascade of knowledge. In short, what is learnt through highly resolved simulations at the micro scale on small representative systems is meant to be transferred to higher scale models and to contribute to a deeper understanding of the particle-laden flow dynamics. Among the assorted ways to transfer knowledge, the most popular way has undoubtedly been over the last 15 years to enhance existing correlations for dimensionless numbers representative of momentum, heat or mass transfer. Among many others, Deen et al. [2014] and Sun et al. [2015] suggested corrections to enhance the Nusselt number correlation suggested by Gunn [1978] 30 years earlier. Our objective in this paper follows the same line, i.e., to suggest a new correlation or to enhance an existing correlation derived from micro scale PRS that can be later used in meso scale Euler/Lagrange and macro scale Euler/Euler modelling.

In the present study, we combine a Fictitious Domain method and a first order Sharp Interface method to investigate mass transfer in particulate flows in the presence of a first order reaction inside particles. The 3D simulation results supplied by this computational Method in a flow configuration representative of dilute

particle-laden flows are used to assess the validity of a reactive Sherwood number correlation that we already suggested for the case of a single sphere in an unbounded domain in Sulaiman et al. [2018a] and that we revisit later in this work. We intend to show that a reactive Sherwood number correlation can be constructed based on simple external-internal coupling. The obtained model relies on any non-reactive Sherwood number correlation available in the literature and is deemed to perform well. The rest of the paper is organized as follows. We shortly summarized in *Section 1* the equations and the corresponding dimensionless numbers governing the problem. *Section 3* elaborates on the features of our numerical method that combines a DLM/FD method to compute the flow field and a SIM to compute the chemical species concentration field. Then, we present in *Section 4* a series of validation tests of growing complexity involving a single sphere. We start with diffusion, then move on with diffusion-reaction, convection-diffusion, and finally consider convection-diffusion-reaction. In the last case, and due to the lack of analytical solutions and previously established correlations to compare our numerical results to, we perform a comparison between SIM and a body-fitted method that fully resolves the interface to investigate the efficiency of our SIM method and determine its limits of validity in terms of range of dimensionless parameters considered and grid size, through a series of convergence tests. We also show, through comparison in a diffusion-reaction case, the advantage of SIM over VOF. Finally, and this is the core of this work, we investigate in *Section 5* the problem of three interacting spheres, firstly presented by Ramachandran et al. [1989] for heat transfer without diffusion and chemical reaction inside the spheres, with mass transfer coupled to diffusion and chemical reaction inside the spheres. We test our reactive Sherwood number correlation on this configuration. The validity of the model and the steps forward in extending/improving our reactive Sherwood number correlation are discussed in *Section 6*.

2   Governing equations

We aim at solving the time-dependent and incompressible flow of a Newtonian fluid past multiple fixed obstacles with mass transfer between the fluid and the solid obstacles. We define the full flow domain as Ω, the part of Ω occupied by the solid obstacles as P and the part of Ω occupied by the fluid as $\Omega \backslash P$. The problem is governed by the following conservation equations: fluid mass conservation, fluid momentum conservation and chemical species conservation. Here we assume a single chemical species C at a low concentration in the fluid such that it does not affect the constant density and viscosity of the fluid. Dimensional quantities are distinguished from dimensionless quantities by a "*" superscript. We denote $\boldsymbol{u}^*$ the fluid velocity, p^* the fluid pressure, C_f^* the chemical species concentration in the fluid and C_s^* the chemical species concentration in the solid. The chemical species is assumed to undergo a first order reaction in the solid obstacles. With appropriate initial conditions in Ω on $(\boldsymbol{u}^*, C_f^*, C_s^*)$ and boundary conditions on $\partial\Omega$, the boundary of Ω, on $\boldsymbol{u}^*$ (and potentially on p^*), the set of conservation equations together with fluid/solid interface conditions is written as follows:

Part III. Three interacting spheres in a row : coupling mass transfer and chemical reaction

in the fluid

$$\rho_f^* \left(\frac{\partial \boldsymbol{u}^*}{\partial t^*} + (\boldsymbol{u}^* \cdot \nabla) \boldsymbol{u}^* \right) - \eta^* \nabla^2 \boldsymbol{u}^* + \nabla p^* = \boldsymbol{0}, \tag{III.1}$$

$$\nabla \cdot \boldsymbol{u}^* = 0, \tag{III.2}$$

$$\frac{\partial C_f^*}{\partial t^*} + \boldsymbol{u}^* \cdot \nabla C_f^* - \nabla \cdot (D_f^* \nabla C_f^*) = 0, \tag{III.3}$$

where ρ_f^* denotes the fluid density, η^* the fluid viscosity and D_f^* the chemical species diffusion coefficient in the fluid.

in the solid

$$\boldsymbol{u}^* = 0, \tag{III.4}$$

$$\frac{\partial C_s^*}{\partial t^*} - \nabla \cdot (D_s^* \nabla C_s^*) = -k_s^* C_s^*, \tag{III.5}$$

where D_s^* denotes chemical species effective diffusion coefficient in the solid and k_s^* the effective first order reaction constant in the solid.

at the fluid/solid interface ∂P

$$\boldsymbol{u}^* = 0, \tag{III.6}$$

$$C_s^* = C_f^*, \tag{III.7}$$

$$-D_s^* \frac{\partial C_s^*}{\partial \boldsymbol{n}} = -D_f^* \frac{\partial C_f^*}{\partial \boldsymbol{n}}, \tag{III.8}$$

where $\boldsymbol{n}$ denotes the unit normal vector at the fluid/solid interface.

Governing equations are made dimensionless by introducing a characteristic length L_c^*, a characteristic velocity U_c^* and a characteristic convective time $T_c^* = L_c^*/U_c^*$. In the various problems examined thereafter, solid obstacles are spheres, hence an obvious choice for L_c^* is the particle diameter d_p^*. When the problem is not purely diffusive, an obvious choice for U_c^* is the far field inlet velocity U_{in}^*. Also, by normalizing the chemical species concentration between 0 and 1 and introducing the chemical species diffusion coefficient ratio $\gamma = \frac{D_s^*}{D_f^*}$, conservation equations (III.3) and (III.5) together with interface conditions (III.7)-(III.8), i.e., continuity of chemical species concentration and continuity of chemical species normal flux, can be recast into a single dimensionless conservation equation for the chemical species C with appropriate no jump conditions at the fluid/solid interface on the chemical species concentration and on its normal flux. The set of dimensionless equations eventually reads as follows:

$$\frac{\partial \boldsymbol{u}}{\partial t} + (\boldsymbol{u} \cdot \nabla) \boldsymbol{u} - \frac{1}{Re} \nabla^2 \boldsymbol{u} + \nabla p = \boldsymbol{0} \quad \text{in} \quad \Omega \backslash P, \tag{III.9}$$

$$\nabla \cdot \boldsymbol{u} = 0 \quad \text{in} \quad \Omega \backslash P, \tag{III.10}$$

$$\boldsymbol{u} = \boldsymbol{0} \quad \text{in} \quad P \cup \partial P, \tag{III.11}$$

$$\frac{\partial C}{\partial t} + \boldsymbol{u} \cdot \nabla C - \nabla \cdot \left(\frac{h(\gamma)}{Pe} \nabla C \right) + \frac{h(\gamma) g(\phi^2)}{Pe} C = 0 \quad \text{in} \quad \Omega,$$

$$[C]_{\partial P} = 0 \quad , \quad \left[h(\gamma) \frac{\partial C}{\partial \boldsymbol{n}} \right]_{\partial P} = 0, \tag{III.12}$$

where $[\ ]_{\partial P}$ represents the jump condition across the fluid/solid interface. The dimensionless numbers introduced above are defined as follows:

— Reynolds number: $Re = \dfrac{\rho_f^* U_c^* L_c^*}{\eta^*}$,

— Peclet number: $Pe = \dfrac{U_c^* L_c^*}{D_f^*}$,

— Damkohler number: $Da = \phi^2 = \dfrac{k_s^* L_c^{*2}}{D_s^*}$

where $\phi = \sqrt{Da}$ is the Thiele modulus, and the functions $h(\gamma)$ and $g(\phi^2)$ are simple Heavyside-like functions defined as:

$$h(\gamma) = \begin{cases} 1 & \text{in} \quad \Omega \backslash P, \\ \gamma & \text{in} \quad P. \end{cases}$$

$$g(\phi^2) = \begin{cases} 0 & \text{in} \quad \Omega \backslash P, \\ \phi^2 & \text{in} \quad P. \end{cases}$$

As usual, we can also introduce a Schmidt number $Sc = \dfrac{\eta^*}{\rho_f^* D_f^*}$ such that $Pe = Re \cdot Sc$. Hence the flow is equivalently characterized by the pair (Re, Pe) or the pair (Re, Sc).

3 Numerical Model

The chemical species problem is one-way coupled only to the fluid problem through the velocity field $\boldsymbol{u}$. At each discrete time t^{n+1}, $n > 0$ being the time index and t^0 being the initial time, we solve the full problem as a sequence of the fluid problem followed by the chemical species problem using the computed velocity field $\boldsymbol{u}^{n+1}$. The solution algorithm is hence of the 1st order in time weak coupling type. In the next subsections, we shortly elaborate on the strategy adopted to solve each sub-problem.

3.1 Solution to the fluid problem: flow around fixed obstacles

We use our well validated Finite Volume/Staggered Grid-DLM/FD solver implemented in our in-house code PeliGRIFF. The whole method is fully detailed in Wachs et al. [2015], Rahmani and Wachs [2014] for freely moving particles and in Dorai et al. [2015] for fixed obstacles and was pionneered by Glowinski et al. [1999] in a Finite Element context. To summarize, we use a cartesian structured mesh of constant grid size around obstacles, we solve the fluid conservation equations (III.9)-(III.10) everywhere in the domain (not only in $\Omega \backslash P$ but in the entire Ω) and we enforce the rigid body motion (motionless in the particular case of the application treated in this paper) in the region (filled with fictitious fluid) occupied

by the obstacles and represented by (III.11) using a distributed Lagrange multiplier field. Our Finite Volume/Staggered Grid-DLM/FD method also involves an implicit solution of the resulting DLM/FD saddle-point problem by a Uzawa algorithm, a collocation-point method to discretize the solid obstacles on the fluid mesh and a second-order interpolation of the fluid velocity at the particle boundary [Wachs et al., 2015, Rahmani and Wachs, 2014, Dorai et al., 2015]. In our Finite Volume/Staggered Grid discretization method, the diffusive term is discretized with a 2nd order accurate centered scheme while the advective term is discretized with a 2nd order accurate TVD (Total Variation Diminishing)/Superbee limiter scheme. Finally, the diffusive term is treated implicitly in time with a 2nd order Crank-Nicholson scheme while the advective term is treated explicitly in time with a 2nd order Adams-Bashforth scheme. The strength of our method is that it does not require any kind of hydrodynamic radius calibration (see Wachs et al. [2015] for more detail about the problem of hydrodynamic radius calibration). The overall spatial accuracy of the discretization scheme is however not fully 2nd order due to the non-boundary fitted feature of the mesh around the solid obstacles. The dimensionless mesh size Δx is related to the number of points per sphere diameter through $N_p = 1/\Delta x$.

The solution algorithm for the fluid problem is of the 1st order operator-splitting type and comprises two stages as follows: A classical L2-projection scheme for the solution of the Navier & Stokes problem: find $\boldsymbol{u}^{n+1/2}$ and p^{n+1} such that

$$
\begin{aligned}
\frac{\tilde{\boldsymbol{u}} - \boldsymbol{u}^n}{\Delta t} - \frac{1}{2Re}\nabla^2\tilde{\boldsymbol{u}} &= -\nabla p^{n+1} + \frac{1}{2Re}\nabla^2\boldsymbol{u}^n \\
&\quad - \frac{1}{2}\left(3\boldsymbol{u}^n\cdot\nabla\boldsymbol{u}^n - \boldsymbol{u}^{n-1}\cdot\nabla\boldsymbol{u}^{n-1}\right) - \boldsymbol{\lambda}^n,
\end{aligned}
\tag{III.13}
$$

$$
\nabla^2\psi = \frac{1}{\Delta t}\nabla\cdot\tilde{\boldsymbol{u}} \ , \ \frac{\partial\psi}{\partial n} = 0 \text{ or } \psi = 0 \text{ on } \partial\Omega,
\tag{III.14}
$$

$$
\boldsymbol{u}^{n+1/2} = \tilde{\boldsymbol{u}} - \Delta t\nabla\psi,
$$
$$
p^{n+1} = p^n + \psi - \frac{\Delta t}{2Re}\nabla^2\psi.
\tag{III.15}
$$

A fictitious domain problem: find $\boldsymbol{u}^{n+1}$ and $\boldsymbol{\lambda}^{n+1}$ such that

$$
\frac{\boldsymbol{u}^{n+1} - \boldsymbol{u}^{n+1/2}}{\Delta t} + \boldsymbol{\lambda}^{n+1} = \boldsymbol{\lambda}^n,
\tag{III.16}
$$

$$
\boldsymbol{u}^{n+1} = \boldsymbol{0} \ \text{in } P.
\tag{III.17}
$$

where $\tilde{\boldsymbol{u}}$, $\boldsymbol{\lambda}$, ψ and Δt denote the non divergence-free predicted fluid velocity vector, DLM/FD Lagrange multiplier to relax the constraint (III.17), pseudo-pressure field and time step, respectively.

3.2 Solution to the chemical species problem: Sharp Interface method

The conservation equation in problem (III.12) is discretized in time with a 1st order scheme. The diffusive term is treated implicitly in time with a 1st order Backward Euler scheme and the advective term is discretized explicitly in time with a 2nd order Adams-Bashforth scheme. Since the reactive term is linear with C, it

can be easily treated implicitly too. The discrete in time version of the conservation equation in problem (III.12) reads as follows:

$$\frac{C^{n+1} - C^n}{\Delta t} - \nabla \cdot \left(\frac{h(\gamma)}{Pe} \nabla C^{n+1} \right) + \frac{h(\gamma) g(\phi^2)}{Pe} C^{n+1} =$$
$$-\frac{1}{2} \left(3\boldsymbol{u}^{n+1} \cdot \nabla C^n - \boldsymbol{u}^n \cdot \nabla C^{n-1} \right) \quad \text{(III.18)}$$

The primary difficulty in the spatial discretization of (III.18) is how to discretize the diffusive operator on a non-boundary fitted mesh and to account for the continuity of C and of its normal flux across the fluid/solid interface through the 2 no jump conditions $[C]_{\partial P} = 0$ and $\left[h(\gamma) \dfrac{\partial C}{\partial \boldsymbol{n}} \right]_{\partial P} = 0$, respectively. This is achieved with a Sharp Interface Method [Fedkiw et al., 1999, Liu et al., 2000, Shao et al., 2012]. We use the original version suggested by Fedkiw et al. [1999]. The method is only 1st order accurate in space but is discontinuity capturing and easy to implement. The core of the method is to incorporate the jump conditions into the discrete in space diffusive term. The other terms in (III.18) are discretized in a classical way. Since the method is well established, we simply shortly summarized its construction in 1D and the extension to 3D suggested by Shao et al. [2012] in the special case of spherical solid bodies.

Description of the Sharp Interface Method in one dimension

To ease notation, let's rewrite $\frac{h(\gamma)}{Pe}$ as β. β is hence a diffusion coefficient with a discontinuity across the fluid/solid interface. We shortly elaborate below on the discretization of the diffusive term $\nabla \cdot (\beta \nabla C)$ in 1D, i.e., $(\beta C_x)_x$, with $x = \frac{\partial}{\partial x}$.

We consider general jump conditions on C and on its flux defined at the interface ∂P as:

$$\left[C \right]_{\partial P} = C^+_{\partial P} - C^-_{\partial P} = a_{\partial P} \quad \text{(III.19)}$$

$$\left[\beta C_x \right]_{\partial P} = \left(\beta C_x \right)^+_{\partial P} - \left(\beta C_x \right)^-_{\partial P} = b_{\partial P} \quad \text{(III.20)}$$

where Ω^- denotes the part of the domain on one side of the interface (e.g., $\Omega^- = \Omega \backslash P$ is the fluid domain) and Ω^+ denotes the part of the domain on the other side of the interface (e.g., $\Omega^+ = P$ is the solid domain). We assume that the 1D space is discretized uniformly with a constant grid size Δx and that the interface ∂P lies between two grid points $i \in \Omega^-$ and $i+1 \in \Omega^+$. Following Fedkiw et al. [1999], Liu et al. [2000], the diffusive term $(\beta C_x)_x$ for point i is discretized in a Finite Difference fashion as follows:

$$\left(\beta C_x \right)_x =$$
$$\frac{1}{\Delta x} \left[\hat{\beta} \left(\frac{C_{i+1} - C_i}{\Delta x} \right) - \beta^- \left(\frac{C_i - C_{i-1}}{\Delta x} \right) \right] - \frac{\hat{\beta} a_{\partial P}}{\Delta x^2} - \frac{\hat{\beta} b_{\partial P} (1 - \zeta)}{\beta^+ \Delta x} \quad \text{(III.21)}$$

where the coefficient $\hat{\beta}$ is calculated as follows:

$$\hat{\beta} = \frac{\beta^+ \beta^-}{\beta^+ \zeta + \beta^- (1 - \zeta)} \quad \text{(III.22)}$$

and ζ is the cell fraction, calculated through the level set function χ based on the interface location.

$$\zeta = \frac{|\chi_i|}{|\chi_i| + |\chi_{i+1}|} \tag{III.23}$$

In our case, we have neither a jump for C nor for its flux βC_x, which translates into $a_{\partial P} = 0$ and $b_{\partial P} = 0$, so (III.21) simplifies to:

$$\left(\beta C_x\right)_x = \frac{1}{\Delta x}\left[\hat{\beta}\left(\frac{C_{i+1} - C_i}{\Delta x}\right) - \beta^-\left(\frac{C_i - C_{i-1}}{\Delta x}\right)\right] \tag{III.24}$$

Extension to three dimensions

The discretization of the diffusive term $\nabla \cdot (\beta \nabla C)$ in the vicinity of an interface ∂P in 3D is a bit trickier as jump conditions exist only for C and its normal flux $[\beta C_n]_{\partial P} = 0$, but nothing is specified about the tangential flux across ∂P. Liu et al. [2000] suggested a dimension by dimension application of the 1D discretization method that we adopt here. However, Liu et al. [2000] also emphasized that a simple projection of the normal flux jump condition on the cartesian coordinate axis leads to the right jump condition in the normal direction but also imposes an artificial and essentially physically wrong additional condition on the tangential flux across ∂P of the form $[\beta C_t]_{\partial P} = 0$, while the right physical condition is simply $[C_t]_{\partial P} = 0$.

Since our solid obstacles are all spheres, we follow the approach suggested by Shao et al. [2012] that involves changing coordinates from cartesian to spherical and writing the jump conditions in cartesian coordinates as a function of the jump conditions in spherical coordinates in a way that the right jump conditions are imposed.

Cartesian and spherical coordinate systems are related to each other through:

$$x = r\sin(\theta)\cos(\varphi) \tag{III.25}$$
$$y = r\sin(\theta)\sin(\varphi) \tag{III.26}$$
$$z = r\cos(\theta) \tag{III.27}$$

with $\theta \in [0, 2\pi]$ and $\varphi \in [-\pi/2, +\pi/2]$. The gradient of C in the cartesian coordinate system is related to the gradient of C in the spherical coordinate system through:

$$C_x = C_r\sin(\theta)\cos(\varphi) + C_{t_\theta}\cos(\theta)\cos(\varphi) - C_{t_\varphi}\sin(\varphi) \tag{III.28}$$
$$C_y = C_r\sin(\theta)\sin(\varphi) + C_{t_\theta}\cos(\theta)\sin(\varphi) + C_{t_\varphi}\cos(\theta) \tag{III.29}$$
$$C_z = C_r\cos(\varphi) - C_{t_\varphi}\sin(\varphi) \tag{III.30}$$

where t_θ is the unit tangential vector in the θ direction and t_φ is the unit tangential vector in the φ direction. Obviously on a sphere surface we have $C_r = C_n$. Multiplying the above equations by β we can write the jump conditions in the cartesian directions x, y and z as a function of the jump conditions in the normal

and tangential directions as:

$$[\beta C_x]_{\partial P} = [\beta C_n]_{\partial P}\sin(\theta)\cos(\varphi) + [\beta C_{t_\theta}]_{\partial P}\cos(\theta)\cos(\varphi)$$
$$- [\beta C_{t_\varphi}]_{\partial P}\sin(\theta) \tag{III.31}$$

$$[\beta C_y]_{\partial P} = [\beta C_n]_{\partial P}\sin(\theta)\sin(\varphi) + [\beta C_{t_\theta}]_{\partial P}\cos(\theta)\sin(\varphi)$$
$$+ [\beta C_{t_\varphi}]_{\partial P}\cos(\theta) \tag{III.32}$$

$$[\beta C_z]_{\partial P} = [\beta C_n]_{\partial P}\cos(\varphi) - [\beta C_{t_\theta}]_{\partial P}\sin(\varphi) \tag{III.33}$$

In our problem, we have $[C]_{\partial P} = 0$, $[\beta C_n]_{\partial P} = 0$, $[C_{t_\theta}] = 0$ and $[C_{t_\varphi}] = 0$. However, $[\beta C_{t_\theta}]_{\partial P} = [\beta]_{\partial P}C_{t_\theta}$ and $[\beta C_{t_\varphi}]_{\partial P} = [\beta]_{\partial P}C_{t_\varphi}$ are non zero because $[\beta]_{\partial P} \neq 0$, i.e., the diffusion coefficient β is discontinuous across the interface ∂P. To calculate these 2 terms, we need to calculate the tangential derivatives C_{t_θ} and C_{t_φ} at the particle surface. At the discrete level, these 2 tangential derivatives are approximated for each point on the particle surface using a central difference scheme that involves the values of C at two adjacent points. As C is not known at the time level t^{n+1}, we use C from the previous time level, i.e., t^n, to compute C_{t_θ} and C_{t_φ} as suggested by Shao et al. [2012]. Eventually, the 3 jump conditions (III.31)-(III.33) are added to the right hand side of the conservation equation as in a 1D case.

4 Validations

We verify here our implementation of the SIM and assess its capability to resolve the different flow problems we are interested in. We perform a step by step validation of the computed solution in problems of growing complexity. For diffusion and diffusion-reaction problems, we compare our SIM results to existing analytical solutions. For convection-diffusion problems, we compare our SIM results to existing correlations. Finally, for convection-diffusion-reaction problems, there does not exist any correlation or analytical solution, to the best of our knowledge. For this reason, we compare our SIM results to results computed with a boundary-fitted method with local mesh refinement that fully resolves the gradients at the particle interface. We test the limitations of SIM for a wide range of dimensionless numbers. In all the cases examined from now on, we are interested in the steady state solution only. However, the steady state solution is computed by our transient algorithm as the solution obtained when time derivatives are negligibly small. All transient computations are run with $\Delta t = 10^{-3}$.

4.1 Pure diffusion in a finite domain

Steady state diffusion from a single particle

The first validation test is performed in a purely diffusive regime. A spherical particle of radius r_p^* is placed at the center of a cubic domain $\Omega = L_x^* \times L_y^* \times L_z^*$ and a zero concentration $C_s = 0$ is imposed at the particle boundary and inside the particle. This condition is enforced through an infinitely fast reaction $\phi^2 \to \infty$ and a large diffusion coefficient ratio γ that makes the problem mass transfer controlled. A fixed concentration C_∞ is imposed at the boundary $\partial\Omega$ of the domain so that the concentration difference (or driving force) is constant. When the problem is posed
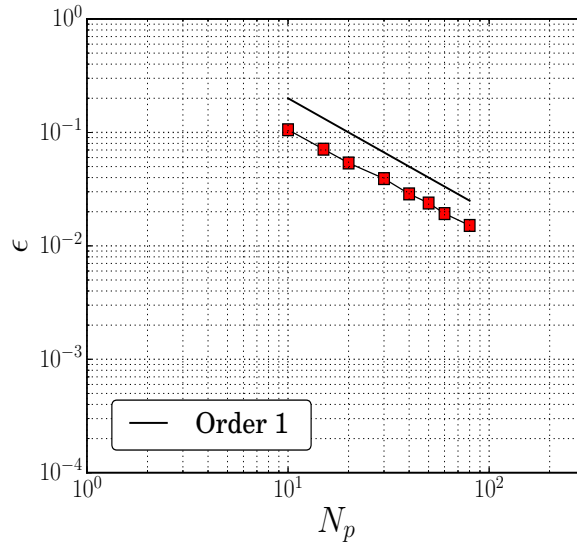
Figure III.1: Steady state diffusion from a single particle in a finite domain $L_x = L_y = L_z = 10$: spatial convergence of the error on the Sherwood number computed with SIM compared to the analytical solution.

in a spherical domain Ω of finite radius r_∞^*, we can solve the 1D problem and derive an expression for the Sherwood number (see Appendix 7 for the details) as follows:

$$Sh = \frac{k^* d_p^*}{D_f^*} = \frac{2r_\infty^*}{r_\infty^* - r_p^*} \tag{III.34}$$

where k^* denotes the mass transfer coefficient defined as:

$$k^* = \frac{D_f^*}{4\pi r_p^{*2}(C_\infty - C_s)} \int_{-\pi/2}^{\pi/2} \int_0^{2\pi} \frac{\partial C(r^*)}{\partial r^*}\bigg|_{r^*=r_p^*} r_p^{*2} sin(\theta) d\varphi d\theta \tag{III.35}$$

We set the dimensionless box size to $L_x = L_y = L_z = 10$. The particle dimensionless radius is $r_p = 0.5$. The analytical value of the Sherwood number in a spherical domain of finite radius $r_\infty = 5$ is $Sh_{an} = 20/9 = 2.22$. We assume that this solution is a good approximation of the solution posed in a cubic domain $L_x = L_y = L_z = 2r_\infty$. We examine the convergence of the method by computing Sh as a function of the grid size $\Delta x = 1/N_p$. We then compute the relative error with respect to Sh_{an} as $\epsilon = \frac{Sh(N_p) - Sh_{an}}{Sh_{an}}$ and plot the convergence of ϵ with N_p in FIG. III.1. The solution follows an expected first order spatial convergence. In this test, the error originates from two contributions. The first contribution is related to the spatial discretization of the problem and the contribution we are interested in. The second contribution is due to the fact that the analytical solution is derived in a spherical domain and compared to the computed solution in a cubic box. For the range of N_p considered, it is clear in FIG. III.1 that the second contribution is negligible and that provided $r_\infty = L_x/2$ is chosen large enough, the analytical solution in a spherical domain does not differ much from the solution in a cubic domain.

Steady state diffusion from a single particle in a gradient of concentration

We test our SIM in another diffusive configuration previously examined by Shao et al. [2012]. A solid particle of diffusion coefficient D_s^* is immersed at the center of a cubic domain $\Omega = L_x^* \times L_y^* \times L_z^*$ of fluid at rest of diffusion coefficient D_f^*. Dirichlet boundary conditions $C = C_1 = 1$ at the top wall and $C = C_2 = 0$ at the bottom wall are imposed to generate a concentration gradient in the z direction. Zero normal flux boundary conditions are imposed on the 4 lateral walls. The average Sherwood number corresponding to the flux through a horizontal xy plane is defined as:

$$Sh = \frac{L_z^*}{C_2 - C_1} \cdot \frac{1}{L_x^* L_y^*} \int_0^{L_x^*} \int_0^{L_y^*} \left(\frac{\partial C}{\partial z^*} \right) dy^* dx^* \tag{III.36}$$

The average Sherwood number can be analytically predicted based on the analogy with Maxwell-Garnett electric conductivity [Maxwell et al., 2005] as:

$$Sh = 1 + \frac{3\alpha(\gamma - 1)}{\gamma + 2} \tag{III.37}$$

where α is the solid volume fraction. Following Shao et al. [2012], we simulate two cases with two different solid volume fractions. We keep the dimensional box size constant to $L_x^* = L_y^* = L_z^* = 10mm$ and vary the solid volume fraction α through selecting 2 different particle radii $r_p^* = 1.25mm$ and $r_p^* = 2mm$, i.e., $r_p^*/L_x^* = 0.125$ and $r_p^*/L_x^* = 0.2$, respectively. We select the diffusion ratio γ to span the interval $[10^{-2}, 10^2]$. For each value of γ we compute the average Sherwood number and compare its value to the theoretical prediction and the numerical results of Shao et al. [2012]. FIG. III.2 exhibits a very satisfactory agreement of our results with both the analytical prediction and numerical results of Shao et al. [2012]. We compute an additional case for $r_p^* = 1.5mm$, i.e., $r_p^*/L_x^* = 0.15$, and plot the convergence towards the analytical solution in FIG. III.3 for the three solid volume fractions corresponding to $r_p^*/L_x^* = 0.1, 0.15, 0.2$. As expected, a first order spatial convergence is obtained. The error is shown to increase with the increase of α. The concentration contours in a xz vertical cut plane containing the sphere center are illustrated in FIG. III.4 for the case of $r_p^*/L_x^* = 0.2$ and $\gamma = 0.1$.

4.2 Steady state internal diffusion and chemical reaction in a single particle

We consider a spherical porous catalyst particle of diameter d_p^* and diffusion coefficient D_s^* immersed at the center of a cubic domain $\Omega = L_x^* \times L_y^* \times L_z^*$. The particle is assumed to undergo a first order chemical reaction controlled by a constant k_s^* such that the chemical species concentration C inside the particle satisfies (III.5). If the surface concentration denoted C_s is known and assumed to be constant over the sphere surface, the problem becomes 1D in space and we can easily write the steady state solution of (III.5) as follows:

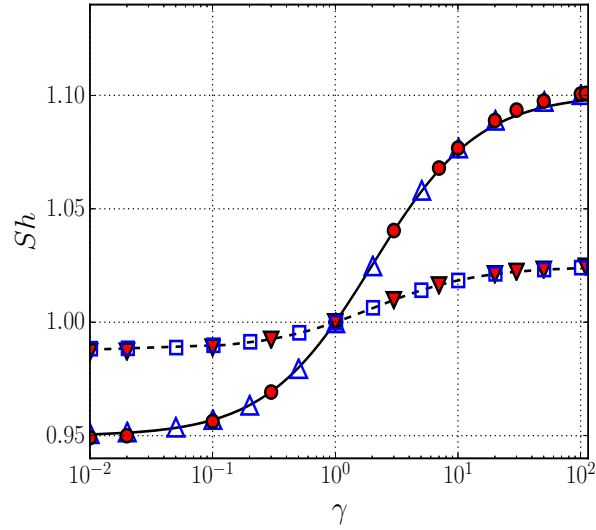$$C(r) = C_s \frac{\sinh(\phi r)}{2r \sinh(\phi/2)} \tag{III.38}$$

Figure III.2: Steady state diffusion from a single particle in a gradient of concentration: comparison of average Sherwood number computed with SIM to the analytical solution and to the previous study of Shao et al. [2012]. Case 1, $r_p^*/L_x^* = 0.2$: continuous black line corresponds to the analytical solution, open triangles correspond to the results of Shao et al. [2012], and disks correspond to our simulation results. Case 2, $r_p^*/L_x^* = 0.125$: dashed black line corresponds to the analytical solution, open squares correspond to the results of Shao et al. [2012] and triangles correspond to our simulation results.
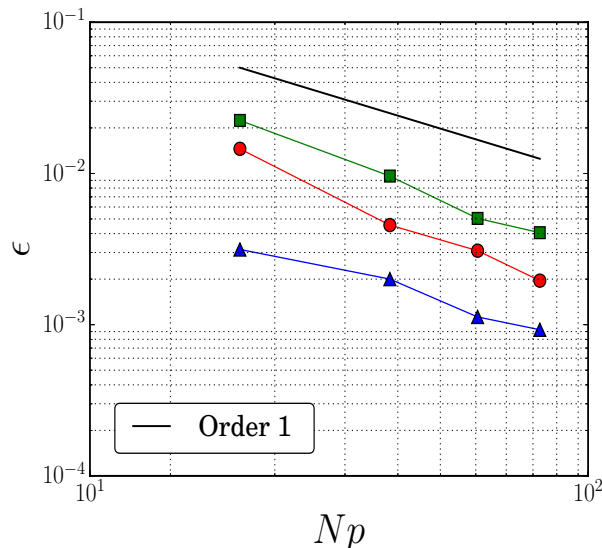
Figure III.3: Steady state diffusion from a single particle in a gradient of concentration: spatial convergence of the relative error on the average Sherwood number computed with SIM. Triangles correspond to $r_p^*/L_x^* = 0.1$, disks correspond to $r_p^*/L_x^* = 0.125$, and squares correspond $r_p^*/L_x^* = 0.2$.
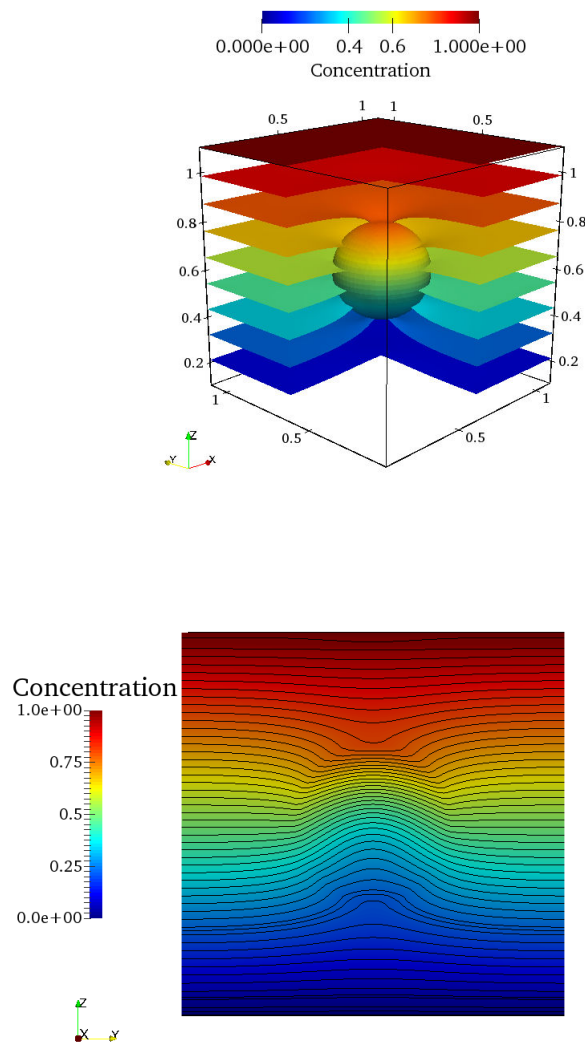
Figure III.4: Steady state diffusion from a single particle in a gradient of concentration: concentration iso-countours for $r_p^*/L_x^* = 0.2$ and $\gamma = 0.1$ in a 3D view (left) and in a xz vertical cut plane containing the sphere center (right).

where as usual $r = r^*/d_p^*$ is the dimensionless radial position and $\phi = d_p^*\sqrt{\dfrac{k_s^*}{D_s^*}}$ is the Thiele modulus. The derivation of (III.38) can be found in many textbooks.

Dirichlet boundary conditions $C = 1$ are imposed on the 6 walls of the cubic domain. We impose $C_s = 1$ through an infinitely large diffusion coefficient D_f^* in fluid phase, i.e., γ is chosen asymptotically small. The domain size does not matter here and only needs to be chosen dimensionlessly larger than 1. We compare our SIM concentration profile inside the particle to the analytical solution (III.38) in FIG. III.5 for $N_p = 20$. The agreement is once again very satisfactory. The numerical method is capable of capturing the steep concentration gradients at the particle surface even for a modest resolution. The corresponding concentration iso-countours are shown in FIG. III.6 for $N_p = 80$.

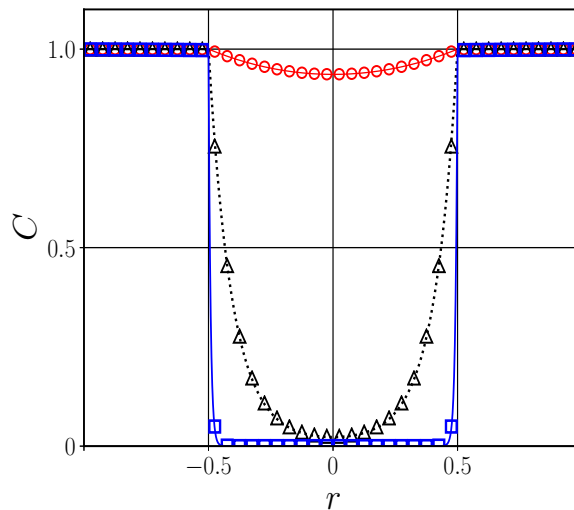**Figure III.5:** Internal diffusion and chemical reaction in a single particle: comparison of concentration profiles computed with SIM to analytical profiles for different Thiele moduli. Lines correspond to analytical solutions and markers correspond to our simulation results. Red line and red circles for $\phi^2 = 1.6$. Black doted line and open triangles for $\phi^2 = 160$. Blue line and open squares for $\phi^2 = 16000$.
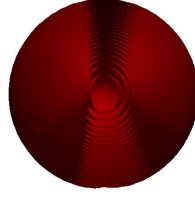
(a) $\phi^2 = 1.6$
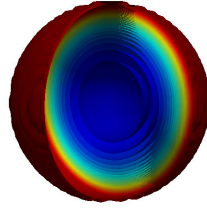
(b) $\phi^2 = 160$
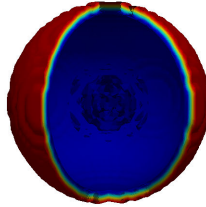
(c) $\phi^2 = 16000$

Figure III.6: Internal diffusion and chemical reaction in a single particle: concentration iso-surfaces inside the particle for different reaction rates.

Based on the concentration profile, the effectiveness factor η for a catalyst particle can be defined as the ratio of the overall internal reaction rate in the particle to the reaction rate that can be attained in the absence of diffusion limitations. For a spherical catalyst particle with a fixed surface concentration C_s, we have:

$$\eta = \frac{\int_0^{2\pi} \int_{-\pi/2}^{+\pi/2} \int_0^{r_p^*} -k_s^* C(r^*) sin(\theta) r^{*2} d\varphi d\theta dr^*}{-k_s^* \frac{4\pi}{3} r_p^{*3} C_s}$$

$$= \frac{\overline{C_v}}{C_s} = \frac{6}{\phi}\left(\frac{1}{tanh(\phi/2)} - \frac{2}{\phi}\right)$$

(III.39)

where $C(r^*) = C_s \dfrac{r_p^* \sinh(\phi r^*)}{r^* \sinh(\phi r_p^*)}$ is the Thiele concentration profile given by (III.38) in a dimensional form for a given surface concentration C_s and $\overline{C_v}$ is the average volume concentration in the particle.

Depending on reaction kinetics and assuming, e.g., $\gamma \in [10^{-2}, 10^2]$, i.e., γ is not asymptotically small/large, the effectiveness factor η exhibits two asymptotic limits. When the reaction rate is very low compared to diffusion, $\phi \ll 1$, the system is controlled by kinetics and the catalyst surface concentration C_s is equal to fluid concentration, and so $\eta \to 1$. When the reaction rate is high compared to diffusion, i.e. $\phi \gg 1$, the system is limited by diffusion and the surface concentration C_s approaches zero, therefore $\eta \to 6/\phi$.

In the following test, we once again impose $C_s = 1$ through an asymptotically small γ. We vary the Thiele modulus ϕ in the range $[0.2, 120]$ by varying the reaction rate constant k_s^*. For each value of ϕ, we calculate numerically the effectiveness factor η and examine the spatial convergence of the solution computed with our SIM and a standard VOF method. Hence we compute SIM solutions for $N_p = 10, 40, 80$ and VOF solutions for $N_p = 40, 80$. FIG. III.7 shows η as a function of ϕ for $N_p = 10, 80$ with SIM and $N_p = 40$ with VOF. Results obtained with SIM and VOF are further compared to each other and to the analytical solution in FIG. III.8 and FIG. III.9 for various values of ϕ and N_p. We can make the 3 following comments: (ii) both methods show a first order spatial convergence, (ii) VOF with a grid size 4 times smaller than SIM gives approximately the same computed solution, and (iii) when $N_p = 80$, SIM predictions are very close to the analytical solution with a slightly growing deviation for $\phi > 20$. The superior accuracy of the solution computed with SIM compared to that computed with VOF is further emphasized in FIG. III.8 where we plot the error to the analytical solution as a function of ϕ for $N_p = 80$. Finally, FIG. III.9 also highlights that fact that the magnitude of the error increases with increasing ϕ in relation to the concentration gradients becoming steeper in the vicinity of the particle surface as ϕ increases, i.e., the internal mass boundary layer gets thinner as ϕ increases.

4.3 Steady state convection-diffusion in the flow past a single sphere: external mass transfer problem

We now validate our SIM in the case of external mass transfer in the flow past a spherical solid particle in an unbounded domain. A spherical particle is placed in a box of size $L_x \times L_y \times L_z = 5 \times 5 \times 15$. The fluid enters the flow domain on the left boundary with an imposed fluid velocity $\mathbf{u} = (0, 0, 1)$ and a concentration $C = C_\infty = 1$. The particle is centered in the x and y directions. Periodic boundary conditions are imposed in x and y directions while a classical outflow boundary condition $\frac{\partial \mathbf{u}}{\partial z} = \frac{\partial C}{\partial z} = 0$ and $p = p_{ref} = 0$ is imposed at the outlet boundary. FIG. III.10 illustrates the flow configuration in a xz cut plane containing the sphere center. The concentration C in the particle is imposed to 0 by selecting an extremely large value of ϕ. The problem is hence controlled by Sc and Re.

To illustrate that our SIM predicts the right external mass transfer, we set
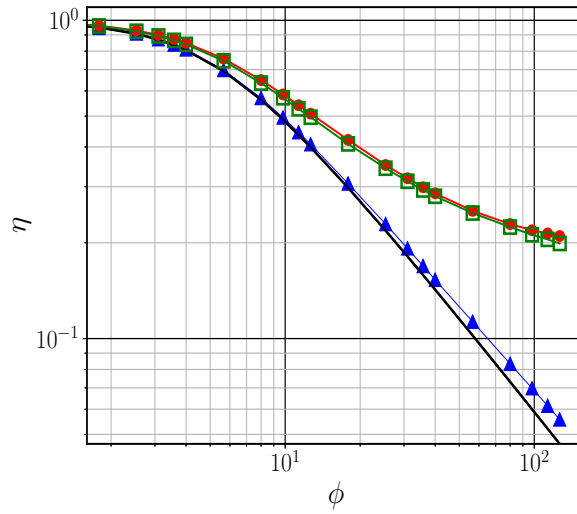
Figure III.7: Internal diffusion and chemical reaction in a single particle: comparison of effectiveness factor computed with VOF and SIM as a function of ϕ. Red color corresponds to VOF obtained with $N_p = 40$ and green color corresponds to SIM obtained with $N_p = 10$. Blue color corresponds to SIM with $N_p = 80$ and black line corresponds to the analytical solution.
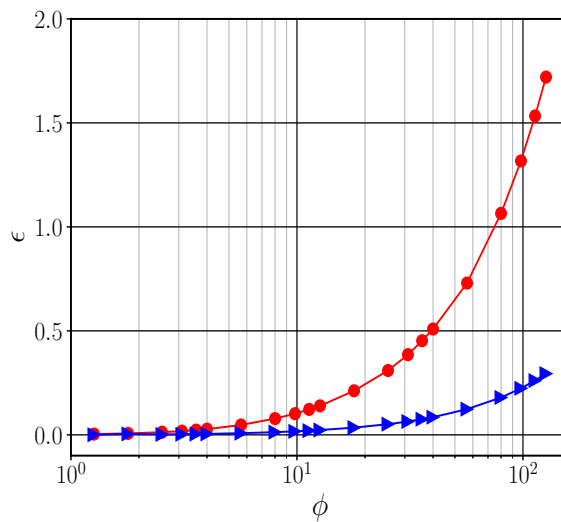
Figure III.8: Internal diffusion and chemical reaction in a single particle: relative error on the effectiveness factor as a function of ϕ for $N_p = 80$. Red color corresponds to VOF and blue color corresponds to SIM.
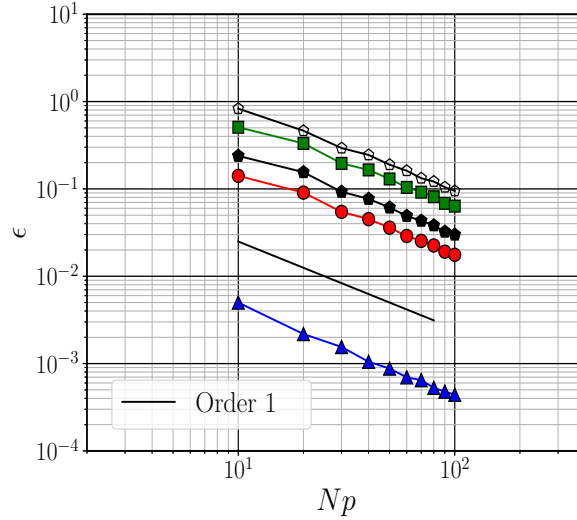
Figure III.9: Internal diffusion and chemical reaction in a single particle: spatial convergence of relative error on effectiveness factor computed with SIM and VOF for various Thiele moduli: $\phi = 1.2$, blue triangles with SIM, $\phi = 12$, red disks with SIM, $\phi = 20$, black filled pentagons with SIM, black open pentagons with VOF, $\phi = 120$, green squares with SIM.
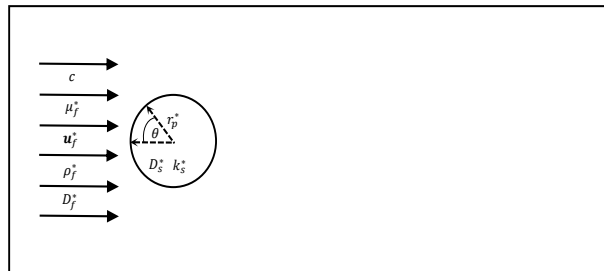
Figure III.10: Geometric configuration for the problem of steady state convection-diffusion in the flow past a single sphere with or without reaction inside the particle: view in a xz cut plane containing the sphere center (Simulation domain is $5d_p^* \times 5d_p^* \times 15d_p^*$).
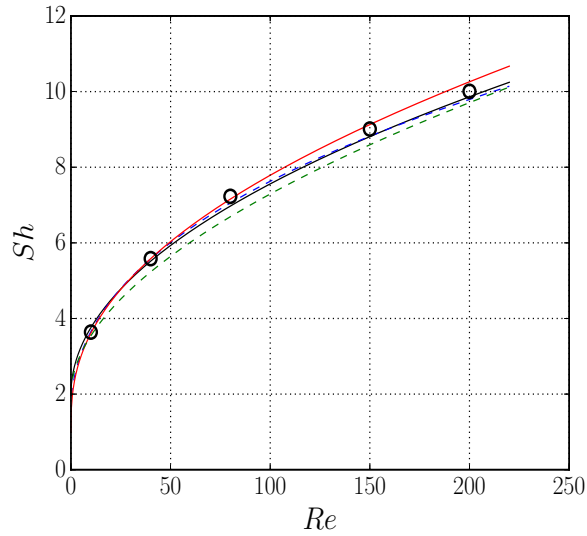
Figure III.11: Steady state convection-diffusion in the flow past a single sphere: comparison of computed Sherwood number with literature correlations at $Sc = 1$. Our SIM results are represented by circles while correlations are as follows: red line for Feng and Michaelides [2000], black line for Ranz et al. [1952], green-doted line for Whitaker [1972] and blue-dashed line for Clift et al. [2005].

$Sc = 1$ and vary Re in the range $[0, 200]$. We compute the steady state Sherwood number Sh for $N_p = 80$ and compare its value to literature correlations as, e.g., the correlation of Feng and Michaelides [2000], in FIG. III.11. Overall, we observe a very satisfactory agreement between our SIM results and literature correlations.

4.4 Steady state convection-diffusion in the flow past a single reactive sphere: external-internal mass transfer

We now consider a similar problem to the one in *Section 4.3* but with a first order reaction inside the particle. To validate our SIM, we compare the results computed with our SIM to results supplied by a highly accurate boundary fitted method implemented in the JADIM code. JADIM solves the same system of equations (III.9)-(III.12) but with a different discretization scheme in space and in time. The high accuracy of solutions computed with JADIM derives both from its boundary fitted spatial discretization scheme and the ability to locally refine the mesh in both the internal and external mass boundary layers.

The numerical methods used in JADIM have been thoroughly described by Magnaudet et al. [1995] and Calmet and Magnaudet [1997]. Consequently they are only quickly summarized here. The JADIM code solves the incompressible Navier-Stokes equations and the concentration equation in general orthogonal curvilinear coordinates which are boundary fitted to the particle surface. Equations are integrated in space using a finite volume method in which advective and diffusive terms are evaluated with second-order accurate centered schemes. The solution is advanced in time by means of a three-step Runge-Kutta time-stepping procedure in which advective terms are computed explicitly while diffusive terms are treated by a semi-implicit
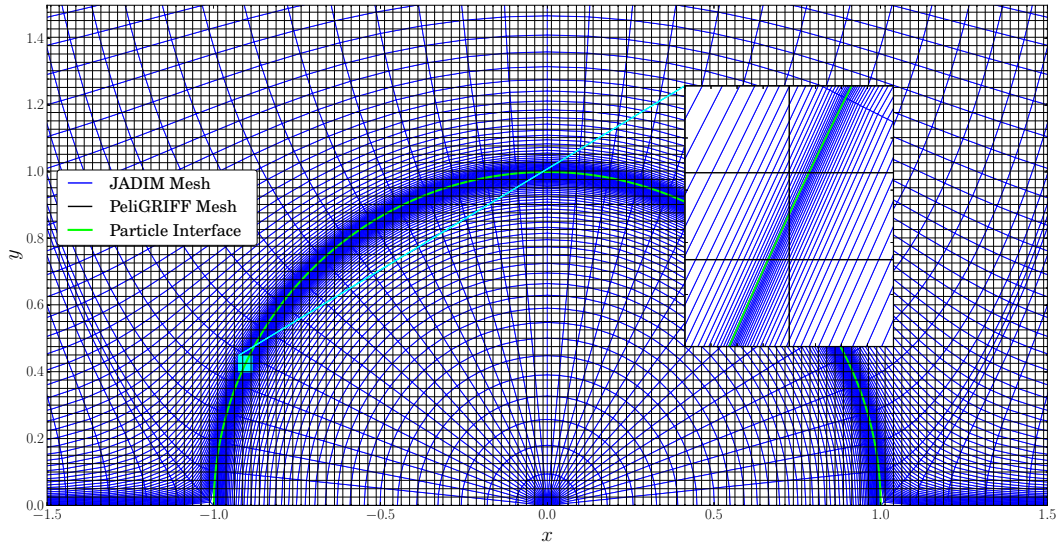
Figure III.12: Comparison of the finest meshes used by JADIM (boundary fitted) and SIM (cartesian grid).

Crank-Nicholson scheme. Incompressibility is satisfied after the third intermediate time step by solving a Poisson equation for an auxiliary potential from which the true pressure is deduced, similarly to (III.13)-(III.15). The complete algorithm is second order accurate in both space and time.

The mesh grid used in the present work is sketched in Fig. III.12. The orthogonal axisymmetric mapping is obtained by using the streamlines and the equipotential lines of the potential flow around a circular cylinder. The mesh is stretched in order to have at least four points in the external mass boundary layer that scales as $Pe^{-1/3}$. Simulations are performed in a 2D axisymmetric configuration which reproduces the geometry of a spherical particle. The fluid computational domain is limited by the particle surface and by external boundaries on which inflow, free stream, axial symmetry, and outflow boundary conditions are imposed. The equations are solved inside the particle over a polar mesh adjusted to the fluid mesh at the particle surface. The internal mass boundary layer thickness reduces when the kinetics of the chemical reaction, i.e., ϕ, increases. The mesh inside the particle is thus refined close to the particle surface following the scaling of the boundary layer as ϕ^{-1}. At least four grid points stand within the internal boundary layer in order to compute properly the internal concentration gradient at the particle surface. A particle of radius r_p^* is placed in a domain with a spatial extension of at least $r_\infty^* = 100 r_p^*$, so that the assumption of infinite domain is physically valid.

All simulations are performed with $N_p = 80$ unless spatial convergence is investigated. The used DLM-FD simulation domain is $5 \times 5 \times 15$. We set $\gamma = 10$, $\phi = 2$ and $Sc = 1$ and vary Re in the range $[0, 200]$. Our SIM results plotted in Fig. III.13 agree well with the JADIM results and the model for the mean surface concentration $\overline{C_s}$ suggested in Sulaiman et al. [2018a]. Fig. III.13 shows that the mean surface concentration $\overline{C_s}$ increases with the increase of Re. Then we

set $\gamma = 10$, $\phi = 150$ and $Sc = 1$ and vary ϕ in the range $[0, 40]$. Once again a good agreement between our SIM results, the JADIM results and the model for the mean surface concentration $\overline{C_s}$ suggested in Sulaiman et al. [2018a] is highlighted in Fig. III.14, with a small deviation of our SIM results from the JADIM results and the model predictions that grows as ϕ increases due to the internal boundary layer getting thinner as $1/\phi$.

We now compare concentration profiles computed with our SIM and JADIM. We set $\gamma = 10$, $Re = 10$, and $Sc = 1$, select two Thiele moduli $\phi = 4$ and $\phi = 10$ and plot the concentration profile obtained with each method in Fig. III.15. The agreement is visually very good. The actual error between SIM and JADIM (not shown here for the sake of conciseness) increases for $\phi = 10$ compared to $\phi = 4$, in line with what we observe for $\overline{C_s}$. We run another set of simulations with $\gamma = 10$, $\phi = 10$, $Sc = 1$ and two Reynolds numbers $Re = 10$ and $Re = 100$. Concentration profiles plotted in Fig. III.16 once again in a cross-section normal to the inlet flow, corresponding to $\theta = 90$. They highlight a satisfactory agreement between our SIM results and the JADIM results. The error between SIM and JADIM (not shown here for the sake of conciseness) only mildly increases with Re. The numerical accuracy is consequently mostly controlled by the internal mass boundary layer thickness.

Finally, we examine the spatial convergence of the SIM computed solution to the JADIM reference solution. We set $\gamma = 0.1$, $\phi^2 = 40$ and $Re = 150$, select $Sc = 0.1$, $Sc = 1$ and $Sc = 10$ and N_p in the range $[10, 80]$. We then compute and plot the error ϵ on the mean surface concentration $\overline{C_s}$ between SIM and JADIM. Fig. III.17 shows that ϵ increases slightly only with the increase of Sc. This behavior is similar to the behavior of the solution with increasing Re at constant ϕ, that shows that ϵ is mainly controlled by the reaction rate and the internal mass boundary layer thickness. To investigate the effect of the reaction rate on the solution, we perform a final set of simulations with $\gamma = 0.1$, $Sc = 10$, $Re = 150$ and ϕ^2 varying in the range $[40, 4000]$. Fig. III.18 reveals that ϵ increases significantly with the increase of ϕ^2. For $\phi^2 = 40$, even a mesh resolution $N_p = 20$ is sufficient to supply a computed solution with a relative error of 3%. At $\phi^2 = 200$, a grid resolution $N_p = 60$ is needed to reach the same accuracy. For $\phi^2 = 400$, a grid resolution with more than $N_p = 80$ is needed to reach an accuracy corresponding to a relative error of less than 4%. And finally at $\phi^2 = 4000$, even the finest grid resolution considered here $N_p = 80$ supplies a computed solution that is still 11% off from the reference solution.

5   Interacting Spheres

We examine here the external forced convection-diffusion on a sequence of interacting spheres undergoing an internal first order irreversible chemical reaction. The non-reactive problem without diffusion inside solid bodies was firstly introduced by [Ramachandran et al., 1989] for heat transfer. As in *Section 4*, we are interested in the steady state solution only and all transient computations leading to steady state are run with $\Delta t = 10^{-3}$. Ramachandran et al. [1989] suggested empirical

Figure III.13: Steady state convection-diffusion in the flow past a single reactive sphere: comparison of the mean surface concentration $\overline{C_s}$ at $\phi = 2$, $\gamma = 10$ and $Sc = 1$ as a function of Re, computed with SIM (red squares), computed with JADIM (black disks), and predicted by the model of Sulaiman et al. [2018a] (black line).
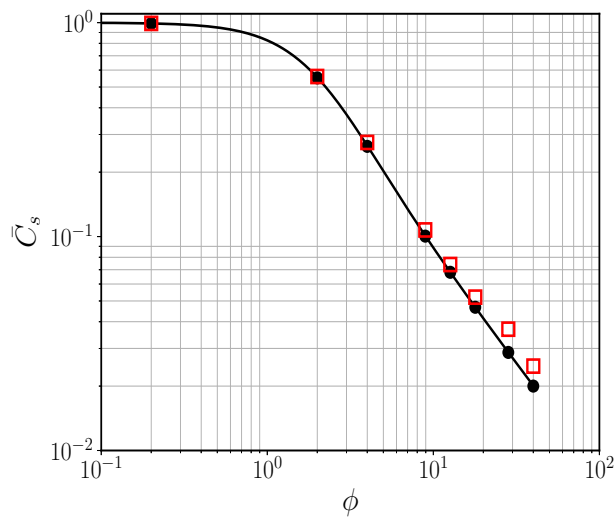
Figure III.14: Steady state convection-diffusion in the flow past a single reactive sphere: comparison of mean surface concentration $\overline{C_s}$ at $Re = 150$, $\gamma = 10$ and $Sc = 1$ as a function of ϕ, computed with SIM (red squares), computed with JADIM (black disks), and predicted by the model of Sulaiman et al. [2018a] (black line).
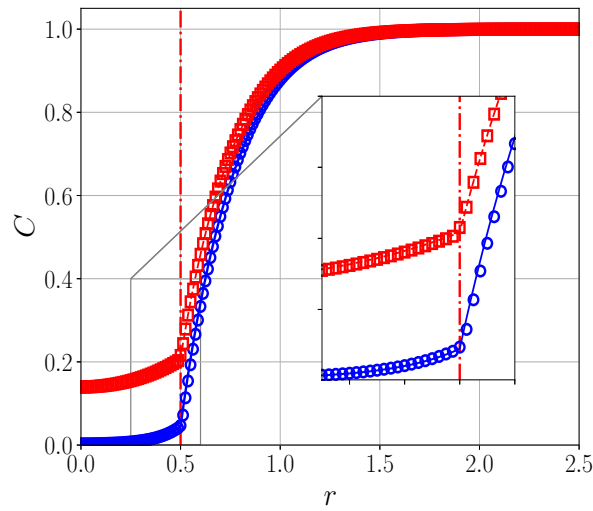
Figure III.15: Steady state convection-diffusion in the flow past a single reactive sphere: comparison of concentration profile in the direction normal to the flow ($\theta = 90$), at $Re = 10$, $\gamma = 10$ and $Sc = 1$ for two Thiele moduli: $\phi = 4$, red color, and $\phi = 10$, blue color. Continuous line correspond to JADIM and markers correspond to SIM.

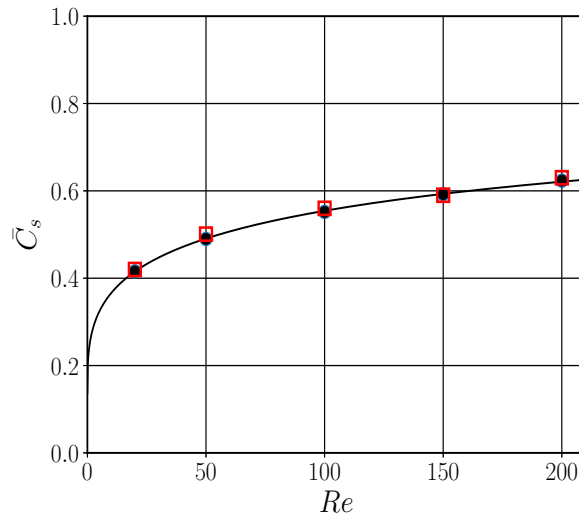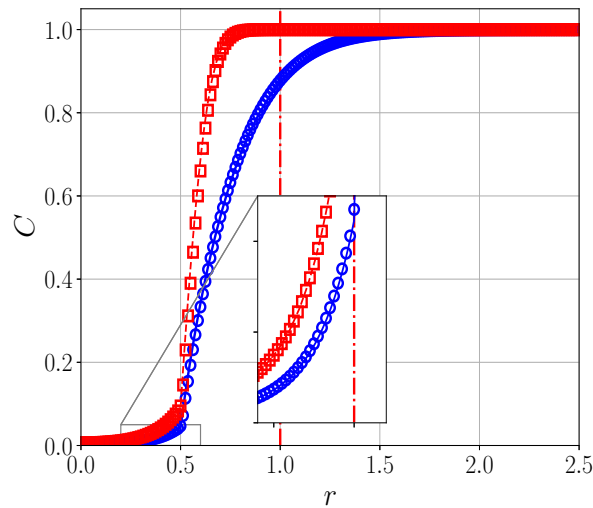**Figure III.16:** Steady state convection-diffusion in the flow past a single reactive sphere: comparison of concentration profile in the direction normal to the flow ($\theta = 90$), for $\phi = 4$, $\gamma = 10$ and $Sc = 1$ and two Reynolds numbers: $Re = 100$, red color, and $Re = 10$, blue color. Continuous lines correspond to JADIM and markers correspond to SIM.

Figure III.17: Steady state convection-diffusion in the flow past a single reactive sphere: spatial convergence of relative error on mean surface concentration $\overline{C_s}$ computed with SIM at $Re = 150$, $\phi^2 = 40$, and $\gamma = 0.1$ for $Sc = 0.1$, red disks, $Sc = 1$, black triangles, and $Sc = 10$, black open circles.

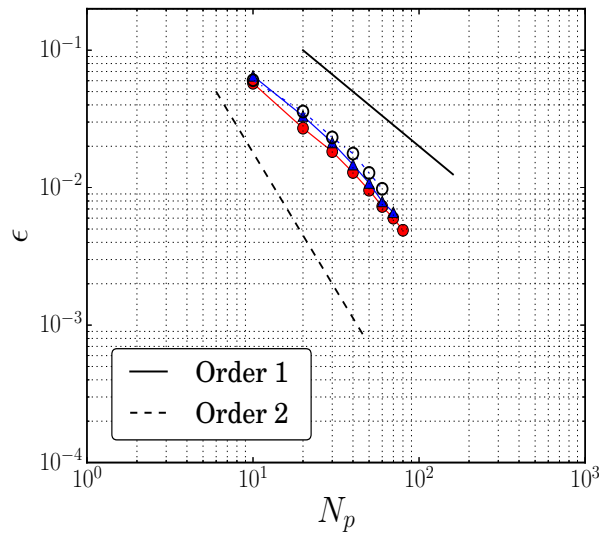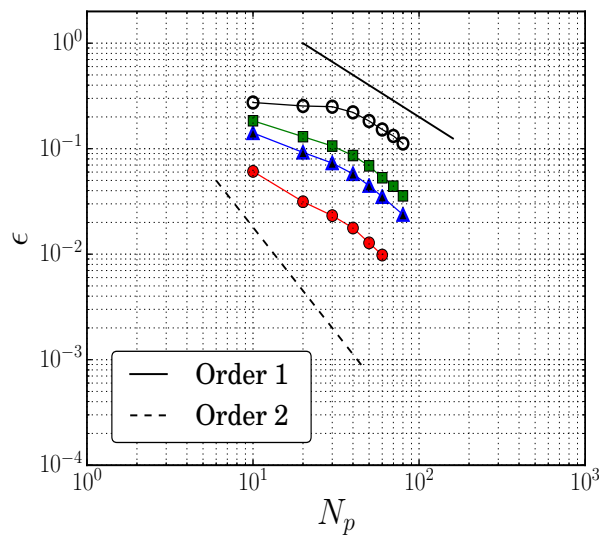**Figure III.18:** Steady state convection-diffusion in the flow past a single reactive sphere: spatial convergence of relative error on mean surface concentration $\overline{C_s}$ computed with SIM at $Re = 150$, $Sc = 10$, and $\gamma = 0.1$ for $\phi^2 = 40$, red disks, $\phi^2 = 200$, blue triangles, $\phi^2 = 400$, green squares, and $\phi^2 = 4000$, black open circles.
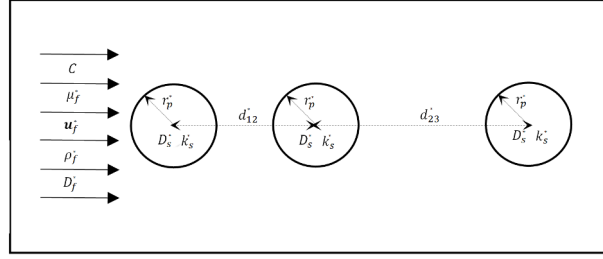
Figure III.19: Geometric configuration for the problem of steady state convection-diffusion in the flow past 3 aligned reactive spheres: view in a xz cut plane containing the sphere center (Simulation domain is $5d_p^* \times 5d_p^* \times 15d_p^*$).

corrective terms to relate the non-reactive Sherwood number of a single sphere to the non-reactive Sherwood numbers of interacting spheres. The corrective terms account for separation distances effect between the particles. The aim of this work is to include the effect of a chemical reaction inside the solid bodies and to introduce, based on internal-external coupling, a model for the reactive Sherwood number for each particle, that accounts for the effects of diffusion, convection, and reaction. We aim at extending the model we suggested for a single sphere in [Sulaiman et al., 2018a] to more concentrated particle-laden flows and consider the flow configuration investigated here as a proper toy model for mass transfer with reaction in dilute particle-laden flows. The core aspect of our model is that it is possible to construct a reactive Sherwood number formula based on an existing non-reactive Sherwood number formula. We show thereafter that this approach is still valid in dilute particle-laden systems experiencing hydrodynamic interactions.

5.1 Problem definition

We consider a system composed of three aligned spherical catalyst particles along z in a box of size $L_x \times L_y \times L_z = 5 \times 5 \times 15$. The fluid enters the flow domain on the left boundary with an imposed fluid velocity $\mathbf{u} = (0, 0, 1)$ and concentration $C = 1$. The three particles are centered in the x and y directions. Periodic boundary conditions are imposed in x and y directions while a classical outflow boundary condition $\frac{\partial \mathbf{u}}{\partial z} = \frac{\partial C}{\partial z} = 0$ and $p = p_{ref} = 0$ is imposed at the outlet boundary. The separation distances between the first and second particles and between the second and third particles are d_{12} and d_{23}, respectively, as shown in FIG. III.19. The problem is controlled by the Reynolds number Re, the Schmidt number Sc, the diffusion coefficient ratio γ and the Damkohler ϕ^2. All computations are performed with $N_p = 70$.

We approach the problem through the external-internal coupling based on the continuity of C and of its normal flux at the fluid/solid interface ∂P. The normal flux density at the particle surface in the solid phase $N_{s,\partial P}^*$ is given by:

$$N_{s,\partial P}^* = -D_s^* \frac{dC}{dr^*} \bigg|_{r^*=r_p^*} \tag{III.40}$$

The concentration profile in the solid phase is given by (III.38). Calculating the radial derivative at $r^* = r_p^*$ (or $r = 0.5$), the flux in the solid phase can be written as:

$$N^*_{s,\partial P} = -\frac{D^*_s C_s}{d^*_p}\left(\frac{\phi}{tanh(\phi/2)} - 2\right) \tag{III.41}$$

The normal flux density at the particle surface in the fluid phase $N^*_{f,\partial P}$ can be written as:

$$N^*_{f,\partial P} = -k^*_f(C_s - C_\infty) \tag{III.42}$$

where k^*_f is the external mass transfer coefficient in the fluid phase, analytically unknown in case of external convection. The continuity of the normal flux at ∂P, i.e., $N^*_{s,\partial P} = N^*_{f,\partial P}$, leads to:

$$k^*_f(C_s - C_\infty) = D^*_s \frac{C_s}{d^*_p}\left(\frac{\phi}{tanh(\phi/2)} - 2\right) \tag{III.43}$$

And we can hence deduce the expression of the surface concentration C_s:

$$C_s = \frac{C_\infty}{1 + \frac{D^*_s}{d^*_p k^*_f}\left(\frac{\phi}{tanh(\phi/2)} - 2\right)} \tag{III.44}$$

In order to determine C_s, we need to evaluate the external mass transfer coefficient k^*_f. Here, we assume that the internal problem is only affecting the external problem through the concentration gradient. Thus, the external Sherwood number is assumed independent of the reaction rate. We hence evaluate the external mass transfer coefficient from the external Sherwood number Sh, i.e., a non-reactive Sherwood number, as $k^*_f = Sh\, D^*_f/d^*_p$. Then, any appropriate empirical correlation available in the literature for Sh can be used. For instance in [Sulaiman et al., 2018a], we used for a single sphere the correlation defined by Feng and Michaelides [2000]:

$$Sh = 0.922 + Re^{1/3}Sc^{1/3} + 0.1Re^{2/3}Sc^{1/3} \tag{III.45}$$

For a series of three interacting spheres, Ramachandran et al. [1989] suggested to account for the interactions between the spheres through corrective coefficients for the Sherwood number of each of the three spheres. These corrective coefficients, mainly empirical, are established based on computational data, and related to the correlation for a single sphere. The individual Sherwood number reads:

$$Sh_j = Sh \cdot \beta_j \quad j = 1, 2, 3 \tag{III.46}$$

where j is the sphere number and the β_j , $j = 1, 2, 3$ are the empirical corrective terms defined by Ramachandran et al. [1989] as:

$$\beta_1 = 0.9555 Sc^{0.0276} Re^{0.0108} d_{12}^{0.113/[1+1.5ln(10Pe)]} e^{-0.02113/d_{23}} \tag{III.47}$$

$$\beta_2 = 1 - 0.0697(1 + ln(Re))^{0.767}[1 + ln(10ReSc)]^{0.095} d_{23}^{-0.13} \\ - 4.807(1 + ln(Re))^{0.012} d_{12}^{-5.28} \tag{III.48}$$

$$\beta_3 = 1 - 0.532 Sc^{-0.019} Re^{0.032} e^{-0.0146/d_{12}}\left(\frac{1}{d_{23}}\right)^{3.044/[1+1.1ln(10Pe)]} \tag{III.49}$$

Part III. Three interacting spheres in a row : coupling mass transfer and chemical reaction

---

The average surface concentration $\overline{C_{s,j}}$ for sphere j with corresponding Sherwood number Sh_j, can be written as follows:

$$\overline{C_{s,j}} = \frac{C_\infty}{1 + \frac{2\gamma}{Sh_j}\left(\frac{\phi/2}{tanh(\phi/2)} - 1\right)} \qquad j = 1, 2, 3 \qquad \text{(III.50)}$$

The formulation of a 'reactive' Sherwood number that accounts for convection, diffusion and reaction is based on two concentration gradients instead of a single concentration gradient in the external non-reactive case. The first gradient is the external gradient involving $(\overline{C_s} - C_\infty)$ and the second gradient is the internal gradient involving $(\overline{C_v} - \overline{C_s})$, where $\overline{C_v}$ is the mean volume concentration of C in each sphere. To derive an expression for $\overline{C_v}$, we integrate the 1D concentration profile given by (III.38), assuming C_s is a function of the position on the sphere and the radial dependence is still reasonably valid, over the particle volume as

$$\overline{C_v} \simeq \frac{3}{4\pi r_p^{*3}} \int_0^{2\pi} \int_{-\pi/2}^{+\pi/2} \int_0^{r_p^*} C_s(\varphi, \theta) \frac{r_p^* \sinh(\phi r^*)}{r^* \sinh(\phi r_p^*)} sin(\theta) r^{*2} d\varphi d\theta dr^* \qquad \text{(III.51)}$$

and further approximate this integral as:

$$\overline{C_v} \simeq \frac{3\overline{C_s}}{4\pi r_p^{*3}} \int_0^{2\pi} \int_{-\pi/2}^{+\pi/2} \int_0^{r_p^*} \frac{r_p^* \sinh(\phi r^*)}{r^* \sinh(\phi r_p^*)} sin(\theta) r^{*2} d\varphi d\theta dr^*$$
$$= \frac{6\overline{C_s}}{\phi}\left(\frac{1}{tanh(\phi/2)} - \frac{2}{\phi}\right) \qquad \text{(III.52)}$$

$\overline{C_s}$ is estimated by model (III.50) and we eventually obtain an expression for the mean volume concentration $\overline{C_{v,j}}$ for sphere j that reads as follows:

$$\overline{C_{v,j}} = \frac{6C_\infty}{1 + \frac{2\gamma}{Sh_j}\left(\frac{\phi/2}{tanh(\phi/2)} - 1\right)}\left(\frac{1}{\phi tanh(\phi/2)} - \frac{2}{\phi^2}\right) \qquad j = 1, 2, 3 \qquad \text{(III.53)}$$

The conjugate mass transfer problem is formulated with the additivity rule. The additivity rule states that the overall resistance to mass transfer in the system is the sum of two resistances. The resistance is related to the inverse of the mass transfer coefficients. We hence define the 2 Sherwood numbers as:

internal Sherwood number Sh_{in}

$$Sh_{in} = \frac{N_{s,\partial P}^* \, d_p^*}{D_s^*(\overline{C_s} - \overline{C_v})} = \frac{k_{in}^* d_p^*}{D_s^*} \qquad \text{(III.54)}$$

where k_{in}^* is the internal mass transfer coefficient.
external Sherwood number Sh

$$Sh = \frac{N_{f,\partial P}^* \, d_p^*}{D_f^*(C_\infty - \overline{C_s})} = \frac{k_f^* d_p^*}{D_f^*} \qquad \text{(III.55)}$$

We now introduce the total mass transfer coefficient $\tilde{k}^*$ and write the additivity rule as:

$$\frac{1}{\tilde{k}^*} = \frac{1}{k_{in}^*} + \frac{1}{k_f^*} \qquad \text{(III.56)}$$

(III.56) can be reformulated in terms of Sherwood numbers. Introducing the reactive (i.e. total) Sherwood number $\widetilde{Sh} = \dfrac{\tilde{k}^* d_p^*}{D_f^*}$, we get:

$$\frac{1}{\widetilde{Sh}} = \frac{1}{\gamma Sh_{in}} + \frac{1}{Sh} \tag{III.57}$$

Finally, using the continuity of the flux density at ∂P, we can obtain Sh_{in} as a function of Sh, inert this in (III.57) and after some simple algebra get the following expression:

$$\widetilde{Sh} = Sh \frac{C_\infty - \overline{C_s}}{C_\infty - \overline{C_v}} = Sh \frac{\Delta \overline{C_s}}{\Delta \overline{C_v}} \tag{III.58}$$

with $\Delta \overline{C_s} = C_\infty - \overline{C_v}$ and $\Delta \overline{C_v} = C_\infty - \overline{C_s}$. Finally, using (III.50) and (III.52), we establish the expression of the reactive Sherwood number $\widetilde{Sh}$ of each sphere as:

$$\widetilde{Sh_j}(Re, Sc, \phi, \gamma) = \frac{Sh_j(Re, Sc)}{\dfrac{Sh_j(Re, Sc)}{2\gamma}\left[\dfrac{tanh(\phi/2)}{\phi/2 - tanh(\phi/2)} - \dfrac{12}{\phi^2}\right] + 1}$$
$$j = 1, 2, 3 \tag{III.59}$$

$Sh_j(Re, Sc)$ in the above expression is the individual Sherwood number for a sphere j in the convective-diffusive problem (without reaction) where the particle internal concentration is uniform, and the mass transfer is only controlled by the Reynolds number Re and the Schmidt number Sc. The 'reactive' Sherwood number, $\widetilde{Sh_j}(Re, Sc, \phi, \gamma)$, also depends on the Damkohler number $Da = \phi^2$ and the diffusion coefficient ratio γ, in addition to the first two dimensionless numbers for convection-diffusion. III.59 can further be written in an explicit form:

$$\frac{1}{\widetilde{Sh_j}} = \frac{1}{2\gamma}\left[\frac{tanh(\phi/2)}{\phi/2 - tanh(\phi/2)} - \frac{12}{\phi^2}\right] + \frac{1}{Sh_j} \tag{III.60}$$

III.60 has two asymptotic limits. When the reaction rate is very fast, i.e., the Thiele modulus $\phi \to \infty$, the term $\left[\frac{tanh(\phi/2)}{\phi/2 - tanh(\phi/2)} - \frac{12}{\phi^2}\right] \to 0$ and so $\widetilde{Sh_j} \to Sh_j$. In this case the system is limited by diffusion, i.e., controlled by mass transfer. When the reaction rate is very slow, i.e. the Thiele modulus $\phi \to 0$, the term $\left[\frac{tanh(\phi)}{\phi - tanh(\phi)} - \frac{3}{\phi^2}\right] \to \infty$, $\widetilde{Sh_j} \to 0$. In this case the system is controlled by internal reaction kinetics.

5.2   Model validation

We examine here how the model performs in the 3-aligned sphere configuration by spanning ranges of the 4 governing dimensionless numbers Re, Sc, γ and ϕ^2, as well as assorted interparticle distances. The mean surface concentration $\overline{C_s}$, given by (III.50), is the main unknown in the problem. Therefore, we primarily assess the validity of our proposed model by comparing $\overline{C_s}$ as computed by our DLM/FD-SIM numerical method to $\overline{C_s}$ as predicted by our model.

We vary the dimensionless parameters in the ranges: $Re \in [0, 100]$, $\phi^2 \in [0, \infty]$, $Sc \in [0.5, 10]$ and $\gamma \in [10^{-2}, 10^2]$ and select the following three different geometric

configurations:

— $d_{12} = 4$ and $d_{23} = 2$,

— $d_{12} = 2$ and $d_{23} = 4$,

— $d_{12} = 2$ and $d_{23} = 2$.

We first examine the influence of the geometric configuration. To do this, we set $Re = 50$, $\gamma = 0.1$, and $Sc = 1$ and keep them constant while we vary the Damkohler number ϕ^2 in the range $[0, 400]$ and compare our model to our numerical results for the three geometric configurations A, B, and C in FIG. III.20, FIG. III.21 and FIG. III.22, respectively. Overall, $\overline{C_s}$ as predicted by the model show a good agreement with computed $\overline{C_s}$ for the three geometric cases. Essentially, the error increases with the increase of ϕ^2 as the internal concentration boundary layer thickness decreases with the increase of ϕ^2 as $1/\phi$. However, the inter-particle distances have literally no impact on the magnitude of the differences between model predictions and numerical results. Even in configuration C where the 3 particles are the closest to each other, no significant difference is visible between FIG. III.22, and FIGS. III.20 and III.21. For the 3 configurations, the system is still dilute enough such that the first sphere behaves similarly, and quite close to a single isolated sphere.

From now on, we consider the geometric configuration A in the rest of this subsection. We fix $Re = 50$, $Sc = 1$, and $\phi^2 = 40$ and we vary the diffusion ratio γ in the range $[10^{-2}, 10^2]$. Once again, we compute numerically the mean surface concentration $\overline{C_s}$ and we compare it to the value predicted by the model for the three particles in FIG. III.23. Results show again a good agreement between model predictions and numerical results.

Finally, we examine the influence of Sc. To do this, we fix $Re = 50$, $\gamma = 0.1$, and $\phi^2 = 40$ and we vary $Sc \in [0.5, 10]$, which consequently varies $Pe \in [25, 500]$. Computed $\overline{C_s}$ is compared to $\overline{C_s}$ predicted by the model for the three particles in FIG. III.24. The agreement is deemed to be satisfactory.

We now plot $\overline{C_s}$ as a function of $Re \in [0, 100]$ and $\phi^2 \in [0, \infty]$ per particle for $\gamma = 0.1$ and $Sc = 1$. Computed values and values predicted by the model are compared in FIG. III.25 for the first sphere, FIG. III.26 for the second sphere and FIG. III.27 for the third sphere. We also compare the mean volume concentration $\overline{C_v}$ in FIG. III.28 for the first sphere, FIG. III.29 for the second sphere and FIG. III.30 for the third sphere. In general, the agreement between computed values and values predicted by the model is once again deemed to be satisfactory. The Damkohler number ϕ^2 has the most significant impact on the observed difference between computed values and model predictions. For $\phi^2 < 200$, the agreement in very satisfactory for all spheres and the observed difference is very small. Then for larger $\phi^2 > 200$, the observed difference, though still limited, increases with ϕ^2. The maximum difference of the order of 10% is attained for $\phi^2 = 4000$. As pointed

out in the above, this trend is related to the internal concentration boundary layer that decreases with the increase of the Thiele modulus as $1/\phi$. The same comments apply to the plots of the reactive Sherwood numbers given by (III.59) for the 3 spheres in FIG. III.31 for the first sphere, FIG. III.32 for the second sphere and FIG. III.33 for the third sphere.

— The observed differences between computed values of $\overline{C_s}$, $\overline{C_v}$ or $\widetilde{Sh}$ and the values of the same quantities predicted by the model have 3 sources:

— approximations and assumptions adopted to derive the model,

— not fully converged in space computed solutions for large values of ϕ^2,

correlations proposed for the coefficients β_j by Ramachandran et al. [1989] and established by a least square regression with a maximum error of 2.5% for β_1, 4.6% for β_2 and 10% for β_3.

In the case of the 3 aligned spheres, the equivalent solid volume fraction around the spheres is low and the system is representative of a dilute regime. The interactions between the 3 spherical obstacles, both in terms of momentum and mass transfer, are limited, though far from negligible. As a result, the chemical concentration does not vary much along each sphere surface as shown in FIG. III.34. Consequently, the approximations (III.51)-(III.52) to calculate the mean volume concentration, i.e., assuming that C is a function of the radial coordinate only and $C_s(\theta, \phi)$ does not vary too much around $\overline{C_s}$, are valid. The model is assumed to perform well in this flow configuration and this range of dimensionless parameters. So we believe that source 1 does not contribution much to the observed differences. The increase of the observed differences as a function of the Damkolher number ϕ^2 is certainly a sign that for high ϕ^2, $N_p = 70$ points per diameter might not yet be enough to yield fully spatially converged computed solutions as the internal boundary layer is getting thinner with the increase of ϕ^2, as suggested by FIG. III.7 and FIG. III.14. Source 2 is thereby a significant contribution to the observed differences at high ϕ^2. Finally, the magnitude of the error on the coefficients β_j as reported by Ramachandran et al. [1989] is of the same order as the observed differences, so we cannot rule out the contribution of source 3. Overall, the model performs well. The difference between computed values and model predictions increases with the Damkohler number ϕ but is capped to 10% in the range of dimensionless parameters investigated.

Figure III.20: Steady state convection-diffusion in the flow past 3 aligned reactive spheres: mean surface concentration $\overline{C_s}$ as a function of ϕ^2 in configuration A at $Re = 50$, $Sc = 1$ and $\gamma = 0.1$. Lines correspond to model and markers correspond to SIM. Red color corresponds to first sphere, blue color to second sphere and green color corresponds to third sphere.

Figure III.21: Steady state convection-diffusion in the flow past 3 aligned reactive spheres: mean surface concentration $\overline{C_s}$ as a function of ϕ^2 in configuration B at $Re = 50$, $Sc = 1$ and $\gamma = 0.1$. Lines correspond to model and markers correspond to SIM. Red color corresponds to first sphere, blue color to second sphere and green color corresponds to third sphere.

Figure III.22: Steady state convection-diffusion in the flow past 3 aligned reactive spheres: mean surface concentration $\overline{C_s}$ as a function of ϕ^2 in configuration C at $Re = 50$, $Sc = 1$ and $\gamma = 0.1$. Lines correspond to model and markers correspond to SIM. Red color corresponds to first sphere, blue color to second sphere and green color corresponds to third sphere.

Figure III.23: Steady state convection-diffusion in the flow past 3 aligned reactive spheres: mean surface concentration $\overline{C_s}$ as a function of γ in configuration A at $Re = 50$, $Sc = 1$ and $\phi^2 = 40$. Lines correspond to model and markers correspond to SIM. Red color corresponds to first sphere, blue color to second sphere and green color corresponds to third sphere.
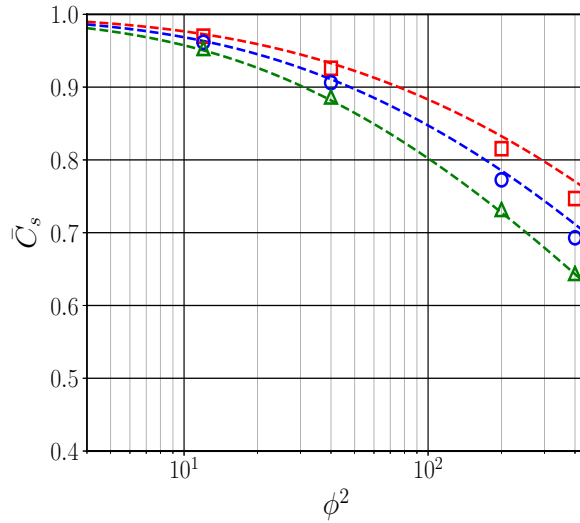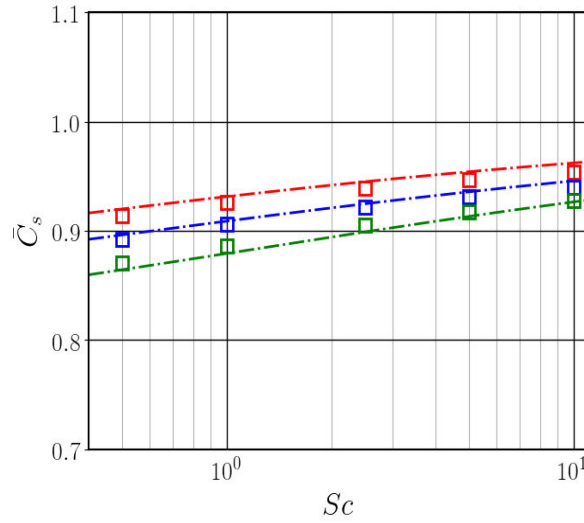
Figure III.24: Steady state convection-diffusion in the flow past 3 aligned reactive spheres: mean surface concentration $\overline{C_s}$ as a function of Sc in configuration A at $\phi^2 = 40$, $Re = 50$ and $\gamma = 0.1$. Lines correspond to model and markers correspond to SIM. Red color corresponds to first sphere, blue color to second sphere and green color corresponds to third sphere.
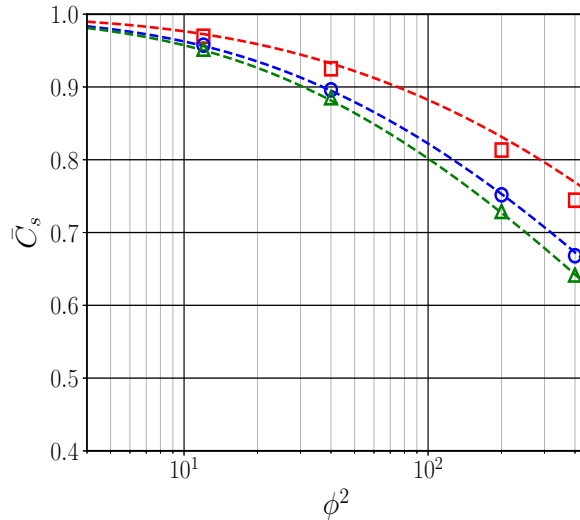

Figure III.25: Steady state convection-diffusion in the flow past 3 aligned reactive spheres: mean surface concentration $\overline{C_s}$ of sphere 1 as a function of Re in configuration A at $\gamma = 0.1$ and $Sc = 1$. Lines correspond to model and markers correspond to numerical simulation. Red color corresponds to $\phi^2 = 40$, blue color to $\phi^2 = 200$ and green color corresponds to $\phi^2 = 4000$.

Figure III.26: Steady state convection-diffusion in the flow past 3 aligned reactive spheres: mean surface concentration $\overline{C_s}$ of sphere 2 as a function of Re in configuration A at $\gamma = 0.1$ and $Sc = 1$. Lines correspond to model and markers correspond to numerical simulation. Red color corresponds to $\phi^2 = 40$, blue color to $\phi^2 = 200$ and green color corresponds to $\phi^2 = 4000$.
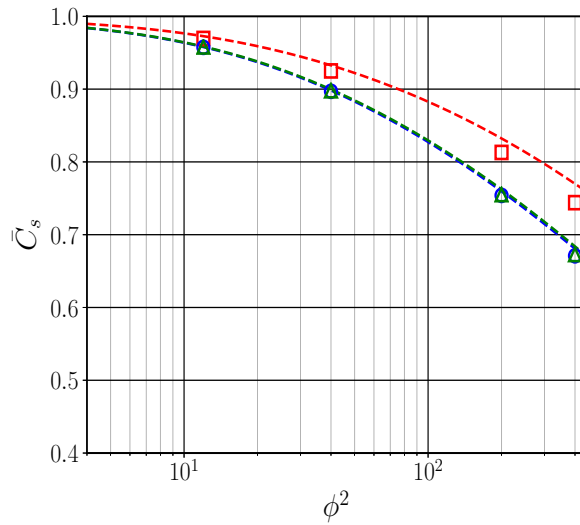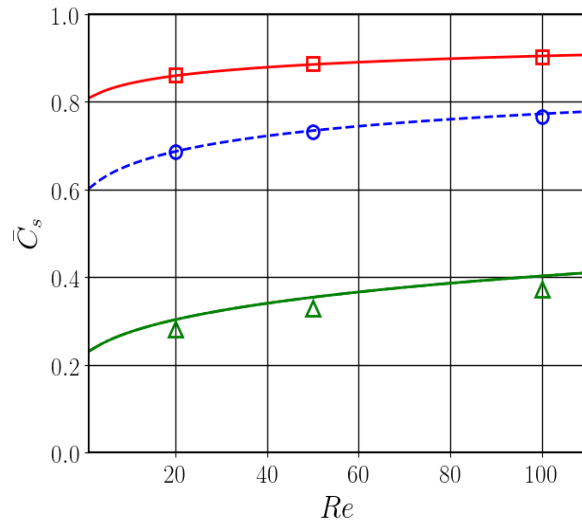

Figure III.27: Steady state convection-diffusion in the flow past 3 aligned reactive spheres: mean surface concentration $\overline{C_s}$ of sphere 3 as a function of Re in configuration A at $\gamma = 0.1$ and $Sc = 1$. Lines correspond to model and markers correspond to numerical simulation. Red color corresponds to $\phi^2 = 40$, blue color to $\phi^2 = 200$ and green color corresponds to $\phi^2 = 4000$.
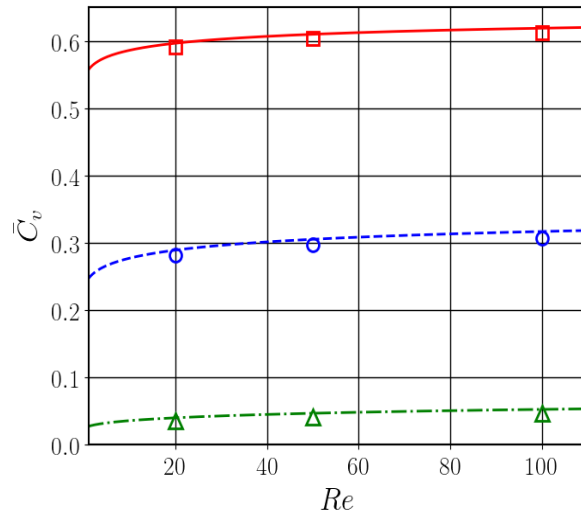
Figure III.28: Steady state convection-diffusion in the flow past 3 aligned reactive spheres: mean volume concentration $\overline{C_v}$ of sphere 1 as a function of Re in configuration A at $\gamma = 0.1$ and $Sc = 1$. Lines correspond to model and markers correspond to numerical simulation. Red color corresponds to $\phi^2 = 40$, blue color to $\phi^2 = 200$ and green color corresponds to $\phi^2 = 4000$.
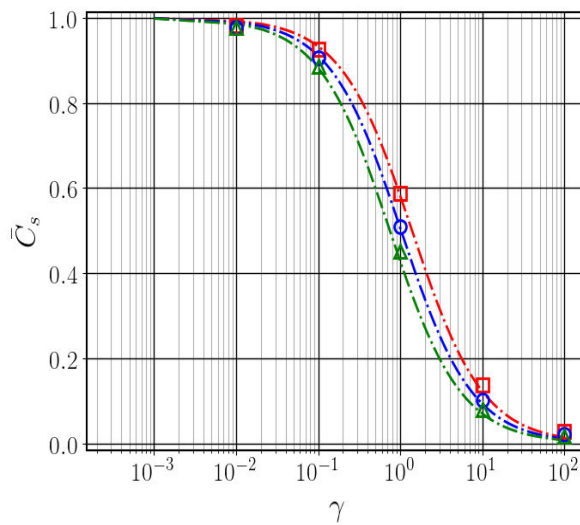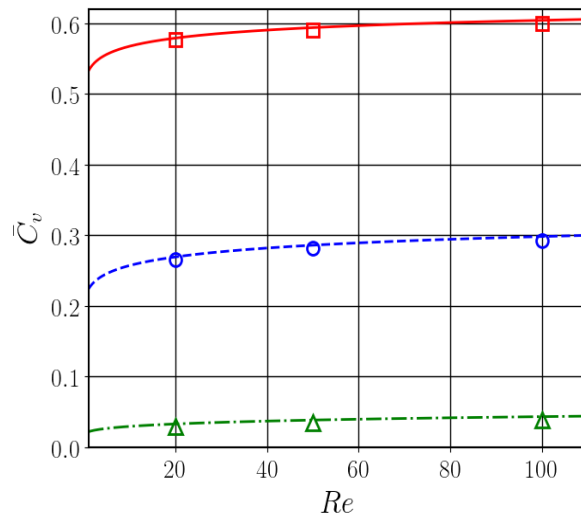

Figure III.29: Steady state convection-diffusion in the flow past 3 aligned reactive spheres: mean volume concentration $\overline{C_v}$ of sphere 2 as a function of Re in configuration A at $\gamma = 0.1$ and $Sc = 1$. Lines correspond to model and markers correspond to numerical simulation. Red color corresponds to $\phi^2 = 40$, blue color to $\phi^2 = 200$ and green color corresponds to $\phi^2 = 4000$.
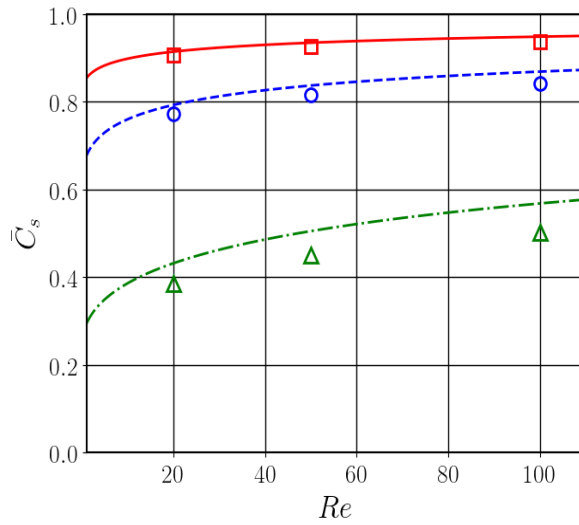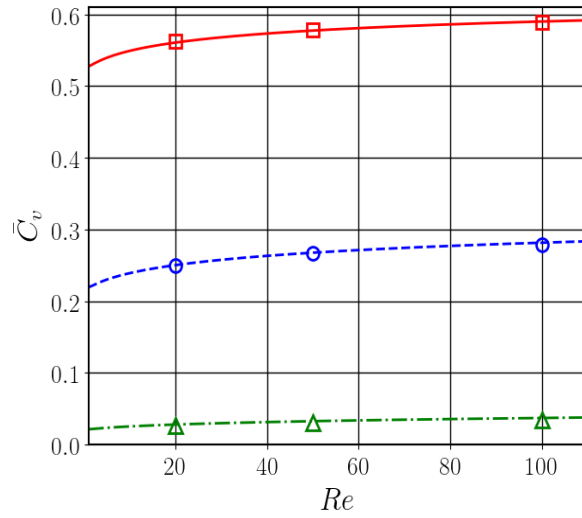
Figure III.30: Steady state convection-diffusion in the flow past 3 aligned reactive spheres: mean volume concentration $\overline{C_v}$ of sphere 3 as a function of Re in configuration A at $\gamma = 0.1$ and $Sc = 1$. Lines correspond to model and markers correspond to numerical simulation. Red color corresponds to $\phi^2 = 40$, blue color to $\phi^2 = 200$ and green color corresponds to $\phi^2 = 4000$.
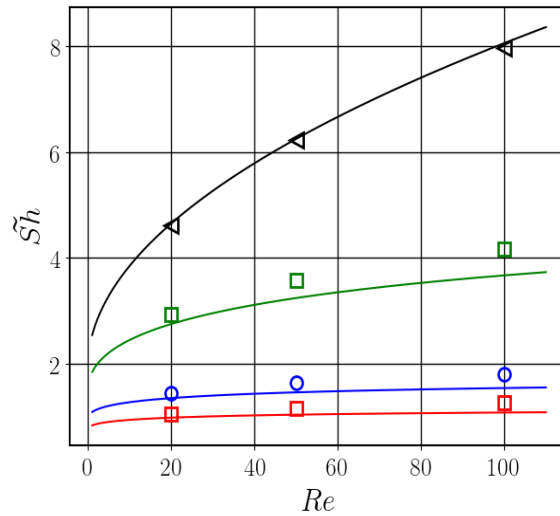
Figure III.31: Steady state convection-diffusion in the flow past 3 aligned reactive spheres: reactive Sherwood number $\tilde{Sh}$ of sphere 1 as a function of Re in configuration A at $\gamma = 0.1$ and $Sc = 1$. Lines correspond to model and markers correspond to numerical simulation. Red color corresponds to $\phi^2 = 40$, blue color to $\phi^2 = 200$, green color correspond to $\phi^2 = 4000$ and black color corresponds to $\phi^2 = \infty$.
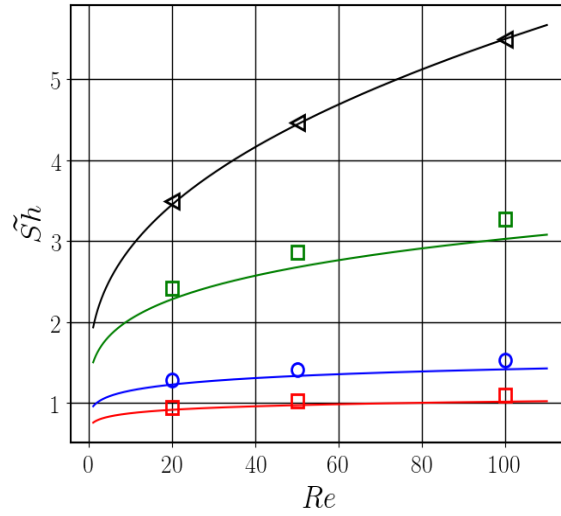
Figure III.32: Steady state convection-diffusion in the flow past 3 aligned reactive spheres: reactive Sherwood number $\tilde{Sh}$ of sphere 2 as a function of Re in configuration A at $\gamma = 0.1$ and $Sc = 1$. Lines correspond to model and markers correspond to numerical simulation. Red color corresponds to $\phi^2 = 40$, blue color to $\phi^2 = 200$, green color corresponds to $\phi^2 = 4000$ and black color corresponds to $\phi^2 = \infty$.
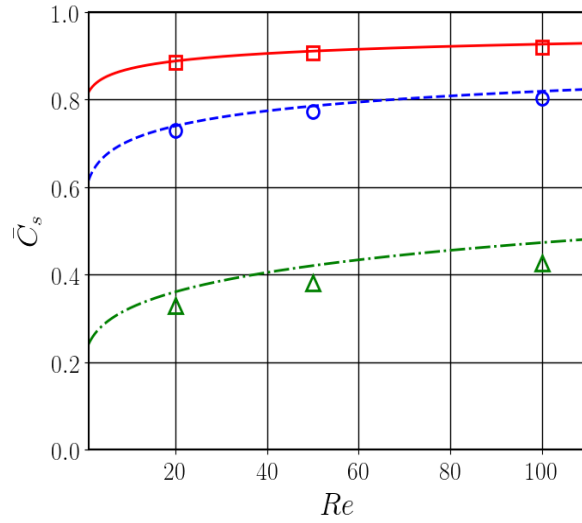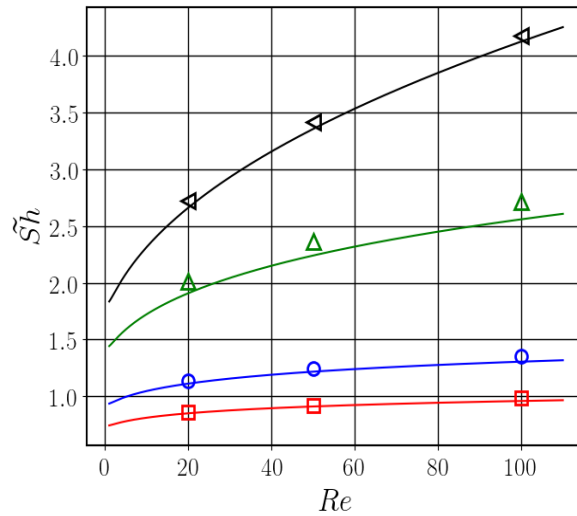

Figure III.33: Steady state convection-diffusion in the flow past 3 aligned reactive spheres: reactive Sherwood number $\tilde{Sh}$ of sphere 3 as a function of Re in configuration A at $\gamma = 0.1$ and $Sc = 1$. Lines correspond to model and markers correspond to numerical simulation. Red color corresponds to $\phi^2 = 40$, blue color to $\phi^2 = 200$, green color corresponds to $\phi^2 = 4000$ and black color corresponds to $\phi^2 = \infty$.

6   Discussion and perspectives

We presented a numerical framework that couples a Sharp Interface Method (SIM) for the convection-diffusion-reaction conservation equation of the chemical

species to a DLM/FD method to solve the incompressible Navier-Stokes equations with fixed obstacles. We presented multiple validation tests of growing complexity to ensure that our implementation of our DLM/FD-SIM method supplies computed solution with the expected accuracy. We have shown through various convergence tests, comparisons to analytical solutions, comparisons to correlations and comparisons to body-fitted simulations that our numerical tool indeed supplies reliable computed solutions. We then used our numerical tool to examine the problem of convective-diffusive mass transfer in the flow past 3 reactive spheres.

The primary objective of the work was to show that a reactive Sherwood number correlation can be constructed in a dilute system on the basis on a simple external-internal coupling and the additivity rule, in a similar way as we constructed a reactive Sherwood number correlation for a single isolated sphere in Sulaiman et al. [2018a]. Model predictions show a satisfactory agreement with our DLM/FD-SIM numerical results for wide ranges of the 4 governing parameters in the problem of convective-diffusive mass transfer in the flow past 3 reactive spheres. We consider this problem as an adequate toy model of a dilute particle-laden system experiencing hydrodynamic interactions. The strength of our reactive Sherwood number correlation is that it is based on any existing non-reactive Sherwood number correlation. Here we used the non-reactive Sherwood number correlations of Feng and Michaelides [2000] and Ramachandran et al. [1989], but this is not mandatory.

The ultimate objective is to extend the suggested reactive Sherwood number correlation to denser regime and eventually to use it in larger scale numerical models as Euler/Lagrange and Euler/Euler modelling of reactive particle-laden flows. This can be achieved in 2 complementary ways. The former way involves investigating pairwise interactions in terms of reactive mass transfer. A model system would be the flow past 2 spheres not aligned with the flow and then investigate not only the effect of the inter-particle distance but also of the relative angular position of the 2 particles, in a similar way to Akiki et al. [2017] for momentum transfer. The latter way involves computing the flow through a random array of reactive spheres up to a high solid volume fraction α_s close to packing, as illustrated in Fig. III.35. This would require large computing resources to span all parameter ranges but is feasible as our code is fully parallel and can run on large supercomputers with a satisfactory scalability. This work is currently under way.

(a) $\phi^2 = 40$

(b) $\phi^2 = 200$

(c) $\phi^2 = \infty$
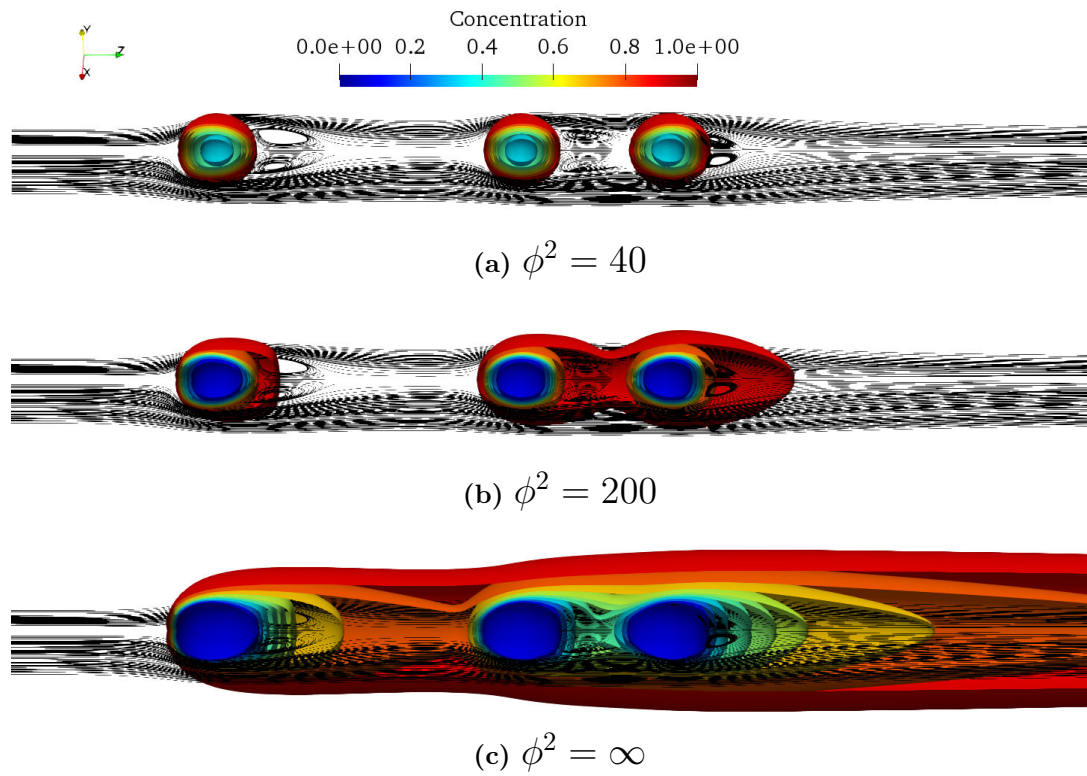
Figure III.34: Steady state convection-diffusion in the flow past 3 aligned reactive spheres: concentration iso-surfaces in configuration A at $Re = 50$, $\gamma = 0.1$, $Sc = 1$ and different ϕ^2.

(a) $\phi^2 = 40$ (b) $\phi^2 = 200$ (c) $\phi^2 = \infty$
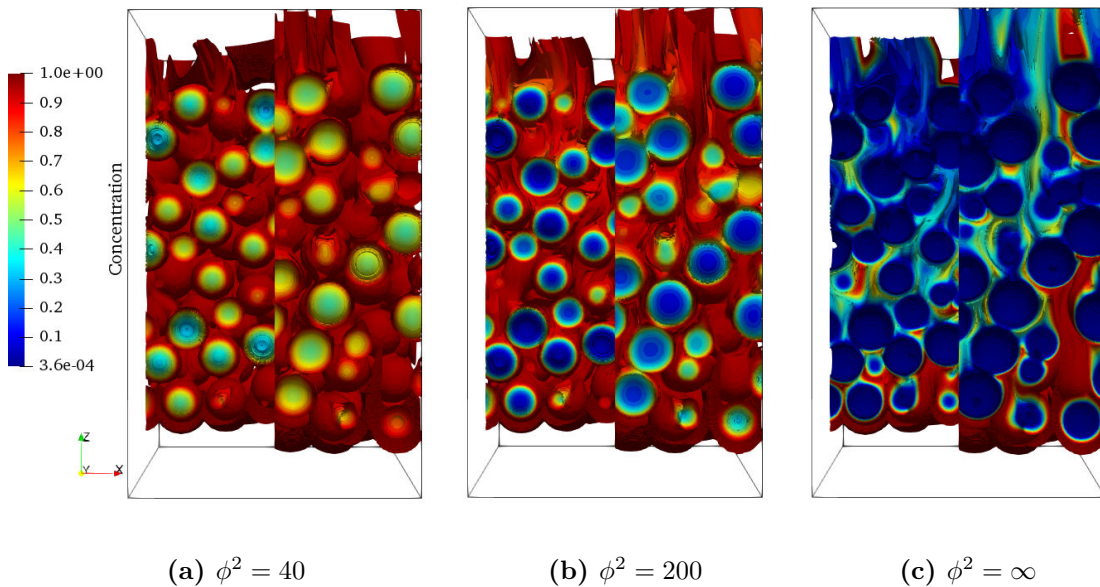
Figure III.35: Concentration iso-surfaces in the the flow through a random array of spheres at $Re = 25$, $\gamma = 0.1$, $Sc = 1$, $\alpha_s = 0.5$ and different Damkohler numbers ϕ^2.

7 Appendices

Derivation of the diffusive Sherwood number in a finite spherical domain

We consider a sphere of radius r_p^* at concentration $C = C_s|_{r^*=r_p^*}$ at the center of a spherical domain of radius $r^* = r_\infty^*$ filled with a quiescent fluid of diffusion coefficient D_f^*. At steady state, the concentration distribution C in the fluid is governed by:

$$D_f^* \nabla^2 C = 0 \tag{III.61}$$

(III.61) can easily be integrated with the two Dirichlet boundary conditions $C = C_s|_{r^*=r_p^*}$ and $C = C_\infty|_{r^*=r_\infty^*}$. The solution, i.e., the concentration profile $C(r^*)$ in the fluid phase, reads:

$$C(r^*) = \frac{r_p^* r_\infty^*}{(r_p^* - r_\infty^*)r^*}(C_\infty - C_s) + \frac{C_s r_p^* - C_\infty r_\infty^*}{r_p^* - r_\infty^*} \tag{III.62}$$

The mass transfer coefficient k^* can be calculated through the calculation of the total flux through the sphere surface as:

$$k^* = \frac{D_f^*}{4\pi r_p^{*2}(C_\infty - C_s)} \int_0^{2\pi} \int_{-\pi/2}^{+\pi/2} \left.\frac{\partial C(r^*)}{\partial r^*}\right|_{r^*=r_p^*} r_p^{*2} sin(\theta) d\varphi d\theta \tag{III.63}$$

Substituting (III.62) into (III.63), the diffusive Sherwood number in a finite spherical domain $Sh = \dfrac{k^* d_p^*}{D_f^*}$ can be written as:

$$Sh = \frac{k^* d_p^*}{D_f^*} = \frac{2r_\infty^*}{r_\infty^* - r_p^*} \tag{III.64}$$

For an infinite domain, i.e., when $r_\infty^* \to \infty$, $Sh \to 2$. For a spherical domain of finite size, Sh is larger than 2 and its value can be calculated by (III.64).

Part IV

Mass transfer coupled with chemical reaction through a random array of fixed particles in a fluid flow

This chapter will be submitted to Chemical Engineering Science and its content is subject to modification.

Contents

Part IV. Mass transfer coupled with chemical reaction through a random array of fixed particles in a fluid flow

Abstract

Keywords: Mass transfer, Catalyst particle, Chemical reaction, Damkohler number, Sherwood number, Sharp Interface Method, Numerical modeling.

In [Sulaiman et al., 2018a] we introduced a model for a 'reactive' Sherwood number for a single particle immersed in a convective-diffusive fluid stream. The model accounts for the effects of external convection-diffusion along with a first order internal reaction with an internal diffusion. In [Sulaiman et al., 2018b] we extended the model for a system of three aligned interacting spheres. In this study, we investigate the effect of chemical reaction through a network of reactive catalyst particles. We use a coupled Sharp Interface / Discrete Lagrange Multiplier-Fictitious Domain Method (SIM-DLM/FD), thoroughly validated in our previous study, to treat particulate flow systems involving convection-diffusion in fluid phase and internal diffusion-reaction in a network of solid spherical catalyst particles. We handle the problem through internal-external coupling by means of concentration and flux continuities as boundary conditions. We present a model that predicts cup-mixing concentration profile as well as the mean surface and volume concentration profiles of the particles. We present a model for the 'reactive' Sherwood number that depends on 5 parameters: The Reynolds number Re, the Schmidt number Sc, the Damkohler number Da, the internal-external diffusion coefficient ratio γ and the solid volume fraction α_s. We validate the model through Direct Numerical Simulation (DNS) for a wide range of the aforementioned dimensionless parameters, we show and discuss its limitations.

Graphical Abstract

(a)   (b)   (c)

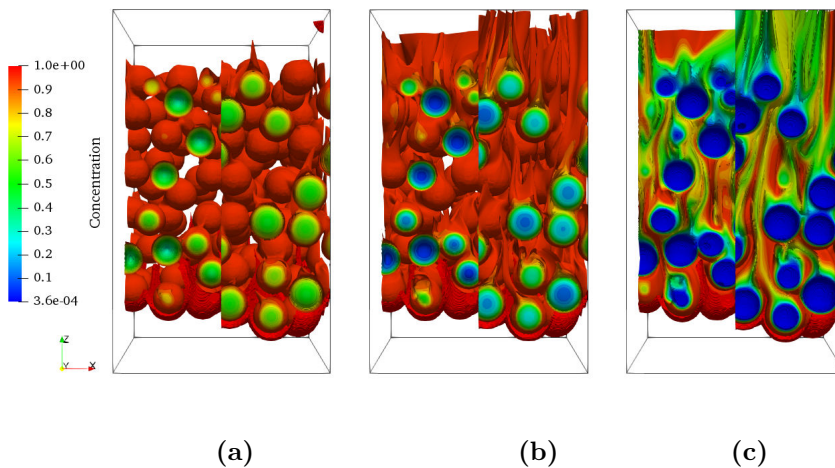**Figure IV.1:** Concentration iso-contours at $Re = 25$, $\gamma = 0.1$, $\alpha_s = 0.3$ and different Damkohler numbers. a) $Da = 40$, b) $Da = 200$ and c) $Da = \infty$

1   Introduction

Systems composed of two interacting solid and fluid phases are relevant for industrial processes operated in the domain of energy conversion. Catalytic fixed bed reactors [Wehinger et al., 2015] and fluidized bed reactors [Gao et al., 2008] are widely used in petrochemical processes for catalytic cracking of long chain hydrocarbons, to break them into lighter products that can be used to run engines. Biomass catalytic co-pyrolysis processes [Zhang et al., 2018], Biomass gasification [Bridgwater, 1995, Turn et al., 1998], and Biomass complete combustion [Baxter, 1993], are processes operated to extract liquid bio-fuel from organic substances. In the aforementioned systems, fluid flows through a network of solid particles where many physical phenomena take place, such as heat, mass and momentum transfer. The advanced comprehension of these systems is of tremendous importance for their design, operation, maintenance and process optimization. The comprehension is still incomplete due to the coupling among many physical phenomena. Usually, chemical reactions take place in these systems to enhance mass transfer, associated with heat transfer due to endothermic/exothermic reactions, whereas momentum transfer drives flow involved in convection phenomenon.

Investigating coupling phenomena in particulate flows can be achieved by means of Particle-Resolved Direct Numerical Simulations (PR-DNS) that fully resolve local interactions between the two phases. Indeed, the emergence of supercomputers with their increasing computational capacity over time has encouraged scientists to develop numerical methods to simulate systems by solving their momentum, mass and heat balance equations at the level of the particle. DNS is able, so far, to simulate particulate flow systems consisting of thousands of particles and provide reliable information about their heat, mass and momentum transfer at particle scale [Sun et al., 2016]. Although efficient, DNS is still incapable of simulating industrial scale systems that contain billions of particles. The DEM-CFD methods are computational fluid dynamics models, that solve the averaged equations of the momentum, mass and heat balance. The advantage of these methods is that they can treat a bigger number of particles, but without resolving the local interaction details at the particle scale. The local interactions in these models are accounted for through closure laws, such as the Nusselt number correlations for heat transfer, Sherwood number for mass transfer, and Drag coefficient for momentum transfer [Deen et al., 2014]. These correlations are used as closure laws to provide the unresolved local information, at the particle scale. Thus, DNS can be used to establish correlations incorporating the local interaction effects and these correlations can later be used to enhance the DEM-CFD model. This approach is referred to as the 'multi-scale' approach [van der Hoef et al., 2004].

Many DNS methods are available in literature and can be employed to simulate particulate flow problems. The fixed mesh methods that use a regular cartesian grid are commonly used for the treatment of problems involving moving particles. The main advantage behind the choice of these methods is that computational methods have a very good scalability on supercomputers. Their disadvantage lies in the difficulty of imposing the correct boundary conditions at particles surface.

Part IV. Mass transfer coupled with chemical reaction through a random array of fixed particles in a fluid flow

The Immersed Boundary Method (IBM) [Uhlmann, 2005], is a fixed mesh computational method, that imposes boundary conditions at the particle surface by means of Lagrangian markers. This method has been applied by Xia et al. [2014] to study convective heat/mass transfer for a single particle. IBM was also used to evaluate the heat transfer Nusselt number in dense particulate flow systems by Deen et al. [2014] and Sun et al. [2015]. More recently, Lu et al. [2018] employed an IBM to study mass transfer with a first order irreversible surface chemical reaction and applied it to a single stationary sphere under forced convection. The Lattice Boltzmann Method (LBM) is also a fixed mesh computational method. LBM solves convection-collision steps of probability density functions instead of solving classical conservation equation. It has been employed to simulate particulate flows with heat transfer by Khiabani et al. [2010] and Kruggel-Emden et al. [2016]. [Derksen, 2014] employed LBM to study mass transfer through fixed and fluidized beds of particles. [Bohn et al., 2012] studied gas-solid diffusion-reaction within a single particle by means of LBM. The Distributed Lagrange Multiplier / Fictitious Domain Method (DLM/FD), firstly introduced by Glowinski et al. [2001], combines the particle and fluid equations of motion into a single, weak, and general equation of motion called combined momentum equation, also uses a fixed cartesien mesh. The combined equations are derived through the combined velocity space incorporating the rigid body motion (no-slip) in the particle. The DLM/FD method has been employed to simulate heat/mass transfer by Yu et al. [2006], Dan and Wachs [2010] and Wachs [2011b].

The Sharp Interface Method (SIM), or as alternatively referred to, the Ghost Fluid Method (GFM), is a fixed-mesh computational method employed to accurately enforce boundary conditions with discontinuities along embedded interfaces [Shi et al., 2011], where jump conditions are incorporated in the discretization of the differential operators on the Cartesian grid in the vicinity of the interface. SIM was firstly introduced by Fedkiw et al. [1999] and employed to impose boundary conditions at a contact discontinuity in the inviscid Euler equations. Udaykumar and Mao [2002] and Gibou et al. [2003] used SIM to study the evolution of solidification fronts with heat transfer and solute transport in dendritic solidification. Kang et al. [2000] extended SIM to treat multiphase incompressible flows including effects of viscosity, surface tension and gravity and applied the method to two-phase water-air mixtures. Shao et al. [2012] combined SIM with a Fictitious Domain method to simulate heat transfer in particulate flows with heat diffusion inside particles.

In this study, we investigate the effect of a first order irreversible chemical reaction on mass transfer. The reaction takes place within a network of catalyst particles through which a fluid with an imposed inlet concentration flows. For an infinite reaction rate, the system is said to be a 'Mass transfer' controlled and the problem is analogous to heat transfer problems with temperature imposed at the particle surface, previously studied by [Sun et al., 2016, Deen et al., 2014, Tavassoli et al., 2013] and [Gunn, 1978]. The analogy with heat transfer fails when the reaction rate is finite and the system is not 'Mass transfer' controlled. In this case, the Sherwood number correlations established for heat transfer are no more capable of describing the physics of the system. According to reaction kinetics, one of the three following regimes can predominate. When the reaction rate is very slow compared

to diffusion, the surface concentration of the particles is equal to the bulk concentration and the regime is said to be kinetics controlled. When the reaction rate is infinitely fast compared to diffusion rate, the surface concentration approaches zero and the system is controlled by mass transfer (diffusion limited). In between the two mentioned cases, the system is neither mass transfer nor kinetics controlled and the catalyst surface concentration is unknown. The main aim of this study is to establish a Sherwood number model that covers the three kinetic regimes and accounts for the effects of convection-diffusion, reaction and solid volume fraction within a fixed a bed of particles.

Governing equations and numerical model

Governing equations and numerical model have been described in detail in Part(III), sections 2 and 3.

2   Problem definition and Geometry

We consider the geometric configuration depicted in FIG. IV.2. The domain dimensions are $x = y = 6$ and $z = 16$. Particles are randomly distributed in the packing region $x \in [0, 6]$, $y \in [0, 6]$ and $z \in]4, 12[$. The sub-regions $z \in [0, 4]$ and $z \in [12, 16]$ have been left free of particles. The fluid enters the flow domain on the left boundary with an imposed fluid velocity $\mathbf{u} = (0, 0, 1)$ and a concentration $C = C_\infty = 1$. Periodic boundary conditions are imposed in x and y directions while a classical outflow boundary condition $\frac{\partial \mathbf{u}}{\partial z} = \frac{\partial C}{\partial z} = 0$ and $p = p_{ref} = 0$ is imposed at the outlet boundary. Solid phase is considered as catalyst particles with internal effective diffusivity D_s^*, effective reactivity k_s^* and diameter d_p^*. The solid volume fraction α_s is chosen such that $\alpha_s \in [0.1, 0.5]$. Up to $\alpha_s = 0.3$, particles are randomly distributed through uniform random seeding of non-overlapping spheres. For $\alpha_s > 0.3$, particles are initially distributed at solid volume fraction $\alpha_{si} = 0.25$, with particles diameter $d_{p_i} < d_p$. Then, particles radius is expanded. During expansion, particles undergo multiple collisions before they reach the final diameter d_p, that satisfies the desired value α_s. Particle-particle contact is handled with Grains3D granular solver. Five independent random particle seeding will be used in mass transfer simulation.

Geometry and particles distribution
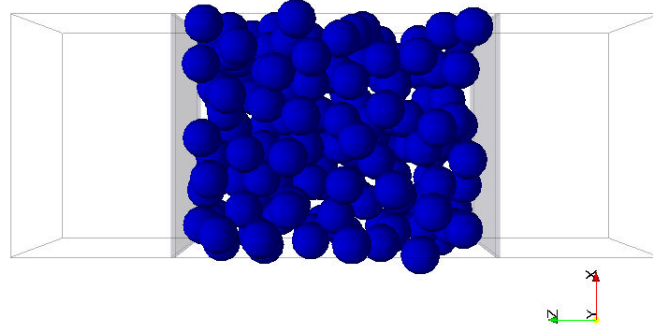
Figure IV.2: Used geometric configuration. $\alpha_s = 0.3$.

2.1 Sherwood number in mass transfer controlled system

The classic prediction of mass transfer in a two-phase fluid-solid reactor (catalyst particles undergoing an internal diffusion-reaction, associated with an external convection-diffusion) is to decouple the internal and external transfer in the system. Then the two separated problems can be coupled at the solid-fluid interface, through concentration and flux continuities. Therefore, the external Sherwood number can be assumed to be constant and unaffected by the internal chemical reaction. Based on this assumption, the external mass transfer coefficient can be utilized, in addition to the boundary conditions, to couple the internal-external coupling. As a first step, we evaluate the reference Sherwood number in mass transfer controlled system, i.e $Da = \infty$ or an infinite reaction rate. The system in this case is analogous to heat transfer problem with particles at fixed temperature. We define the cup-mixing, or flow-averaged concentration as :

$$\overline{C}(z) = \frac{\int \int_{S_f} u_z(x,y,z)C(x,y,z)dxdy}{\int \int_{S_f} u_z(x,y,z)dxdy} \tag{IV.1}$$

with S_f the cross-section area of the fluid and u_z the fluid velocity component along the z direction. The balance equation for the cup-mixing concentration in the system along the z direction can be written as follows:

$$\frac{d\overline{C}(z)}{dz} + \xi(\overline{C}(z) - C_s) = 0 \tag{IV.2}$$

where C_s is the particle concentration and ξ is a measure of external mass transfer, defined as $\xi = \frac{6\alpha_s Sh}{Pe}$. Hence, the concentration profile along the z direction in the bed is solution of (IV.2) and can be written as:

$$\overline{C}(z) = (C_\infty - C_s)exp(-\xi z) + C_s \tag{IV.3}$$

In the above equation the value of ξ can be determined through the fitting with concentration profile obtained numerically. α_s and Pe being fixed, the value of ξ obtained by the fitting determines the value of the Sherwood number from simulations.

Part IV. Mass transfer coupled with chemical reaction through a random array of fixed particles in a fluid flow

We have performed a set of simulations at constant $Sc = 1$ and $Re \in [0, 100]$. We considered two solid volume fractions $\alpha_s = 0.1$ and $\alpha_s = 0.3$. The particle surface concentration is fixed to zero by setting $k_s^* = \infty$ or $(Da = \infty)$. We calculate Sh through the fitting with the $1D$ model (IV.2). For each (Re, Sc, α_s) we take the average of Sh resulting from 5 different random configurations. The numerical spatial resolution in this case is set to $N_d = 24$ and simulations are performed at $CFL < 0.25$. We compare the Sherwood number obtained from our simulations with the previously established correlations of [Sun et al., 2016], [Deen et al., 2014] and [Gunn, 1978] in Fig. IV.3. Our results show an over estimate of the correlations of [Deen et al., 2014] and [Sun et al., 2016] for both $\alpha_s = 0.1$ and $\alpha_s = 0.3$. The results at $\alpha_s = 0.3$ are closer to both correlations than those at $\alpha_s = 0.1$. In both cases the results under estimate the correlation of [Gunn, 1978], (IV.4).

$$Sh = (7 - 10\alpha_f + 5\alpha_f^2)(1 + 0.7Re^{0.2}Sc^{1/3}) + (1.33 - 2.4\alpha_f + 1.2\alpha_f^2)Re^{0.7}Sc^{1/3} \quad \text{(IV.4)}$$

It is remarkable that with the increase of Re, the results get closer to those of [Gunn, 1978] for both α_s. Similar study was carried out by Euzenat [2017] on heat transfer through fixed beds of particles and compared the Nusselt number with previous correlations.

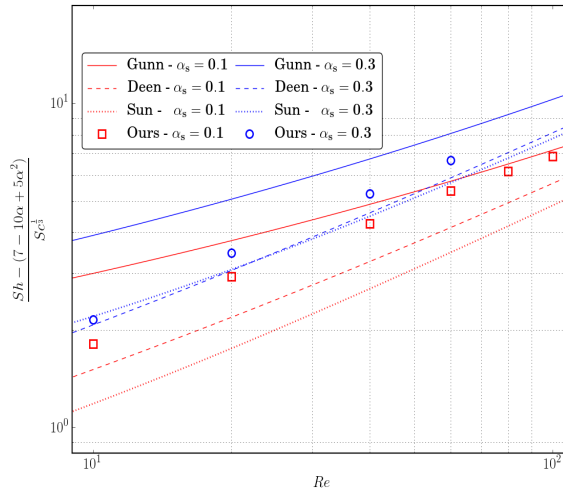**Figure IV.3:** Comparison of Sherwood number for external mass transfer with previous correlations.

3   Effect of chemical reaction

Now we consider a system where a finite chemical reaction takes place, i.e. $0 < Da < \infty$. We recall important results from the single particle system (for a particle undergoing a first order reaction placed in a fluid stream). The particle mean surface concentration can be written as:

Part IV. Mass transfer coupled with chemical reaction through a random array of fixed particles in a fluid flow

$$\overline{C_s} = \frac{C_\infty}{1 + \frac{2\gamma}{Sh}\left(\frac{\phi/2}{tanh(\phi/2)} - 1\right)} \tag{IV.5}$$

The mean volume concentration of the particle is the integration of the concentration profile given in (IV.6):

$$C(r^*) = C_s \frac{r_p^* \sinh(\phi r^*)}{r^* \sinh(\phi r_p^*)} \tag{IV.6}$$

$$\overline{C_v} \simeq \frac{3}{4\pi r_p^{*3}} \int_0^{2\pi} \int_{-\pi/2}^{+\pi/2} \int_0^{r_p^*} C_s(\phi,\theta)\frac{r_p^* \sinh(\phi r^*)}{r^* \sinh(\phi r_p^*)} sin(\theta) r^{*2} d\varphi d\theta dr^* \tag{IV.7}$$

and the integral can further be approximated as:

$$\begin{aligned}\overline{C_v} &\simeq \frac{3\overline{C_s}}{4\pi r_p^{*3}} \int_0^{2\pi} \int_{-\pi/2}^{+\pi/2} \int_0^{r_p^*} \frac{r_p^* \sinh(\phi r^*)}{r^* \sinh(\phi r_p^*)} sin(\theta) r^{*2} d\varphi d\theta dr^* \\ &= \frac{6}{\phi}\left(\frac{1}{tanh(\phi)} - \frac{2}{\phi}\right)\overline{C_s}\end{aligned} \tag{IV.8}$$

where $\overline{C_s}$ is the mean surface concentration is a constant given by (IV.5). The mean volume concentration $\overline{C_v}$ for a single sphere can finally be written as follows:

$$\overline{C_v} = \frac{3C_\infty}{1 + \frac{2\gamma}{Sh}\left(\frac{\phi/2}{tanh(\phi/2)} - 1\right)}\left(\frac{2}{\phi tanh(\phi/2)} - \frac{4}{\phi^2}\right) = \delta\sigma C_\infty \tag{IV.9}$$

with Sh, is the particle external Sherwood number. This assumption was validated in [Sulaiman et al., 2018a] for the single particle case, and for three aligned particles in [Sulaiman et al., 2018b]. In the previous cases, the particle Sh was known and it was evaluated through previously established correlations, such as [Feng and Michaelides, 2000] for a single particle. For the case of multiple-particle system, the individual Sh is unknown. In addition, the bulk concentration C_∞ that is constant in cases of single and three aligned particles, is variable along the z direction for a network of particles due to the consumption of the bulk concentration. Thus, the mean surface concentration of the particles' needs to be predicted along z in order to be able to calculate the internal and external concentration gradients. The problem can be solved through the additivity rule. The rule states that the total resistance to mass transfer in the system can be considered as a sum of two resistances in series. The first resistance is the inverse of the internal mass transfer coefficient k_{in}^*, solid phase, and the second is the external coefficient k_f^* within the fluid phase. The total mass transfer coefficient $\tilde{k}^*$, via the additivity rule, writes as:

$$\frac{1}{\tilde{k}^*} = \frac{1}{k_{in}^*} + \frac{1}{k_f^*} \tag{IV.10}$$

We consequently introduce the two Sherwood numbers as:

Part IV. Mass transfer coupled with chemical reaction through a random array of fixed particles in a fluid flow

— internal Sherwood number Sh_{in}

$$Sh_{in} = \frac{N_{s,\partial P}^* \, d_p^*}{D_s^* (\overline{C_s} - \overline{C_v})} = \frac{k_{in}^* d_p^*}{D_s^*} \tag{IV.11}$$

— external Sherwood number Sh

$$Sh = \frac{N_{f,\partial P}^* \, d_p^*}{D_f^* (C_\infty - \overline{C_s})} = \frac{k_f^* d_p^*}{D_f^*} \tag{IV.12}$$

(IV.10) can be reformulated in terms of Sherwood numbers. Introducing the total Sherwood number of the system $\widetilde{Sh} = \dfrac{\tilde{k}^* d_p^*}{D_f^*}$, we get:

$$\frac{1}{\widetilde{Sh}} = \frac{1}{\gamma Sh_{in}} + \frac{1}{Sh} \tag{IV.13}$$

The expression of $\widetilde{Sh}$ can be written as function of Sh, $\Delta \overline{C_s} = C_\infty - \overline{C_s}$ and $\Delta \overline{C_v} = C_\infty - \overline{C_v}$, using the continuity of the flux density at ∂P, it reads as follows:

$$\widetilde{Sh} = Sh \frac{C_\infty - \overline{C_s}}{C_\infty - \overline{C_v}} = Sh \frac{\Delta \overline{C_s}}{\Delta \overline{C_v}} \tag{IV.14}$$

Using (IV.5) and (IV.8), the reactive Sherwood number $\widetilde{Sh}$ of a sphere can be written as:

$$\widetilde{Sh}(Re, Sc, \phi, \gamma) = \frac{Sh(Re, Sc)}{\dfrac{Sh(Re, Sc)}{2\gamma} \left[\dfrac{tanh(\phi/2)}{\phi/2 - tanh(\phi/2)} - \dfrac{12}{\phi^2} \right] + 1} \tag{IV.15}$$

accounting for external mass transfer and internal chemical reaction.

3.1 Multiple-particle system

We will approach the problem using the analogy with the single particle system (IV.5). The key point of the problem is to predict the internal and external concentration differences. The first is the external gradient $\Delta \overline{C_s}(z) = \overline{C}(z) - \overline{C_s}(z)$, the gradient between the bulk cup-mixing and mean particle surface concentration. The second is $\Delta \overline{C_v}(z) = \overline{C}(z) - \overline{C_v}(z)$, through which the internal gradient between the mean surface and mean volume concentration. We consider the averaged over 5 different sets of randomly distributed particles. We assume that the mean surface concentration of the particles at z can be approximated as :

$$\overline{C_s}(z) = \frac{\overline{C}(z)}{1 + \dfrac{2\gamma}{Sh} \left(\dfrac{\phi/2}{tanh(\phi/2)} - 1 \right)} \tag{IV.16}$$

We will call hereafter, the concentration drop between the cup-mixing and the mean surface concentration of the particles as δ :

$$\delta = \overline{C}_s(z)/\overline{C}(z) = \cfrac{1}{1 + \frac{2\gamma}{Sh}\left(\frac{\phi/2}{tanh(\phi/2)} - 1\right)} \tag{IV.17}$$

with *Sh* the external Sherwood number that can be determined from mass transfer controlled system. In single particle system it was evaluated through existing correlations such as [Feng and Michaelides, 2000] and for a bed of particles it can be evaluated through correlations of [Gunn, 1978] or [Deen et al., 2014].

The equation describing the cup-mixing concentration profile along the z direction, taking into account the variation of the particle surface concentration along z, becomes:

$$\frac{d\overline{C}(z)}{dz} + \xi\left(\overline{C}(z) - \overline{C}_s(z)\right) = 0 \tag{IV.18}$$

Taking into account the assumption made in (IV.16), the equation can further be written as:

$$\frac{d\overline{C}(z)}{dz} + \xi(1 - \delta)\overline{C}(z) = 0 \tag{IV.19}$$

The cup-mixing concentration profile, accounting for the evolution of the particle concentration as function of z is the solution of the above equation, and it writes as follows:

$$\overline{C}(z) = C_\infty exp(-\xi(1 - \delta)z) \tag{IV.20}$$

Note that we assumed δ to be constant, $0 < \delta < 1$. For very slow reaction, i.e $Da \ll 1$, $\delta \rightarrow 1$. For very fast reaction i.e $Da \rightarrow \infty$, $\delta \rightarrow 0$ and (IV.20) is equivalent to (IV.3). ξ is the external mass transfer coefficient that is assumed to be independent of reaction rate.
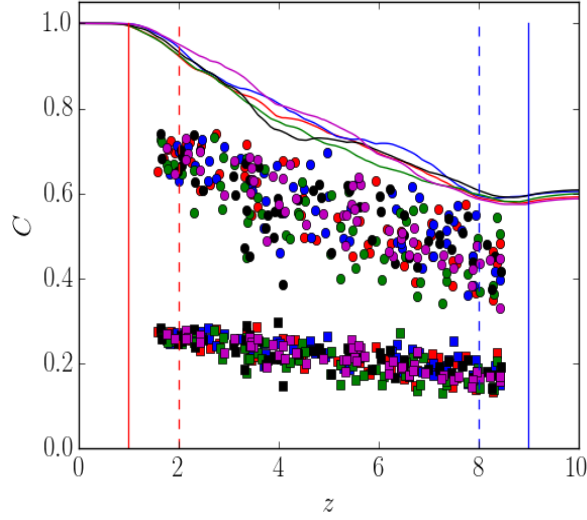
Figure IV.4: Concentration distribution along the bed. Continuous lines correspond to cup-mixing concentration. Disks correspond to mean surface concentration $\overline{C}_s$ and squares correspond to mean volume concentration $\overline{C}_v$. Different colors correspond to the five different solid particles random distributions. The dimensionless parameters are fixed to $Re = 10$, $Da = 50$, $Sc = 1$, $\gamma = 0.1$.
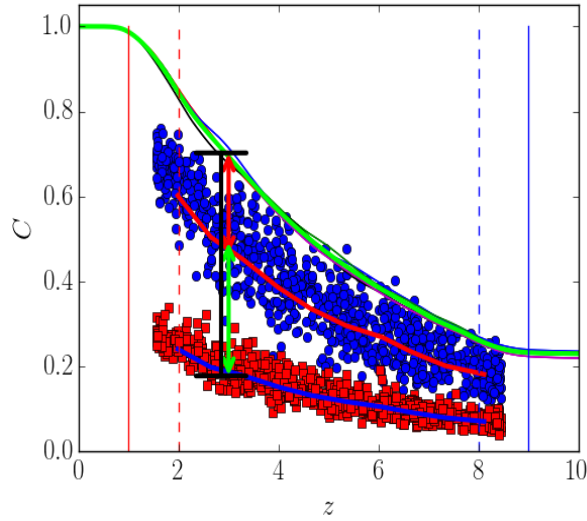
Figure IV.5: Concentration distribution along the bed. Green continuous line corresponds to cup-mixing concentration, red line corresponds to average of mean surface concentration and blue line to average of mean volume concentration. Disks correspond to mean surface concentration $\overline{C}_s$ and squares correspond to mean volume concentration $\overline{C}_v$. Red vertical arrow corresponds to $\Delta \overline{C}_s(z) = \overline{C}(z) - \overline{C}_s(z)$, black bar corresponds to $\Delta \overline{C}_v(z) = \overline{C}(z) - \overline{C}_v(z)$. The internal concentration differences are represented by the green vertical arrow.

Before going further with the assumption, we need to verify that the external mass transfer coefficient is independent of Da. To do so, we re-write (IV.18) in the following form:

Part IV. Mass transfer coupled with chemical reaction through a random array of fixed particles in a fluid flow

$$\xi = -\frac{1}{(\overline{C}(z) - \overline{C}_s(z))}\frac{d\overline{C}(z)}{dz} \tag{IV.21}$$

We compute ξ numerically for two cases. Case 1, $\alpha_s = 0.1$, $Re = 50$, $Sc = 10$ and $\gamma = 0.1$. Case 2, $\alpha_s = 0.3$, $Re = 10$, $Sc = 10$ and $\gamma = 0.1$. In each case we consider three values of Da. $Da = 40$, $Da = 200$, and $Da = \infty$. We compare the results in FIG. IV.6 for the two cases. FIG. IV.6 shows that ξ is constant as function of z and Da.
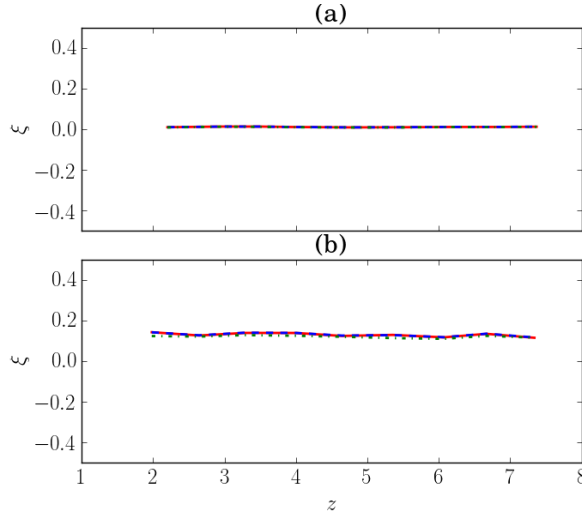
Figure IV.6: Comparison of external mass transfer coefficient for different Da. Red color corresponds to $Da = 40$, blue color corresponds to $Da = 200$ and green color corresponds to $Da = \infty$. The dimensionless parameters are fixed to : a) $Re = 50$, $Sc = 10$, $\alpha_s = 0.1$, and $\gamma = 0.1$. b) $Re = 10$, $Sc = 10$, $\alpha_s = 0.3$, and $\gamma = 0.1$.

Now, the mean volume concentration profile along z in the bed, can be deduced from (IV.8) and (IV.16) as:

$$\overline{C_v} = \overline{C}(z)\delta\sigma = \frac{3\overline{C}(z)}{1 + \frac{2\gamma}{Sh}\left(\frac{\phi/2}{tanh(\phi/2)} - 1\right)}\left(\frac{2}{\phi tanh(\phi/2)} - \frac{4}{\phi^2}\right) \tag{IV.22}$$

with σ writes as follows :

$$\sigma = 3\left(\frac{2}{\phi tanh(\phi/2)} - \frac{4}{\phi^2}\right) \tag{IV.23}$$

Thus, the cup-mixing concentration profile, the mean surface concentration and the mean volume concentration are prescribed in the bed along z by (IV.20), (IV.16) and (IV.22), respectively. The total transfer in the bed, can be accounted for through the 'reactive' Sherwood number :

$$\widetilde{Sh} = Sh\frac{\overline{C}(z) - \overline{C}_s(z)}{\overline{C}(z) - \overline{C}_v(z)} = Sh\frac{\Delta\overline{C}_s(z)}{\Delta\overline{C}_v(z)} \tag{IV.24}$$

The model proposed in (IV.24) can be compared to direct numerical simulations. The model is supposed to predict the concentration profiles along the bed, and

consequently the concentration differences $\Delta\overline{C_s}(z) = \overline{C}(z) - \overline{C_s}(z)$ and $\Delta\overline{C_v}(z) = \overline{C}(z) - \overline{C_v}(z)$. (IV.24) can be simplified to:

$$\widetilde{Sh} = \frac{\overline{C}(z) - \overline{C_s}(z)}{\overline{C}(z) - \overline{C_v}(z)} Sh = \frac{\left(1 - \delta\right)}{\left(1 - \delta\sigma\right)} Sh = \lambda Sh \qquad \text{(IV.25)}$$

The constant λ depends on the diffusion coefficient ratio γ, the reaction rate (Da) and the external Sherwood number that depends on Sc, Re and α_s. We calculate λ numerically to verify if it is constant along z. λ shows to be constant and it attains higher value at higher Da. Note that when $Da \to \infty$, $\lambda \to 1$ and $\widetilde{Sh} \to Sh$.
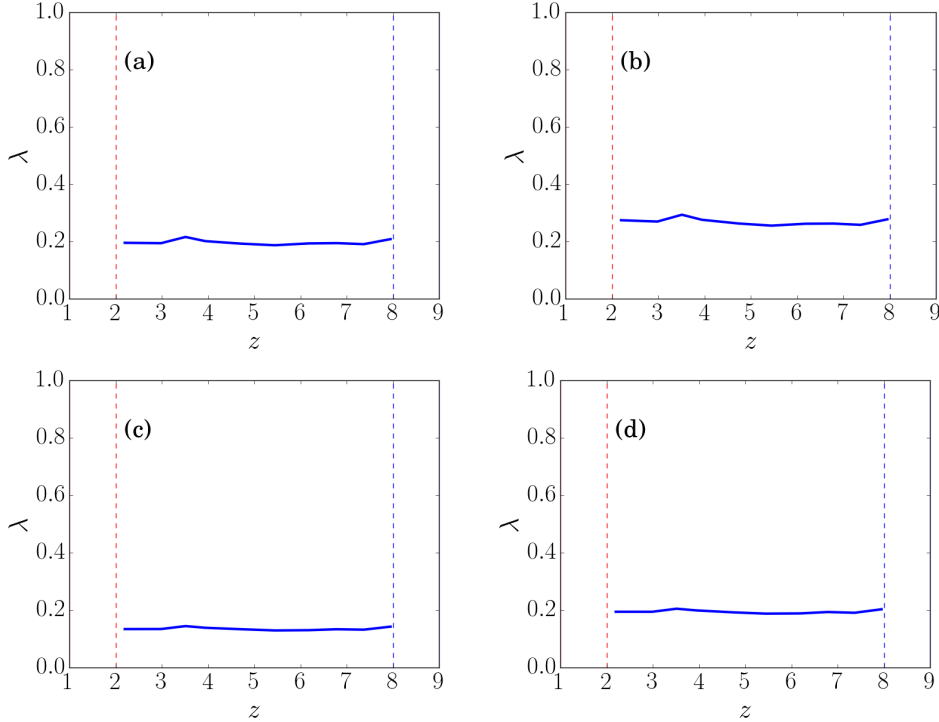
Figure IV.7: Evolution of the λ factor. At top figures (a and b) correspond to $Sc = 1$ and bottom figures (c and d) correspond to $Sc = 10$. Left figures (a and c) correspond to $Da = 40$ and right figures (b and d) correspond to $Da = 200$. Here the dimensionless parameters are fixed to $\alpha_s = 0.1$, $Re = 50$, and $\gamma = 0.1$.

4 Model validation and discussion

We perform DLM/FD-SIM numerical simulations to validate the model we proposed. We choose a spatial numerical resolution of $Nx = 40$ points per particle diameter, according to the convergence tests performed in [Sulaiman et al., 2018b]. For $\gamma = 0.1$, the numerical error on the surface concentration for the highest Da is less than 5%. All simulations were carried out with a CFL < 0.25 and they are fully converged in time. We test the model validity and dependence on the 5 dimensionless parameters in the following ranges:

— $\alpha_s \in [0.1, 0.5]$

— $\mathcal{R}e \in [1, 50]$

— $Sc \in [1, 10]$

— $Da \in [40, \infty]$

— $\gamma \in [10^{-2}, 10]$

For particle volume concentration, we consider three values $\alpha_s = 0.1$, $\alpha_s = 0.3$ and $\alpha_s = 0.5$, i.e, From semi-dilute to dense regime. We consider the following set of test cases for validation:

— Case A , we fix $\gamma = 0.1$, $\alpha_s = 0.1$, $Sc = 1$ and $Re = 1$. We vary Da such that $Da = [40, 200]$.

— Case B , we fix $\gamma = 0.1$, $\alpha_s = 0.1$, $Sc = 10$ and $Re = 1$. We vary Da such that $Da = [40, 200]$. Results comparison is shown in FIG. IV.8.

— Case C , we fix $\gamma = 0.1$, $\alpha_s = 0.1$, $Sc = 1$ and $Re = 10$. We vary Da such that $Da = [40, 200]$.

— Case D , we fix $\gamma = 0.1$, $\alpha_s = 0.1$, $Sc = 10$ and $Re = 10$. We vary Da such that $Da = [40, 200]$. Results comparison is shown in FIG. IV.9.

— Case E , we fix $\gamma = 0.1$, $\alpha_s = 0.1$, $Sc = 1$ and $Re = 50$. We vary Da such that $Da = [40, 200]$.

— Case F , we fix $\gamma = 0.1$, $\alpha_s = 0.1$, $Sc = 10$ and $Re = 50$. We vary Da such that $Da = [40, 200]$. Results comparison is shown in FIG. IV.10.

— Case H , we fix $\gamma = 0.1$, $\alpha_s = 0.3$, $Sc = 1$ and $Re = 10$. We vary Da such that $Da = [40, 200]$.

— Case I , we fix $\gamma = 0.1$, $\alpha_s = 0.3$, $Sc = 10$ and $Re = 10$. We vary Da such that $Da = [40, 200]$. Results comparison is shown in FIG. IV.11.

— Case J , we fix $\gamma = 0.1$, $\alpha_s = 0.5$, $Sc = 1$ and $Re = 1$. We vary Da such that $Da = [40, 200]$.

— Case K , we fix $\gamma = 0.1$, $\alpha_s = 0.5$, $Sc = 10$ and $Re = 1$. We vary Da such that $Da = [40, 200]$. Results comparison is shown in FIG. IV.12.

— Case L , we fix $\gamma = 0.1$, $\alpha_s = 0.5$, $Sc = 1$ and $Re = 10$. We vary Da such that $Da = [40, 200]$.

— Case M , we fix $\gamma = 0.1$, $\alpha_s = 0.5$, $Sc = 5$ and $Re = 10$. We vary Da such that $Da = [40, 200]$. Results comparison is shown in FIG. IV.13.

— Case N , we fix $\gamma = 0.1$, $\alpha_s = 0.5$, $Sc = 1$ and $Re = 25$. We vary Da such that $Da = [40, 200]$.

— Case O , we fix $\gamma = 0.1$, $\alpha_s = 0.5$, $Sc = 10$ and $Re = 25$. We vary Da such that $Da = [40, 200]$. Results comparison is shown in FIG. IV.14.

— Case P , we fix $\alpha_s = 0.1$, $Sc = 10$, $Re = 50$ and $Da = 200$. We vary γ such that $\gamma = [10^{-2}, 10^{-1}, 1, 10]$. Results comparison is shown in FIG. IV.15.

Part IV. Mass transfer coupled with chemical reaction through a random array of fixed particles in a fluid flow

— Case A , we fix $\gamma = 0.1$, $\alpha_s = 0.1$, $Sc = 1$ and $Re = 1$. We vary Da such that $Da = [40, 200]$.

— Case B , we fix $\gamma = 0.1$, $\alpha_s = 0.1$, $Sc = 10$ and $Re = 1$. We vary Da such that $Da = [40, 200]$. Results comparison is shown in FIG. IV.8.

In case A, we compare the models for the concentration profiles $\overline{C}(z)$, $\overline{C}_s(z)$, and $\overline{C}_v(z)$, corresponding to (IV.20), (IV.16) and (IV.22), respectively, at low Re, low α_s and low Sc. We only vary Da. Then, in case B, the value of Sc is increased from 1 to 10, with respect to case A, which leads to higher Peclet number. The comparison is shown in FIG. IV.8 for the two cases. The model compares well with numerical simulations with a lower agreement when $Sc = 10$ and $Da = 200$, corresponding to thin external and internal boundary layers.

Figure IV.8: Comparison with numerical simulations for $\alpha_s = 0.1$, $Re = 1$, and $\gamma = 0.1$. Red color corresponds to $\overline{C}(z)$, blue color correspond to $\overline{C}_s(z)$ and green color corresponds to $\overline{C}_v$. Continuous lines stand for simulations and markers stand for model. (a) and (b) correspond to $Sc = 1$, (c) and (d) correspond to $Sc = 10$, (a) and (c) correspond to $Da = 40$ and (b) and (d) correspond to $Da = 200$.

— Case C , we fix $\gamma = 0.1$, $\alpha_s = 0.1$, $Sc = 1$ and $Re = 10$. We vary Da such that $Da = [40, 200]$.

— Case D , we fix $\gamma = 0.1$, $\alpha_s = 0.1$, $Sc = 10$ and $Re = 10$. We vary Da such that $Da = [40, 200]$. Results comparison is shown in FIG. IV.9.

In cases C and D, and with respect to cases A and B, we only increase the value of Re from 1 to 10. The comparison is shown in FIG. IV.9. The results show a

very good agreement between the model and simulations. Concentration profiles decrease with a lower slope along the bed. This is due to the increase of convective effects induced by an increase of Re.

Figure IV.9: Comparison with numerical simulations for $\alpha_s = 0.1$, $Re = 10$, and $\gamma = 0.1$. Red color corresponds to $\overline{C}(z)$, blue color correspond to $\overline{C}_s(z)$ and green color corresponds to $\overline{C}_v$. Continuous lines stand for simulations and markers stand for model. (a) and (b) correspond to $Sc = 1$, (c) and (d) correspond to $Sc = 10$, (a) and (c) correspond to $Da = 40$ and (b) and (d) correspond to $Da = 200$.

— Case E , we fix $\gamma = 0.1$, $\alpha_s = 0.1$, $Sc = 1$ and $Re = 50$. We vary Da such that $Da = [40, 200]$.

— Case F , we fix $\gamma = 0.1$, $\alpha_s = 0.1$, $Sc = 10$ and $Re = 50$. We vary Da such that $Da = [40, 200]$. Results comparison is shown in FIG. IV.10.

In cases E and F, and with respect to cases C and D, we only increase the value of Re from 10 to 50. The comparison is shown in FIG. IV.10. The results show a very good agreement between model and simulations. Concentration profiles decrease with a lower slope along the bed than cases A,B,C and D. This is due to the increase of convective effects induced by the increase of Re at constant reaction rate and constant solid volume fraction.
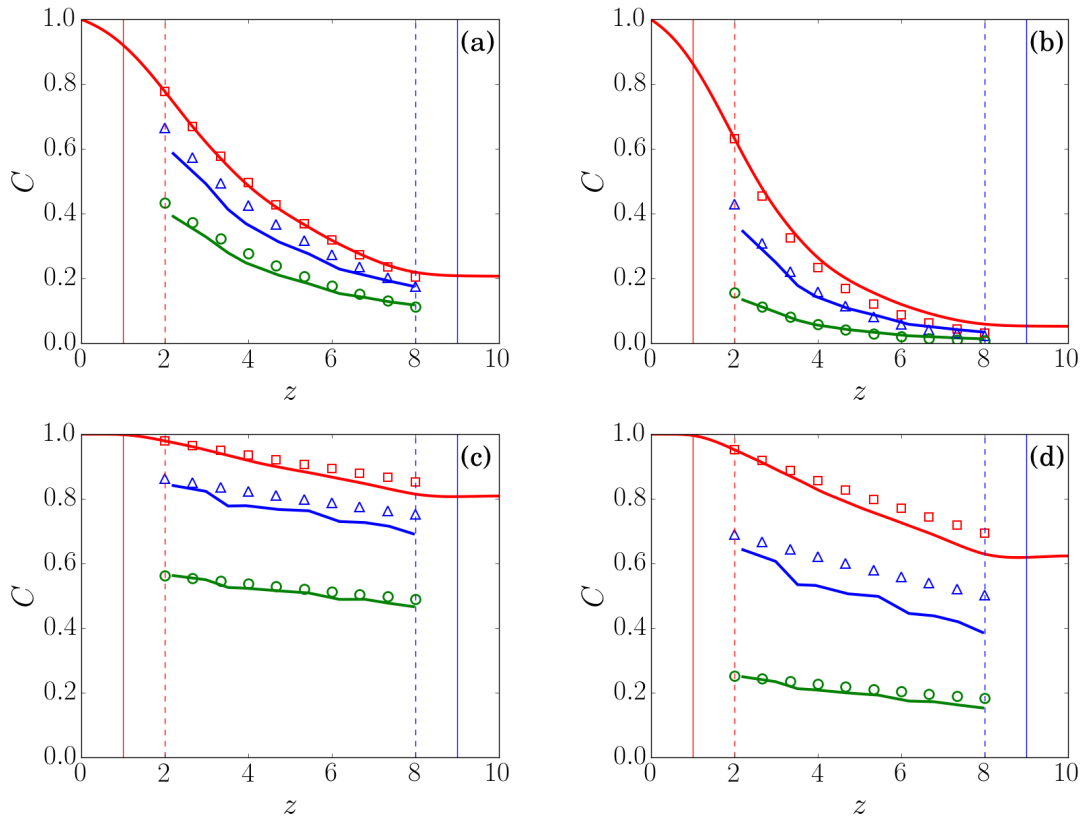
Figure IV.10: Comparison with numerical simulations for $\alpha_s = 0.1$, $Re = 50$, and $\gamma = 0.1$. Red color corresponds to $\overline{C}(z)$, blue color correspond to $\overline{C}_s(z)$ and green color corresponds to $\overline{C}_v$. Continuous lines stand for simulations and markers stand for model. (a) and (b) correspond to $Sc = 1$, (c) and (d) correspond to $Sc = 10$, (a) and (c) correspond to $Da = 40$ and (b) and (d) correspond to $Da = 200$.

— Case H , we fix $\gamma = 0.1$, $\alpha_s = 0.3$, $Sc = 1$ and $Re = 10$. We vary Da such that $Da = [40, 200]$.

— Case I , we fix $\gamma = 0.1$, $\alpha_s = 0.3$, $Sc = 10$ and $Re = 10$. We vary Da such that $Da = [40, 200]$. Results comparison is shown in FIG. IV.11.

In cases H and I, and with respect to cases C and D, we only increase the solid volume fraction α_s from 0.1 to 0.3. The comparison is shown in FIG. IV.11. The results show a good agreement between model and simulations for $Sc = 1$, whereas the agreement gets better for $Sc = 10$. The physical explanation of this observation is that when the convective effects increase, the particle surface concentration gets more uniform, and so, the assumption made in (IV.17) is more valid. Indeed, for some particles in the bed, neighbor particles induce heterogeneity to its surrounding concentration field. The increase of Re or Sc (or Pe) enhances the uniformity of the concentration field. Assuming $Pe \to \infty$, the concentration field around the particle will be uniform and equal to the inlet concentration C_∞. Concentration profiles decrease with a lower slope along the bed than the cases C and D. This is due to the increase of number of particles per volume of reactor and consequently the total surface area available for chemical reaction in the system that induces more consumption of the chemical species.

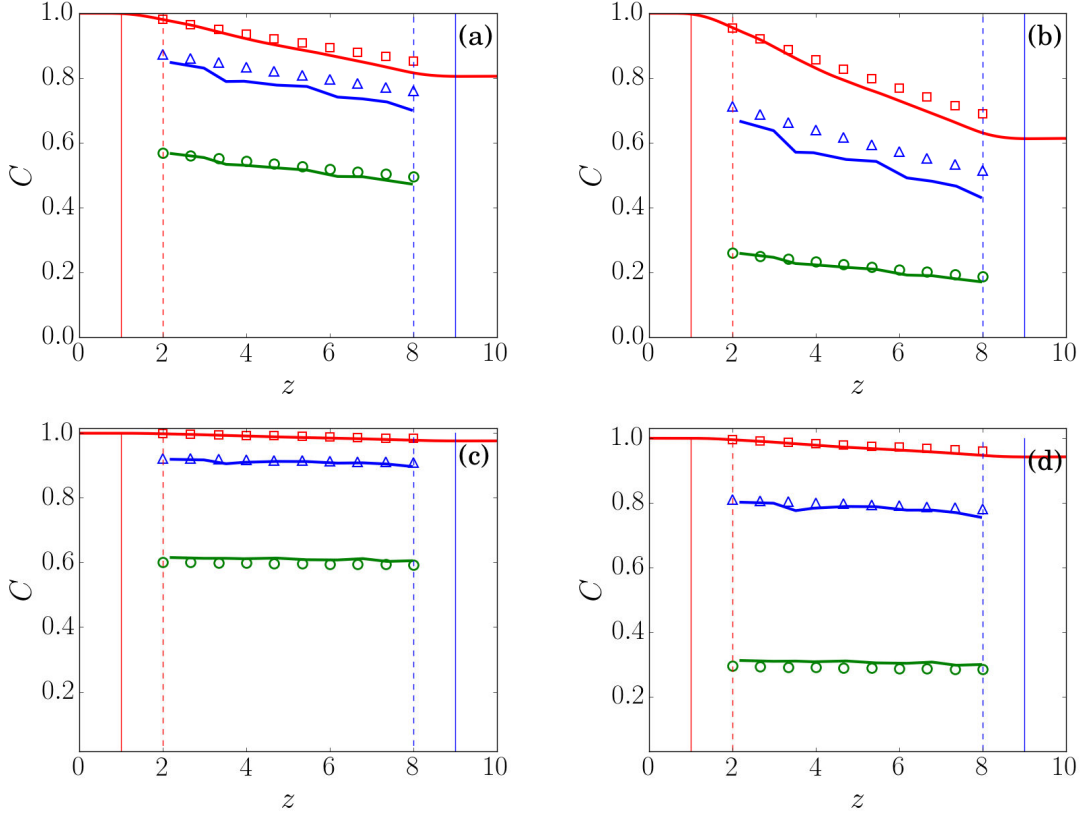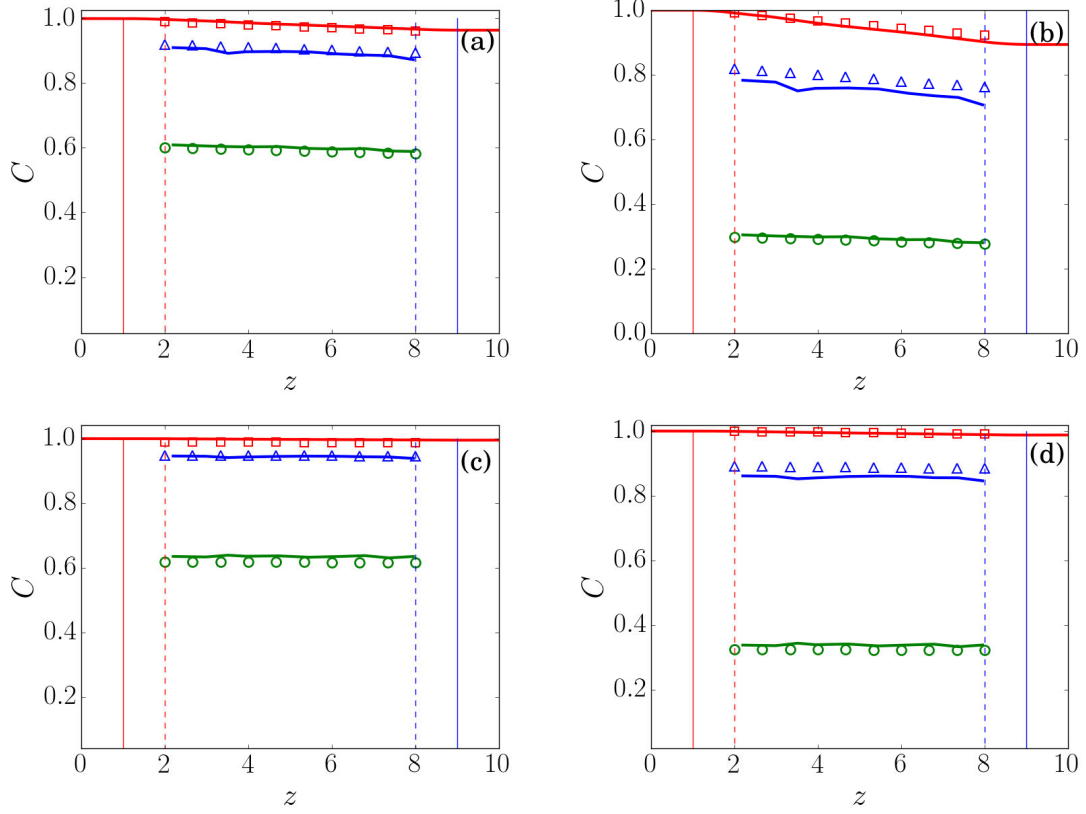**Figure IV.11:** Model comparison with numerical simulations for $\alpha_s = 0.3$, $Re = 10$, and $\gamma = 0.1$. Red color corresponds to $\overline{C}(z)$, blue color correspond to $\overline{C}_s(z)$ and green color corresponds to $\overline{C}_v$. Continuous lines stand for simulations and markers stand for model. (a) and (b) correspond to $Sc = 1$, (c) and (d) correspond to $Sc = 10$, (a) and (c) correspond to $Da = 40$ and (b) and (d) correspond to $Da = 200$.

— Case J , we fix $\gamma = 0.1$, $\alpha_s = 0.5$, $Sc = 1$ and $Re = 1$. We vary Da such that $Da = [40, 200]$.

— Case K , we fix $\gamma = 0.1$, $\alpha_s = 0.5$, $Sc = 10$ and $Re = 1$. We vary Da such that $Da = [40, 200]$. Results comparison is shown in FIG. IV.12.

In cases J and K, and with respect to cases A and B, we only increase the solid volume fraction α_s from 0.1 to 0.5. The comparison is shown in FIG. IV.12. The results show a satisfactory agreement between model and simulations for both cases $Sc = 1$ and $Sc = 10$. However, model predictions are better for cases A and B. When solid volume fraction increases, the particle surface concentration gets less uniform because the surrounding concentration field is more heterogeneous. When more neighboring particles are present, the concentration field is strongly disturbed, and so, the assumption made in (IV.17) is less and less valid. Concentration profiles show a steeper slope along the bed than the cases A and B. This is due to the increase of number of particles and consequently an increase of the consumption rate of the solute.
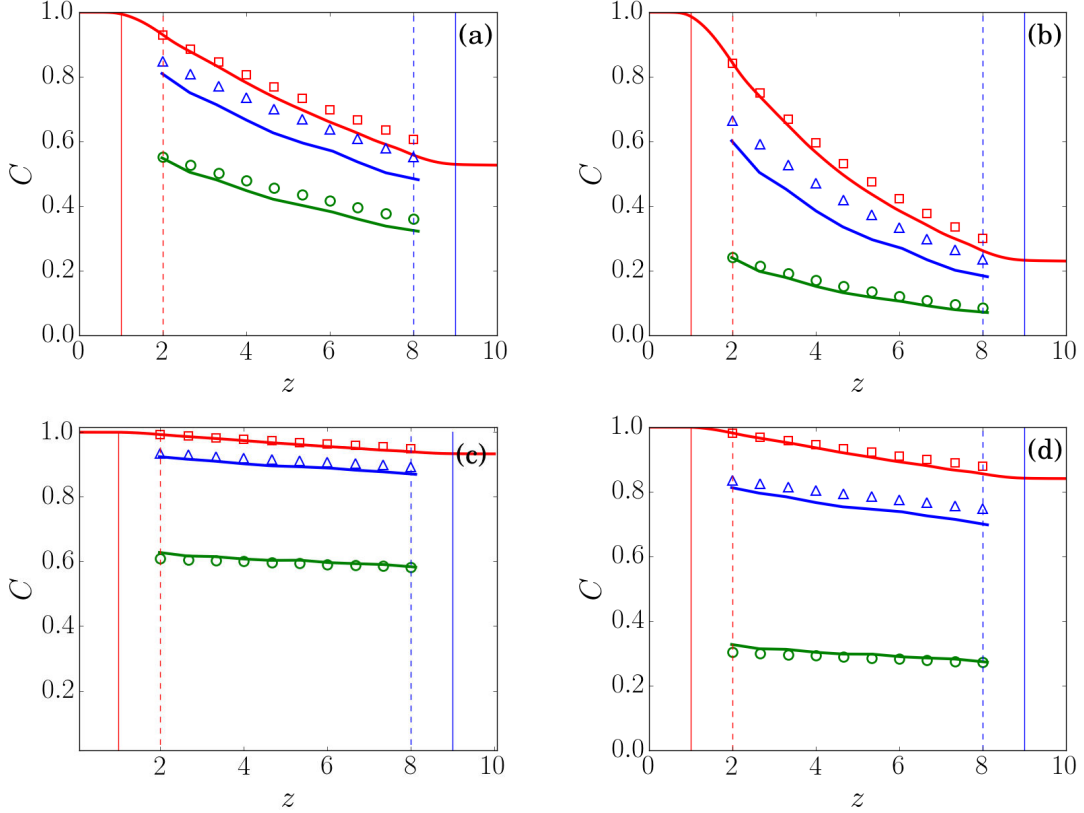
Figure IV.12: Comparison with numerical simulations for $\alpha_s = 0.5$, $Re = 1$, and $\gamma = 0.1$. Red color corresponds to $\overline{C}(z)$, blue color correspond to $\overline{C}_s(z)$ and green color corresponds to $\overline{C}_v$. Continuous lines stand for simulations and markers stand for model. (a) and (b) correspond to $Sc = 1$, (c) and (d) correspond to $Sc = 10$, (a) and (c) correspond to $Da = 40$ and (b) and (d) correspond to $Da = 200$.

— Case L , we fix $\gamma = 0.1$, $\alpha_s = 0.5$, $Sc = 1$ and $Re = 10$. We vary Da such that $Da = [40, 200]$.

— Case M , we fix $\gamma = 0.1$, $\alpha_s = 0.5$, $Sc = 5$ and $Re = 10$. We vary Da such that $Da = [40, 200]$. Results comparison is shown in FIG. IV.13.

In cases L and M, and with respect to cases J and K, we only increase Re from 1 to 10, with a single difference, Sc is 5 in case M instead of 10. The comparison is shown in FIG. IV.13. The results show a good agreement between model and simulations for both cases $Sc = 1$ and $Sc = 5$. However, model predictions are better than in the cases J and K. At a constant solid volume fraction, the particles' surface concentration gets more uniform when the convective effects increase. The increase of the convective effects enhances the homogeneity of surrounding concentration field and decreases the disturbance induced by neighboring particles. Hence, the assumption made in (IV.17) is more valid. Concentration profiles have a lower slope along the bed than the cases J and K. This is due to the increase of convective supply of chemical species to the particles surface at a constant consumption rate.
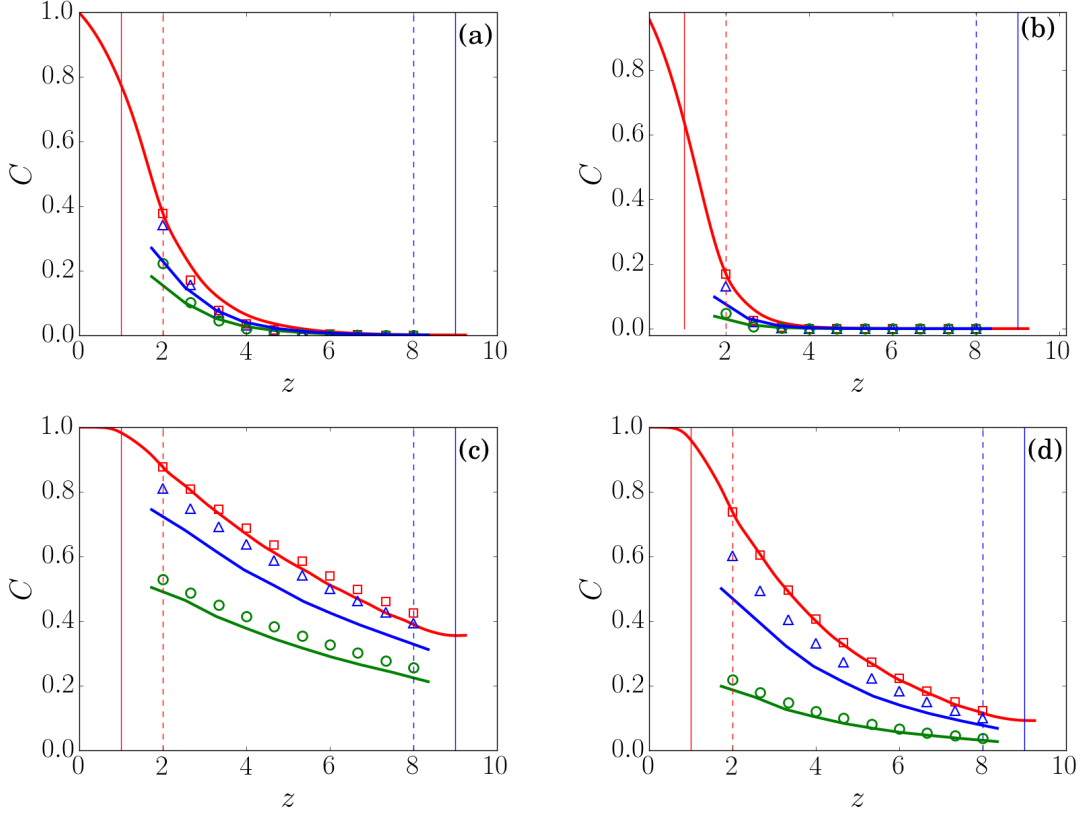
Figure IV.13: Comparison with numerical simulations for $\alpha_s = 0.5$, $Re = 10$, and $\gamma = 0.1$. Red color corresponds to $\overline{C}(z)$, blue color correspond to $\overline{C}_s(z)$ and green color corresponds to $\overline{C}_v$. Continuous lines stand for simulations and markers stand for model. (a) and (b) correspond to $Sc = 1$, (c) and (d) correspond to $Sc = 5$, (a) and (c) correspond to $Da = 40$ and (b) and (d) correspond to $Da = 200$.

— Case N , we fix $\gamma = 0.1$, $\alpha_s = 0.5$, $Sc = 1$ and $Re = 25$. We vary Da such that $Da = [40, 200]$.

— Case O , we fix $\gamma = 0.1$, $\alpha_s = 0.5$, $Sc = 10$ and $Re = 25$. We vary Da such that $Da = [40, 200]$. Results comparison is shown in FIG. IV.14.

In cases N and O, and with respect to cases L and M, we only increase Re from 10 to 25, with a single difference, Sc is 10 instead of 5. The comparison is shown in FIG. IV.14. The results show a good agreement between model and simulations for both cases $Sc = 1$ and $Sc = 5$. However, model predictions are almost similar for those in the cases L and M. Increasing convective effects does not show an important impact on the agreement between model and simulations. In all cases where $\alpha_s = 0.5$, the model agrees less with numerical simulations. This is, probably, due the fact that the assumptions are less valid at high solid volume fraction. Particles may experience, in this case, strong spatial concentration variations over their surfaces due the disturbance effects induced by neighboring particles. Limitation of the proposed model is expected in this case.
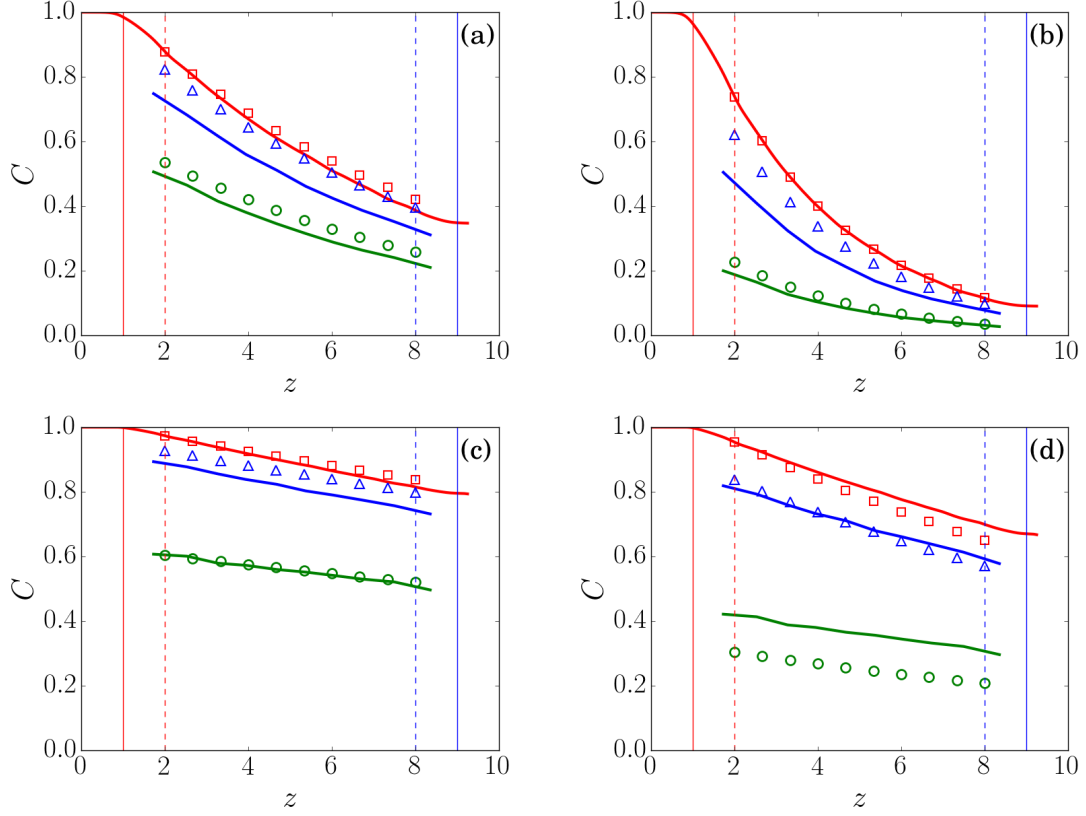
Figure IV.14: Comparison with numerical simulations for $\alpha_s = 0.5$, $Re = 25$, and $\gamma = 0.1$. Red color corresponds to $\overline{C}(z)$, blue color correspond to $\overline{C}_s(z)$ and green color corresponds to $\overline{C}_v$. Continuous lines stand for simulations and markers stand for model. (a) and (b) correspond to $Sc = 1$, (c) and (d) correspond to $Sc = 10$, (a) and (c) correspond to $Da = 40$ and (b) and (d) correspond to $Da = 200$.

— Case P , we fix $\alpha_s = 0.1$, $Sc = 10$, $Re = 50$ and $Da = 200$. We vary γ such that $\gamma = [10^{-2}, 10^{-1}, 1, 10]$. Results comparison is shown in FIG. IV.15.

Finally, in case P, we vary the diffusion coefficient ratio γ ($\gamma = 0.1$ kept constant in all the previous simulations). For this case, we fix $Re = 50$, $Da = 40$, $Sc = 10$, and $\alpha_s = 0.1$. We compare model and simulations for four values of γ : $10^{-2}, 10^{-1}, 1$, and 10. The results comparison is shown in FIG. IV.15. For $\gamma = 10^{-2}$ the model is in full agreement with simulations. The agreement stays very good when γ is increased to 10^{-1}. For $\gamma = 1$, the numerical results show a big deviation from model, the difference between model and simulations gets bigger for $\gamma = 10$. Increasing the diffusion coefficient ratio γ at a constant Da decreases the surface concentration of the particles. In fact, decreasing the bulk diffusion coefficient decreases the supply of chemical species to particles, at a constant consumption rate due to reaction. This fact is in-line with what takes place when we decrease Re or Sc. Mathematically, tending γ or ϕ to ∞ in (IV.16) has the same effect. In both cases the particle concentration tends to zero. The increase of Da increases significantly the numerical error, as the concentration gradient at the interface gets steeper, and so a higher numerical resolution is required to accurately capture the correct boundary conditions. Thus, we refer the discrepancy between the model and simulations when we increase γ to the numerical spatial resolution.
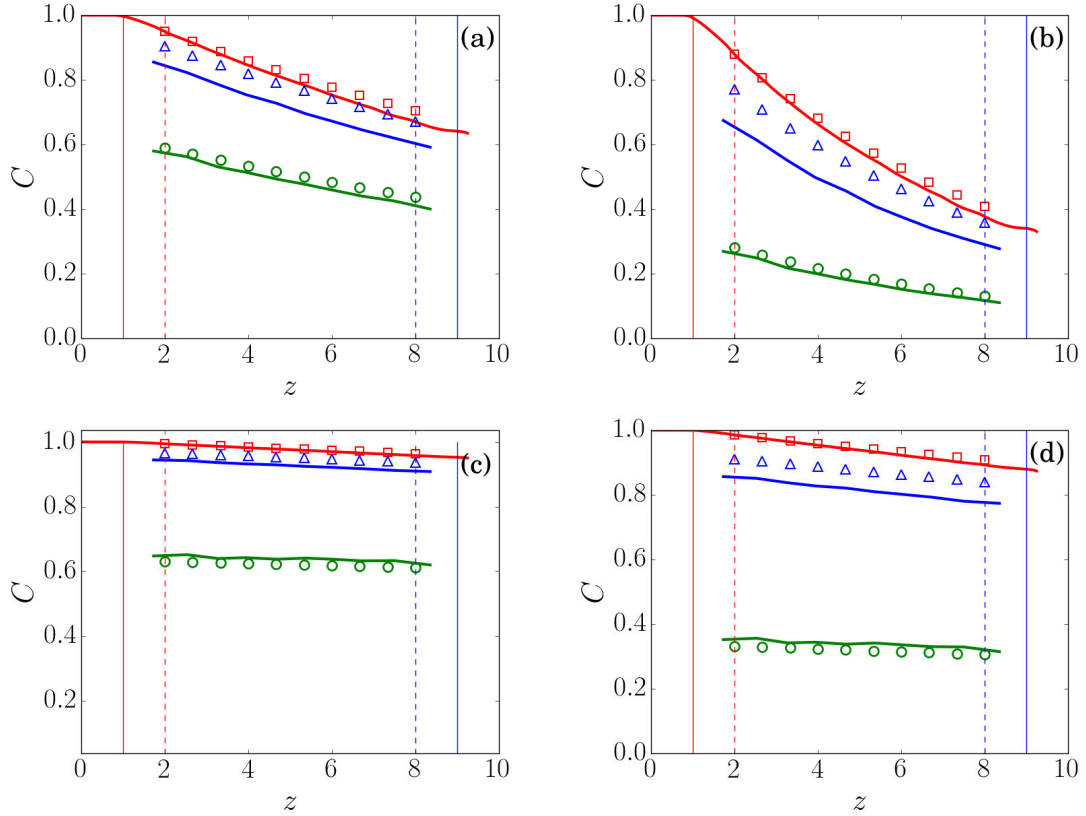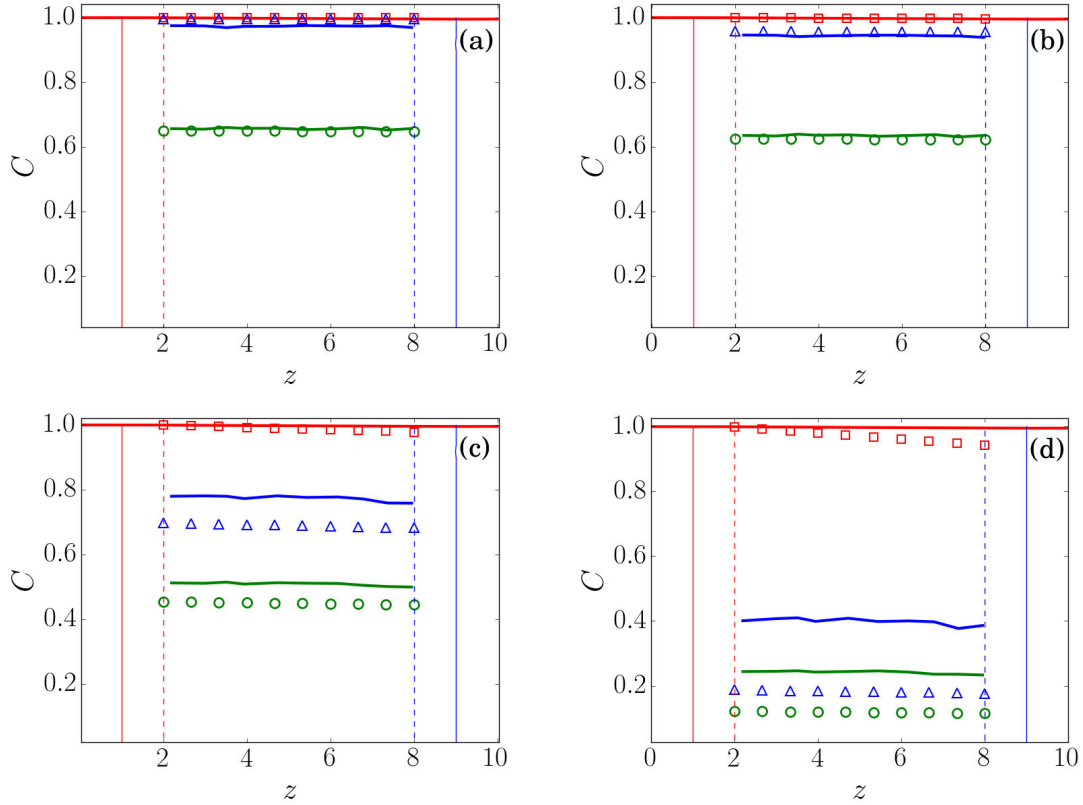
Figure IV.15: Comparison with numerical simulations for $\alpha_s = 0.1$, $Re = 50$, and $Da = 40$. Red color corresponds to $\overline{C}(z)$, blue color correspond to $\overline{C}_s(z)$ and green color corresponds to $\overline{C}_v$. Continuous lines stand for simulations and markers stand for model. (a) corresponds to $\gamma = 0.01$, (b) corresponds to $\gamma = 0.1$, (c) corresponds to $\gamma = 1$ and (d) corresponds to $\gamma = 10$.

In order to illustrate this fact, we arbitrarily select a few particles in the bed and we plot their internal concentration profiles for $\gamma = 10^{-2}$, $\gamma = 1$ and $\gamma = 10$ in FIG. IV.16. The particles location in the bed is shown in FIG. IV.15. Regardless their positions in the bed, particles show approximately a similar concentration profile for the same γ. However, when γ increases, the surface concentration significantly decreases with an increase of the gradient between the surface and bulk concentrations. This explains the increase of the numerical error and thus the model cannot be tested in this case as the simulations are not well-spatially resolved. The concentration iso-contours of the presented case are shown in FIG. IV.18. They clearly show the decrease of the particle concentration with the increase of γ. This observation is similar to what we can see in FIG. IV.17, where we compared the concentration iso-contours for another case at $Re = 25$, $\gamma = 0.1$, $Sc = 10$, $\alpha_s = 0.3$ and many Da. We show in FIG. IV.19 the concentration iso-surfaces for $\alpha_s = 0.1$, $\gamma = 0.1$ and $Sc = 1$. In (a), (b) and (c), we increase Re from 1, to 10 and 50 respectively, at a constant Da. The concentration increases with the increase of Re. As previously pointed-out, the increase of Re increases the convective effects and the supply at a constant consumption rate of the chemical species. In (c), (f), and (i), Re is fixed to 50. The reaction rate is increased through Da, from 40, to

200 and ∞. The particles concentration as well as the global concentration in the bed decrease with increase of Da. At a constant supply rate through convection and mass diffusion, the consumption of the chemical species due to reaction has been increased.
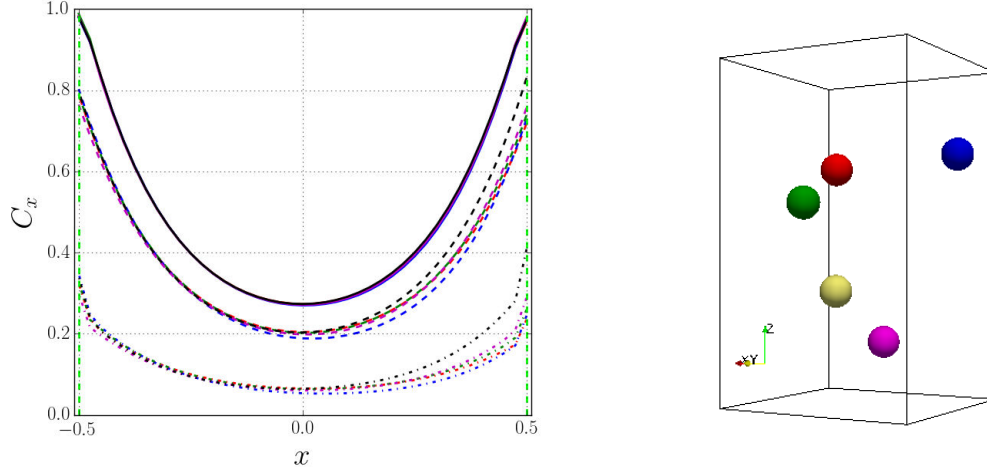
Figure IV.16: (Right) concentration profiles comparison for arbitrary selected particles in the bed (left). Vertical dashed line represents particle interface with fluid. Continuous lines correspond to $\gamma = 10^{-2}$, dashed lines correspond to $\gamma = 10^{-1}$ and dotted lines correspond to $\gamma = 10$. Red, blue, green, magenta, and black colors correspond to red, blue, green, magenta, and black spheres, receptively.

(a) (b) (c)
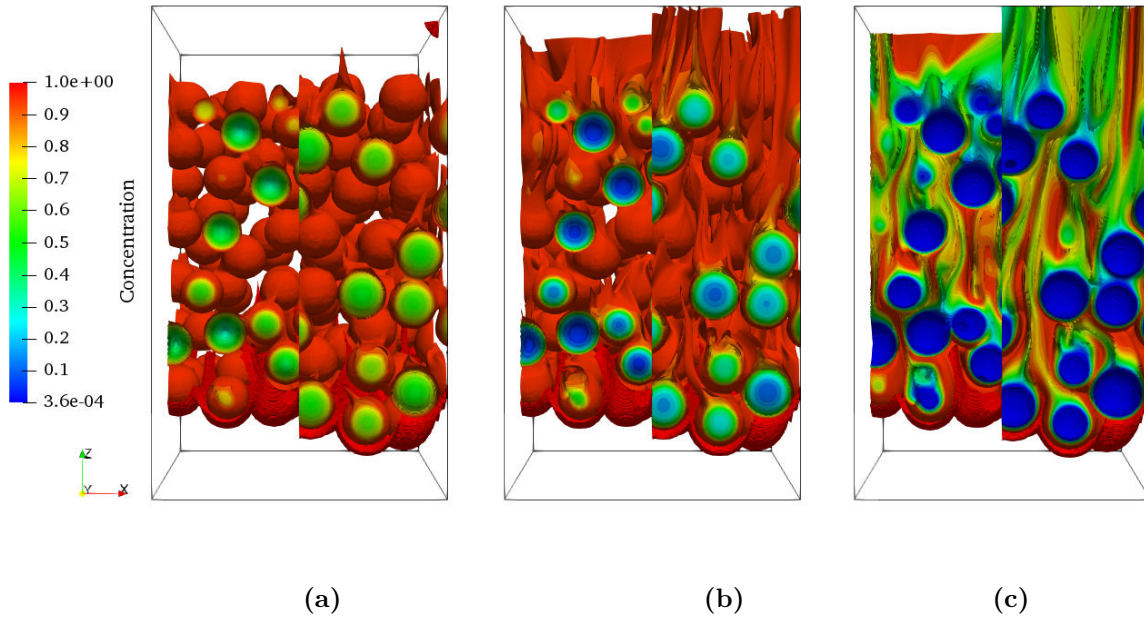
Figure IV.17: Concentration contours at $Re = 25$, $\gamma = 0.1$, $\alpha_s = 0.3$ and different Damkohler numbers. a) $Da = 40$, b) $Da = 200$ and c) $Da = \infty$

(a) $\gamma = 0.01$ (b) $\gamma = 1$ (c) $\gamma = 10$
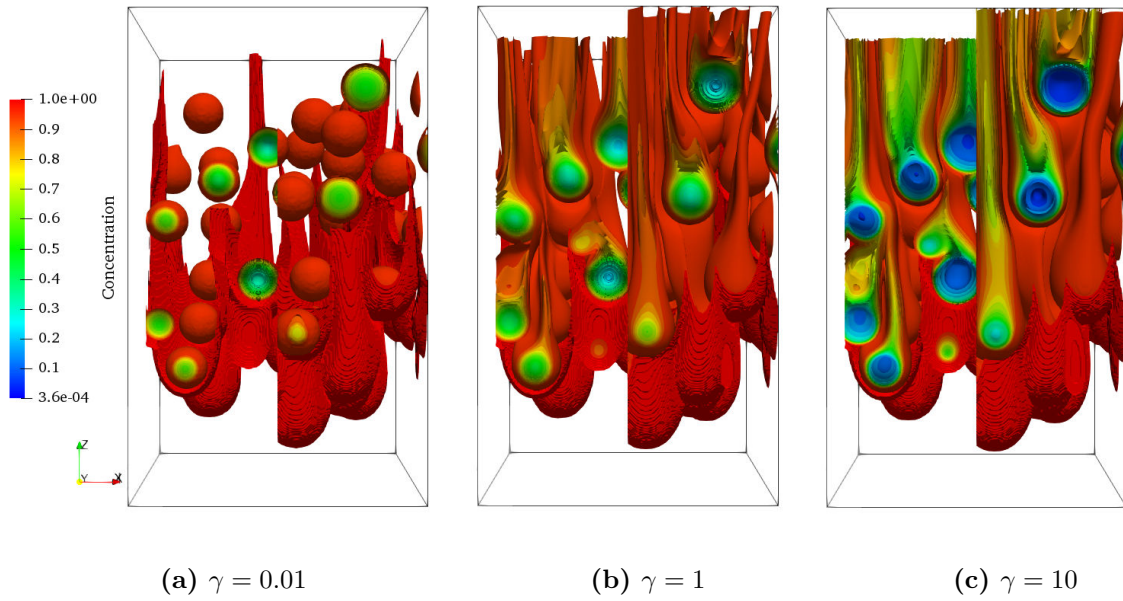
Figure IV.18: Concentration contours at $Re = 50$, $Sc = 10$, $Da = 40$, $\alpha_s = 0.1$, $\gamma = 10^{-2}, 1, 10$.
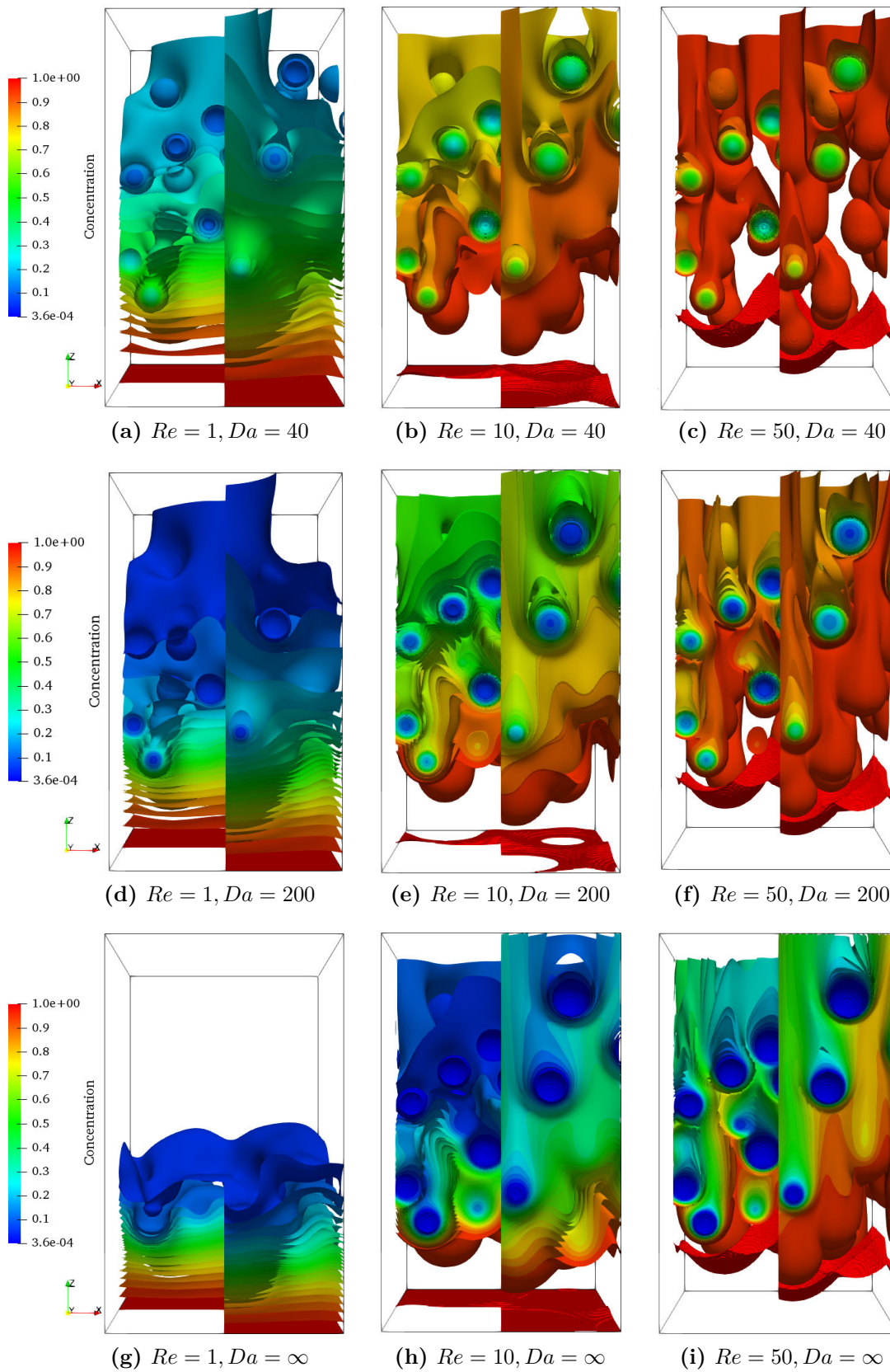
Figure IV.19: Concentration iso-surfaces for $Sc = 1$ and $\gamma = 0.1$ and $\alpha_s = 0.1$.

Reactive Sherwood number

We compare the model of reactive Sherwood number $\widetilde{Sh}$ presented in (IV.25) with numerical simulations for two cases $\alpha_s = 0.1$ and $\alpha_s = 0.5$. For each case we consider $Da = 40$, $Da = 200$ and $Da = \infty$. For the first dilute case, the results are shown in FIG. IV.20. In the first case, the model compares well with numerical simulations. For the second dense case, model compares worse than the first case with numerical simulations. This difference is expected as for $\alpha_s = 0.5$, the model showed some discrepancies for the prediction of the mean surface and volume concentration profiles.

(a) $\alpha_s = 0.1$ **(b)** $\alpha_s = 0.5$
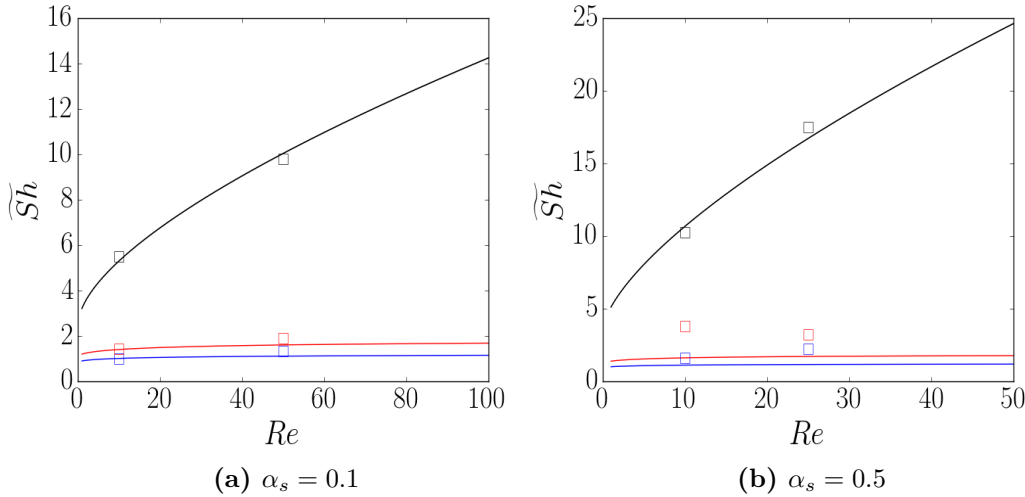
Figure IV.20: Model comparison with numerical simulations for $Sc = 10$. (a) corresponds to $\alpha_s = 0.1$, and (b) corresponds to $\alpha_s = 0.5$. Blue color corresponds to $Da = 40$, red color corresponds to $Da = 200$ and black color corresponds to $Da = \infty$. Continuous lines represent simulations and markers represent model.

5 Conclusion

The effect of a first order irreversible chemical reaction within a network of catalyst particles has been studied. The cup-mixing concentration as well as the means surface and mean volume concentration profiles have been obtained from simulations and the concentration gradients between bulk, particle surface and particle volume have been compared to our model. The results of the model have been compared to direct numerical simulations and according to its behavior the following conclusions are drawn :

— At constant Re, Sc, Da, and γ, the lower the solid volume fraction, the better the agreement between model and numerical simulations.

— At constant α_s, Da and γ, the higher the $Pe = Re \times Sc$, the better the agreement between model and numerical simulations.

The validity of the model showed to be highly affected by the spatial homogeneity of the surrounding concentration field. At a low solid volume fraction, the flow

field tends to that around an isolated particle, and thus the assumptions are likely to be valid. At the same low solid volume fraction, as Pe increases, the more the system becomes similar to that of isolated particles and bulk concentration tends to be equal to inlet concentration. This is due to the fact that convective effects increase at a constant consumption rate of the chemical reaction.

At a constant Pe, when solid volume fraction increases, the heterogeneity in the system becomes prominent, and the concentration field surrounding a particle is disturbed. The disturbance of the concentration field affects directly the concentration profiles inside the particle as well as its mean surface and volume concentrations. Even at a high solid volume fraction, when Re increases, the chemical species supply to the system increases at a constant consumption rate due to reaction. Assuming a strong flow rate, particles in the system will experience a uniform concentration field that has a value equal to that of inlet concentration, and the model prediction is supposed to behave similarly to that of single isolated particle. The limitation of the model can probably be further treated mathematically by taking in account the effect of disturbance induced by neighbor particles, through creating kernels that are capable of predicting the correct mean surface and volume concentrations of the particles even at a high solid volume fraction.

Part V

Conclusion and perspectives

Contents

1   Conclusion

The carried out work aimed at investigating the effect of a first order irreversible chemical reaction on mass transfer for systems composed of two phases. Dispersed phase consists in fixed catalyst particles and continuous phase is a fluid through which chemical species get transported by mass, momentum diffusion and convection. Chemical species diffuse from fluid to solid particles where diffusion and reaction take place. The problem is handled by means of external-internal coupling by virtue of flux and concentration continuities as boundary conditions at particle interface. The performed coupling depends on the decoupling of the external and internal Sherwood numbers, where the external mass transfer coefficient is evaluated through the external-known Sherwood number that is considered to be independent of reaction rate, which is the milestone of our modeling strategy.

In the first part, we started with the simplest system that has not been yet addressed in literature, the system of a single particle in a forced convective-diffusive fluid stream where a first order irreversible reaction is taking place along with diffusion all over the particle volume. In such a system, the internal Sherwood number is dependent on reaction rate that significantly affects the concentration gradient between the particle surface and volume. Thus, we firstly aimed at determining the mean surface concentration of the particle through which the mean volume concentration can be deduced thanks to the analytical solution of the 1-D concentration profile within the catalyst particle (Thiele problem). Here we considered that the particle's surface concentration does not experience an important spatial variation, and consequently the concentration profiles inside the particle can still be predicted by the 1-D solution of the Thiele problem. We carried out a set of direct numerical simulations using a body-fitted mesh method that fully resolves the internal and external boundary layers to assess the validity of the proposed model over a wide

range of dimensionless parameters. The model showed to be capable of predicting the mean surface and mean volume concentration, although the external mass transfer coefficient in the model is evaluated through an empirical correlation available in literature, previously established in mass transfer regime (infinite reaction rate). Subsequently, an overall Sherwood number, hereafter called 'reactive' Sherwood number has been established based on general mass balance and re-obtained through additivity rule. The reactive Sherwood number compared very well with numerical simulations. The unsteady response of the model is then tested. It has shown to be able to predict the temporal evolution of the mean volume concentration of the particle.

In the second part, we aimed at the extension of the model to multi-particle systems. To do so, we implemented a Sharp Interface Method that accurately captures gradients at solid boundaries in our in-house code. The method's implementation as well as its capability and limits have been assessed by comparison with analytical solutions and existing empirical correlations in literature in cases of diffusion-reaction and convection-diffusion, respectively. In case of chemical reaction coupled with an external convection-diffusion, the method has been validated against the boundary-fitted mesh code that has been previously used in the first part. The mean surface concentration has been compared for the case of a single particle for a wide range of dimensionless parameters. Convergence tests have been performed by taking the boundary-fitted code as a reference solution to probe the limitations of the method. Concentration profiles between the boundary-fitted and Sharp Interface Method have been compared in cases of convection-diffusion-reaction and they showed a very good agreement. Before addressing a complex network of particles, we studied the problem of three aligned interacting spheres with chemical reaction. A physical model for reactive Sherwood number for each sphere has been presented. The model uses the same boundary conditions of the single particle case and the external mass transfer coefficient of each particle is evaluated through the individual-external Sherwood numbers that have been previously presented in literature for non-reactive particles. The new model has been thoroughly validated by a long set of simulations and it showed a very good agreement. The assumption of the 1-D model made in the first part of the study showed to be valid even for three particles as long as the individual-external Sherwood number is known and the value of the mean external mass transfer coefficient can be correctly predicted. The validity of this assumption, here, is essentially dependent on the fact that even in the system of three interacting spheres, the concentration field surrounding the particles stays uniform and the bulk concentration is equal to that of inlet concentration. Thus, the validity of the proposed model needs to be assessed in problems incorporating multi-particles of high solid fraction where each particle is surrounded by neighbor particles that disturb its surrounding concentration field.

In the last part, a fixed bed of particles has been studied. The system possesses three main differences with the previous two systems. The bulk concentration in this case is variable along the bed height in the main flow direction, the particles' mean surface and volume concentrations significantly vary along the bed height, and the flow field surrounding a particle is disturbed by the other neighbor par-

ticles undergoing reaction and consuming chemical species. The same coupling strategy has been adopted here. The cup-mixing concentration as well as the mean surface and mean volume concentration profiles have been predicted, and thus, the concentration gradients between bulk, particles surface and volume are predicted. The reactive Sherwood number is shown analytically to be a function of both gradients that are expressed in terms of 5 dimensionless parameters. The model has been compared to direct numerical simulations and according to its behavior the following remarks are concluded :

— At constant Re, Sc, Da, and γ, the lower the solid volume fraction, the better the agreement between model and numerical simulations.

— At constant α_s, Da and γ, the higher the $Pe = Re \times Sc$, the better the agreement between model and numerical simulations.

The validity of the model is highly affected by the uniformity of the surrounding concentration field. At a low solid volume fraction, particles behavior tends to that of an isolated particle, and thus the assumptions adopted are likely to be valid. At the same low solid volume fraction, the more Pe increases, the more the system is similar to that of isolated particles and bulk concentration tends to be equal to that of inlet concentration. This is due to the fact that convective effects are being increased at a constant consumption rate due to chemical reaction.

At a constant Pe, the more the solid volume fraction increases, the more the heterogeneity in the system is prominent, and the more the concentration field surrounding a particle is disturbed. The disturbance of the concentration field affects directly the concentration profiles inside the particle as well as its mean surface and volume concentrations. Even at a high solid volume fraction, when Re increases, the chemical species transport to the system increases at a constant consumption rate due to reaction. The more Re increases, the more the concentration field is uniform and the more the assumption is valid. Assuming an infinite flow rate, particles in the system will experience a uniform concentration field that has a value equal to that of inlet concentration, and the model prediction is supposed to behave as that of single isolated particle.

2 Perspectives

The model showed limitations at high solid volume fraction, when convective effects are low and concentration field is disturbed. This limitation of the model is to be probably further treated mathematically by taking in account the effect of disturbance induced by neighbor particles, through predicting the correct mean surface and volume concentrations of the particles.

The objective of the established models is twofold. i) A tool that can be used by engineers for quick estimation of mass transfer coefficients in reactor design and ii)

as a closure law for partially resolved numerical models (DEM-CFD) where information about local interactions at particle scale is unresolved. It is of major interest to assess the validity of the established model as a closure law these systems and to perform a comparison between fully resolved simulations (DNS-micro scale) and partially resolved simulations (DEM-meso scale).

The carried out work addressed systems involving spherical particles. Catalyst particles' shapes vary in industrial applications from spherical to convex and non-convex shapes. Modeling efforts in future work are to be devoted towards the comprehension of systems composed of complex particles shapes, analytically, and numerically. The numerical validation of the analytical models would require the extension of the implemented Sharp Interface Method to non-spherical particles to be able to simulate systems comprising complex shapes. Creating correlations would allow engineers to attain efficient tools to estimate mass transfer coefficient and help them to optimize their reactor design. As a closure law, these models would allow to simulate meso scale systems that comprise big number of particles.

Part VI

Appendixes

1 The granular flow solver : Grains3D

The discrete numerical methods simulating the individual grain movement are important tools to study the behavior of granular flows. These methods permit to numerically access some variables which are difficult to access experimentally, such as the forces exerted on grains, their contact distribution and the stress and deformation tensors. In spite of the ever increasing computational capacity, these methods are still costly and they are facing problems when the number of particles is large. The Discrete Element Method (DEM), firstly presented by Cundall and Strack Cundall and Strack [1979], has been widely used to simulate granular flows. Due to its success and simplicity through treating complex granular mechanisms, DEM simulates particle-particle interactions at particle scale, which permits to track the particles motion and their packing as a whole. The method has been successfully used examine various granular problems such as rotating drum, vibrating screen, mixing process, screw conveyor. DEM is implemented in our platform and was used to simulate granular spherical particles, non-spherical convex particles and non-spherical and non-convex particle [Wachs et al., 2012], [Rakotonirina and Wachs, 2018] and [Rakotonirina et al., 2018].

— Governing equations:

The particles motion is calculated by applying Newton's second law to each particle i, $i \in [0, N-1]$ where N is the total number of particles. The velocity vector $\boldsymbol{\nu}$ of a rigid particle can be expressed as the sum of translational and rotational terms, $\boldsymbol{\nu} = \mathbf{U} + \boldsymbol{\omega} \wedge \mathbf{R}$. Where $\boldsymbol{U}$, $\boldsymbol{\omega}$ and $\boldsymbol{R}$ represent the particle's translational velocity, angular velocity and the position vector, respectively. The translational motion of a particle of index i is represented by eq(VI.1) whereas the rotational motion is expressed by eq(VI.2).

$$M_i \frac{d\mathbf{U}}{dt} = \mathbf{F}_i \quad \text{(VI.1)} \qquad \qquad \boldsymbol{J}_i \frac{d\boldsymbol{\omega}_i}{dt} + \boldsymbol{\omega}_i \wedge \boldsymbol{J}_i \boldsymbol{\omega}_i = \boldsymbol{M}_i \quad \text{(VI.2)}$$

Where M_i, $\boldsymbol{\omega}_i$, $\boldsymbol{J}_i$, $\boldsymbol{F}_i$, $\boldsymbol{M}_i$ are the particle's mass, angular velocity, inertia tensor, sum of all forces, and sum of torques applied on particle i, respectively.

The linear position x_i and angular position θ_i are obtained by integrating the two classical kinematics equations (VI.3) and (VI.4), respectively.

$$\frac{d\mathbf{x_i}}{dt} = \mathbf{U}_i \quad \text{(VI.3)}$$

$$\frac{d\boldsymbol{\theta}_i}{dt} = \boldsymbol{\omega}_i \quad \text{(VI.4)}$$

Only contact forces and gravity are acting on the particle. Thus, the $\boldsymbol{F}_i$ and $\boldsymbol{M}_i$ can be written as eq(VI.5) and eq(VI.6) respectively:

$$\boldsymbol{F}_i = M_i\boldsymbol{g} + \sum_{j=0,j\neq i}^{N-1} \boldsymbol{F}_{ij} \quad \text{(VI.5)}$$

$$\boldsymbol{M}_i = \sum_{j=0,j\neq i}^{N-1} \boldsymbol{R}_j \wedge \boldsymbol{F}_{ij} \quad \text{(VI.6)}$$

Where $\boldsymbol{R}_i$ is a vector pointing from the center of mass of particle i to the contact point with particle j. The $\boldsymbol{\omega}_i \wedge \boldsymbol{J}_i\boldsymbol{\omega}_i$ term cancels out in the case of 2D systems as well as the 3D cases exhibiting some specific symmetry properties as, e.g, a sphere or a cube. Usually, this term cannot be dropped due to the fact that the inertia tensor $\boldsymbol{J}_i$ defined in a global space-fixed coordinate system varies with θ. Two coordinate systems are used to overcome this issue, the first is the global one which is independent of the particle and the second, the body-fixed to the particle, translates and rotates with it. The inertia tensor is calculated in the fixed body-fixed coordinate system which is stored as reference configuration and rotations from this reference to the current configuration provides the current tensor of inertia of the particle. For 3 dimensional arbitrary shapes, quaternions have been used to represent rotations to avoid the singularities which can be induced by Euler angles at angles 0 and π. Quaternions are non-singular under any arbitrary rotation, easy to work with, and can be renormalized in case of cumulative error. The angular displacements of the rigid particles are limited in DEM simulations over a time step due the small time step magnitude required by the explicit time integration of the governing equations and the short contact duration.

— Numerical integration:

Numerical Integration in preformed through a second-order accurate scheme is employed combining low computational cost with acceptable accuracy and low complexity. Eq(VI.1), eq(VI.2), eq(VI.3) and eq(VI.4) have been integrated using Adams-Bashforth scheme employed in Džiugys and Peters [2001] and Sundaram and Collins [1996]. Only the translational equations are detailed here, the same applies for the angular equations. The particles collision are detected with a GJK algorithm. For spherical particles, the contact of two spheres can be determined by computing the distance between the particles center of mass, if the distance is less $r_1 + r_2$, then the particles are in contact. If the distance is bigger than $r_1 + r_2$ then the particles are not in contact. The determination of contact requires defining the normal and tangent vectors at the contact point. For a sphere, the normal vector points out from the

particle's center of mass to the one of other particle which is in contact. For convex non-spherical shapes, the definition is more complex, the reader is referred to Wachs et al. [2012].

$$\boldsymbol{U}(t + \Delta t) = \boldsymbol{U}(t) + \frac{\Delta t}{2M}(3\boldsymbol{F}(t) - \boldsymbol{F}(t - \Delta t)) \qquad \text{(VI.7)}$$

$$\boldsymbol{x}(t + \Delta t) = \boldsymbol{x}(t) + \frac{\Delta t}{2}(3\boldsymbol{U}(t) - \boldsymbol{U}(t - \Delta t)) \qquad \text{(VI.8)}$$

The leap-frog Verlet scheme, eq(VI.9) and eq(VI.10), can also be employed to integrate the system of equations. It worth mentioning that in both schemes, evaluating the contact forces is required only once at each time step, which is the costly part of the method.

$$\boldsymbol{U}(t + \Delta t/2) = \boldsymbol{U}(t - \Delta t/2) + \frac{\boldsymbol{F(t)}}{M}\Delta t \qquad \text{(VI.9)}$$

$$\boldsymbol{x}(t + \Delta t) = \boldsymbol{x}(t) + \boldsymbol{U}(t + \Delta t/2)\Delta t \qquad \text{(VI.10)}$$

— Contact forces:
The chosen contact model adopts a simple classical Hook-like elastic model. The collision force is a combination of Hookean elastic restoring force, eq(VI.11), a viscous dynamic force in the normal direction to account for the dissipative aspect of the contact, eq(VI.12), where k_n is normal contact stiffness, δ_{ij} is the overlapping distance between particles i, j and $\boldsymbol{n}_c$ the unit normal vector at the contact point, γ_n is the dissipative normal friction coefficient, $m_{ij} = \frac{M_i M_j}{M_i + M_j}$ is the reduced mass of the particles i and j and $\boldsymbol{U}_{rn}$ is the normal relative velocity between them.

$$\boldsymbol{F}_{ij,dn} = -2\gamma_n m_{ij}\boldsymbol{U}_{rn} \qquad \text{(VI.12)}$$

$$\boldsymbol{F}_{ij,el} = k_n \delta_{ij}\boldsymbol{n}_c \qquad \text{(VI.11)}$$

The tangential force is expressed in eq(VI.13), and its dissipative frictional term in eq(VI.14), where the γ_t is the dissipative tangential friction coefficient, $\boldsymbol{U}_{rt}$ is the tangential relative velocity between the particles i and j and $\boldsymbol{t}_c$ is the unit tangential vector at the contact point. The tangential force is limited by the Coulomb frictional force calculated with Coulombs dynamic frictional coefficient μ_c.

$$\boldsymbol{F}_{ij,t} = min\{\mu_c|\boldsymbol{F}_{el}|, |\boldsymbol{F}_{dt}|\}\boldsymbol{t}_c \quad \text{(VI.13)} \qquad \boldsymbol{F}_{dt} = -2\gamma_n m_{ij}\boldsymbol{U}_{rt} \quad \text{(VI.14)}$$

The resultant force acting on the particle is the sum of all the tangential and normal contributions and can be written as eq(VI.15):

$$\boldsymbol{F}_{ij} = \boldsymbol{F}_{ij,el} + \boldsymbol{F}_{ij,dn} + \boldsymbol{F}_{ij,t} \quad \text{(VI.15)} \qquad \boldsymbol{M}_{rolling,ij} = -k_{ms}|\boldsymbol{F}_{ij}^{n}|R_{ij}\frac{\boldsymbol{\omega}_{ij}}{|\boldsymbol{\omega}_{ij}|} \quad \text{(VI.16)}$$

The rolling moment, eq(VI.16), is added in the case of spherical particles to the total torque of particle i during its contact with particle j, k_{ms} is the rolling friction coefficient, $\boldsymbol{F}_{ij}^{n} = \boldsymbol{F}_{ij}\boldsymbol{n}_{c}$, $R_{ij} = \frac{R_i R_j}{R_i + R_j}$ is the reduced radius, $\boldsymbol{\omega}_{ij} = \boldsymbol{\omega}_{i} - \boldsymbol{\omega}_{j}$ is the relative angular velocity.
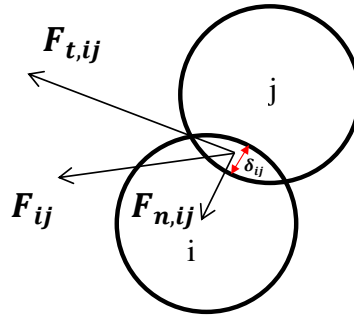
Figure VI.1: Forces acting on the contact point of particle i with particle j. δ_{ij} is the overlapping distance Džiugys and Peters [2001].

— DEM time step:
  The required time step to integrate the system of equations has to be taken less than the collision duration between two particles T_c, expressed in eq(VI.17), and can be approximated by the collision of two particles of same radius R in a zero gravity space with a relative colliding velocity v_0 using Newton's second law, see Wachs et al. [2012] and Džiugys and Peters [2001] for the governing equation. Generally, the time step is taken in the interval $[T_c/50, T_c/10]$ in order to integrate contact properly .

$$T_c = \frac{\pi}{\sqrt{\omega_0^2 - \gamma_n^2}} \quad \text{(VI.17)}$$

2   The DEM-CFD Method: Meso-Scale

Meso-scale interactions are accounted for in PeliGRIFF through a DEM-CFD model. This model lies at an intermediate level of resolution between the Particle Resolved models and the Two Fluid Model. Particle size, density and other physical properties can be taken into account. The particle-particle treatment with DEM model is detailed in *Section 1* The available computing power and algorithms enable us to simulate systems containing up to $O(10^8)$ particles, which is equivalent to a

lab-scale reactors. The fluid phase of the DEM model can be described by the locally phase-averaged equations firstly presented by Anderson and Jackson [1967], the continuity equation is written as:

$$\frac{\partial \rho \epsilon}{\partial t} + \frac{\partial}{\partial x_i}(\epsilon u_i) = 0 \tag{VI.18}$$

The fluid motion is described through :

$$\frac{\partial}{\partial t}(\epsilon u_i) + \frac{\partial}{\partial x_i}(\epsilon u_i u_j) = -\frac{\epsilon}{\rho_g}\frac{\partial p}{\partial x_i} + f_{p_f} \tag{VI.19}$$

where ρ is the density, ϵ the void fraction, p the pressure and f_{p_f} the force exerted by the particles on the fluid and it is given by the following equation:

$$f_{p_f} = \beta(v_{p_f} - u_f)/\rho \tag{VI.20}$$

β is a void fraction dependent coefficient. The particles motion is considered as weakly affected by the other particle when $\beta > 0.8$. When the void fraction is less than 0.8 , β can be found from Ergun equation for a packed bed [Tsuji et al., 1993].

$$\beta = \begin{cases} \dfrac{1-\epsilon}{d_s \epsilon^2} + \left(150\dfrac{(1-\epsilon)\mu}{d_s} + 1.75\rho\epsilon|\vec{V_s} - \vec{u}|\right) & \text{if } \epsilon \leq 0.8 \\ \dfrac{3}{4}C_D\dfrac{|\vec{V_s} - \vec{u}|\rho(1-\epsilon)}{d_s}\epsilon^{-2.7} & \text{if } \epsilon > 0.8 \end{cases}$$

$$C_D = \begin{cases} 24(1 + 0.15Re^{0.687})/Re & \text{if } Re < 1000 \\ 0.43 & \text{if } Re > 1000 \end{cases}$$

Where d_s is the particle diameter, μ the dynamic viscosity, $\vec{V_s}$ is the particle velocity and Re is the Reynolds number, expressed as :

$$Re = |\vec{V} - \vec{u}|\rho\epsilon d_s/\mu \tag{VI.21}$$

Closure laws can be developed at the micro-scale from particle resolved simulations and correlations representing the effective particle-fluid interactions can be used to improve the meso-scale description.

Bibliography

M. A. Abul-Hamayel. Kinetic modeling of high-severity fluidized catalytic cracking. *Fuel*, 82(9):1113–1118, 2003.

G. Akiki, T. Jackson, and S. Balachandar. Pairwise interaction extended point-particle model for a random array of monodisperse spheres. *Journal of Fluid Mechanics*, 813:882–928, 2017.

H. Alvarez-Castro, E. Matos, M. Mori, W. Martignoni, and R. Ocone. The influence of the fluidization velocities on products yield and catalyst residence time in industrial risers. *Advanced Powder Technology*, 26(3):836–847, 2015.

T. B. Anderson and R. Jackson. Fluid mechanical description of fluidized beds. equations of motion. *Industrial & Engineering Chemistry Fundamentals*, 6(4):527–539, 1967.

F. Augier, F. Idoux, and J.-Y. Delenne. Numerical simulations of transfer and transport properties inside packed beds of spherical particles. *Chemical Engineering Science*, 65(3):1055–1064, 2010a.

F. Augier, A. Koudil, A. Royon-Lebeaud, L. Muszynski, and Q. Yanouri. Numerical approach to predict wetting and catalyst efficiencies inside trickle bed reactors. *Chemical Engineering Science*, 65(1):255–260, 2010b.

D. Baruah and D. Baruah. Modeling of biomass gasification: a review. *Renewable and Sustainable Energy Reviews*, 39:806–815, 2014.

D. Baruah, D. Baruah, and M. Hazarika. Artificial neural network based modeling of biomass gasification in fixed bed downdraft gasifiers. *Biomass and Bioenergy*, 98(Supplement C):264 – 271, 2017. ISSN 0961-9534. doi: https://doi.org/10.1016/j.biombioe.2017.01.029. URL http://www.sciencedirect.com/science/article/pii/S0961953417300569.

L. L. Baxter. Ash deposition during biomass and coal combustion: a mechanistic approach. *Biomass and Bioenergy*, 4(2):85–102, 1993.

S. Bellan, N. Gokon, K. Matsubara, H. S. Cho, and T. Kodama. Heat transfer analysis of 5kw th circulating fluidized bed reactor for solar gasification using concentrated xe light radiation. *Energy*, 2018.

R. B. Bird, W. E. Stewart, E. N. Lightfoot, and D. J. Klingenberg. *Transport phenomena*. Wiley, 2 edition, 2015. ISBN 13: 978-0470115398.

K. Bizon. Steady-state characteristics of autothermal structures with fluidized-bed catalytic reactors. *Chemical Engineering Journal*, 321:286–300, 2017.

C. Bohn, S. A. Scott, J. S. Dennis, and C. Müller. Validation of a lattice boltzmann model for gas–solid reactions with experiments. *Journal of Computational Physics*, 231(16):5334–5350, 2012.

R. Boom, T. Van den Boomgaard, and C. Smolders. Mass transfer and thermodynamics during immersion precipitation for a two-polymer system: evaluation with the system pes—pvp—nmp—water. *Journal of membrane science*, 90(3): 231–249, 1994.

A. Bridgwater. The technical and economic feasibility of biomass gasification for power generation. *Fuel*, 74(5):631–653, 1995.

I. Calmet and J. Magnaudet. Large-eddy simulation of high-schmidt number mass transfer in a turbulent channel flow. *Physics of Fluids*, 9(2):438–455, 1997.

J. Chang, W. Cai, K. Zhang, F. Meng, L. Wang, and Y. Yang. Computational investigation of the hydrodynamics, heat transfer and kinetic reaction in an fcc gasoline riser. *Chemical Engineering Science*, 111:170–179, 2014.

S. Chen, Y. Fan, Z. Yan, W. Wang, X. Liu, and C. Lu. Cfd optimization of feedstock injection angle in a fcc riser. *Chemical Engineering Science*, 153:58–74, 2016a.

S. Chen, Y. Fan, Z. Yan, W. Wang, and C. Lu. Cfd simulation of gas–solid two-phase flow and mixing in a fcc riser with feedstock injection. *Powder Technology*, 287:29–42, 2016b.

T. H. Chilton and A. P. Colburn. Mass transfer (absorption) coefficients prediction from data on heat transfer and fluid friction. *Industrial & engineering chemistry*, 26(11):1183–1187, 1934.

R. Clift, J. R. Grace, and M. E. Weber. *Bubbles, drops, and particles.* Courier Corporation, 2005.

P. A. Cundall and O. D. Strack. A discrete numerical model for granular assemblies. *geotechnique*, 29(1):47–65, 1979.

C. Dan and A. Wachs. Direct numerical simulation of particulate flow with heat transfer. *International Journal of Heat and Fluid Flow*, 31(6):1050–1057, 2010.

N. G. Deen, E. Peters, J. T. Padding, and J. Kuipers. Review of direct numerical simulation of fluid–particle mass, momentum and heat transfer in dense gas–solid flows. *Chemical Engineering Science*, 116:710–724, 2014.

J. Derksen. Simulations of solid–liquid mass transfer in fixed and fluidized beds. *Chemical Engineering Journal*, 255:233–244, 2014.

A. Dey, T. Bhattacharyya, and S. Dhara. Characterization of hot rolled scales-root cause identification and remedial action. *Engineering Failure Analysis*, 34: 478–487, 2013.

F. Dierich, A. Richter, and P. Nikrityuk. A fixed-grid model to track the interface and porosity of a chemically reacting moving char particle. *Chemical Engineering Science*, 175:296–305, 2018.

A. G. Dixon, M. E. Taskin, M. Nijemeisland, and E. H. Stitt. Cfd method to couple three-dimensional transport and reaction inside catalyst particles to the fixed bed flow field. *Industrial & Engineering Chemistry Research*, 49(19):9012–9025, 2010.

F. Dorai, C. Moura Teixeira, M. Rolland, E. Climent, M. Marcoux, and A. Wachs. Fully resolved simulations of the flow through a packed bed of cylinders: Effect of size distribution. *Chemical Engineering Science*, 129:180–192, 2015.

F. Duarte, R. Gormaz, and S. Natesan. Arbitrary lagrangian–eulerian method for navier–stokes equations with moving boundaries. *Computer Methods in Applied Mechanics and Engineering*, 193(45-47):4819–4836, 2004.

S. Dunn, E. Nenniger, and V. Rajan. A study of bitumen recovery by gravity drainage using low temperature soluble gas injection. *The Canadian Journal of Chemical Engineering*, 67(6):978–991, 1989.

X. Dupain, M. Makkee, and J. Moulijn. Optimal conditions in fluid catalytic cracking: A mechanistic approach. *Applied Catalysis A: General*, 297(2):198–219, 2006.

A. Džiugys and B. Peters. An approach to simulate the motion of spherical and non-spherical fuel particles in combustion chambers. *Granular matter*, 3(4):231–266, 2001.

F. Euzenat. *Simulation numérique directe et analyse des transferts de chaleur dans les lits de particules fixes et mobiles.* PhD thesis, IFP Energies nouvelles, 2017.

R. P. Fedkiw, T. Aslam, B. Merriman, and S. Osher. A non-oscillatory eulerian approach to interfaces in multimaterial flows (the ghost fluid method). *Journal of computational physics*, 152(2):457–492, 1999.

Z.-G. Feng and E. E. Michaelides. A numerical study on the transient heat transfer from a sphere at high reynolds and peclet numbers. *International Journal of Heat and Mass Transfer*, 43(2):219–229, 2000.

J. L. Fernandes, L. H. Domingues, C. I. Pinheiro, N. M. Oliveira, and F. R. Ribeiro. Influence of different catalyst deactivation models in a validated simulator of an industrial uop fcc unit with high-efficiency regenerator. *Fuel*, 97:97–108, 2012.

S. Furuta, H. Matsuhashi, and K. Arata. Biodiesel fuel production with solid amorphous-zirconia catalysis in fixed bed reactor. *Biomass and Bioenergy*, 30 (10):870–873, 2006.

J. Gao, Z. Hou, J. Guo, Y. Zhu, and X. Zheng. Catalytic conversion of methane and co2 to synthesis gas over a la2o3-modified sio2 supported ni catalyst in fluidized-bed reactor. *Catalysis today*, 131(1-4):278–284, 2008.

F. Gibou, R. P. Fedkiw, L.-T. Cheng, and M. Kang. A second-order-accurate symmetric discretization of the poisson equation on irregular domains. *Journal of Computational Physics*, 176(1):205–227, 2002.

F. Gibou, R. Fedkiw, R. Caflisch, and S. Osher. A level set approach for the numerical simulation of dendritic growth. *Journal of Scientific Computing*, 19 (1-3):183–199, 2003.

D. Gidaspow. *Multiphase flow and fluidization: continuum and kinetic theory descriptions*. Academic press, 1994.

R. Glowinski, T.-W. Pan, T. I. Hesla, and D. D. Joseph. A distributed lagrange multiplier/fictitious domain method for particulate flows. *International Journal of Multiphase Flow*, 25(5):755–794, 1999.

R. Glowinski, T. Pan, T. Hesla, D. Joseph, and J. Periaux. A fictitious domain approach to the direct numerical simulation of incompressible viscous flow past moving rigid bodies: application to particulate flow. *Journal of Computational Physics*, 169(2):363–426, 2001.

D. Gunn. Transfer of heat or mass to particles in fixed and fluidised beds. *International Journal of Heat and Mass Transfer*, 21(4):467–476, 1978.

Y. Hamedi Shokrlu, T. Babadagli, et al. Effects of nano-sized metals on viscosity reduction of heavy oil/bitumen during thermal applications. In *Canadian Unconventional Resources and International Petroleum Conference*. Society of Petroleum Engineers, 2010.

Y. Haroun, D. Legendre, and L. Raynal. Volume of fluid method for interfacial reactive mass transfer: application to stable liquid film. *Chemical Engineering Science*, 65(10):2896–2909, 2010.

J. Hernandez, G. Pavon, and M. Garcıa. Analytical solution of mass transfer equation considering shrinkage for modeling food-drying kinetics. *Journal of food engineering*, 45(1):1–10, 2000.

K. Hou and R. Hughes. The effect of external mass transfer, competitive adsorption and coking on hydrogen permeation through thin pd/ag membranes. *Journal of Membrane Science*, 206(1):119–130, 2002.

H. H. Hu, N. A. Patankar, and M. Zhu. Direct numerical simulations of fluid–solid systems using the arbitrary lagrangian–eulerian technique. *Journal of Computational Physics*, 169(2):427–462, 2001.

K. N. Islam, J. Hildenbrand, and M. M. Hossain. Life cycle impacts of three-way ceramic honeycomb catalytic converter in terms of disability adjusted life year. *Journal of Cleaner Production*, 182:600–615, 2018.

T. M. Ismail, M. A. El-Salam, E. Monteiro, and A. Rouboa. Fluid dynamics model on fluidized bed gasifier using agro-industrial biomass as fuel. *Waste Management*, 2017. ISSN 0956-053X. doi: https://doi.org/10.1016/j.wasman.2017.06.018. URL http://www.sciencedirect.com/science/article/pii/S0956053X17304592.

A. T. Jarullah, N. A. Awad, and I. M. Mujtaba. Optimal design and operation of an industrial fluidized catalytic cracking reactor. *Fuel*, 206:657–674, 2017.

M. Jeremiáš, M. Pohořelỳ, K. Svoboda, S. Skoblia, Z. Beňo, and M. Šyc. Co 2 gasification of biomass: The effect of lime concentration in a fluidised bed. *Applied Energy*, 217:361–368, 2018.

Y. M. John, R. Patel, and I. M. Mujtaba. Effects of compressibility factor on fluid catalytic cracking unit riser hydrodynamics. *Fuel*, 223:230–251, 2018.

G. Juncu. The influence of the henry number on the conjugate mass transfer from a sphere. *Heat and mass transfer*, 37(4):519–530, 2001.

G. Juncu. The influence of the henry number on the conjugate mass transfer from a sphere: Ii–mass transfer accompanied by a first-order chemical reaction. *Heat and Mass Transfer*, 38(6):523–534, 2002.

M. Kaewpanha, G. Guan, X. Hao, Z. Wang, Y. Kasai, K. Kusakabe, and A. Abudula. Steam co-gasification of brown seaweed and land-based biomass. *Fuel Processing Technology*, 120:106–112, 2014.

M. Kang, R. P. Fedkiw, and X.-D. Liu. A boundary condition capturing method for multiphase incompressible flow. *Journal of Scientific Computing*, 15(3):323–360, 2000.

A. Kapahi, J. Mousel, S. Sambasivan, and H. Udaykumar. Parallel, sharp interface eulerian approach to high-speed multi-material flows. *Computers & Fluids*, 83: 144–156, 2013.

R. H. Khiabani, Y. Joshi, and C. K. Aidun. Heat transfer in microchannels with suspended solid particles: lattice-boltzmann based computations. *Journal of Heat Transfer*, 132(4):041003, 2010.

L. S. Kleinman and X. J. Reed. Interphase mass transfer from bubbles, drops, and solid spheres: diffusional transport enhanced by external chemical reaction. *Industrial & engineering chemistry research*, 34(10):3621–3631, 1995.

S. Kraft, F. Kirnbauer, and H. Hofbauer. Influence of drag laws on pressure and bed material recirculation rate in a cold flow model of an 8 mw dual fluidized bed system by means of cpfd. *Particuology*, 36:70–81, 2018.

H. Kruggel-Emden, B. Kravets, M. Suryanarayana, and R. Jasevicius. Direct numerical simulation of coupled fluid flow and heat transfer for single particles and particle packings by a lbm-approach. *Powder Technology*, 294:236–251, 2016.

D. Kunii and O. Levenspiel. *Fluidization engineering*. Elsevier, 2013.

C. O. Lemos, L. L. Rade, M. A. d. S. Barrozo, L. Cardozo-Filho, and C. E. Hori. Study of glycerol etherification with ethanol in fixed bed reactor under high pressure. *Fuel Processing Technology*, 178:1–6, 2018.

R. Li, C. Wang, P. Wang, and J. Pei. Preparation of a novel flow improver and its viscosity-reducing effect on bitumen. *Fuel*, 181:935–941, 2016.

W. Li, Y. Zhang, Y. Shao, and J. Zhu. A rigorous model for the simulation of chemical reaction in gas-particle bubbling fluidized bed: I. modeling and validation. *Powder Technology*, 327:399–407, 2018.

H. Liu, S. Krishnan, S. Marella, and H. Udaykumar. Sharp interface cartesian grid method ii: A technique for simulating droplet interactions with surfaces of arbitrary shape. *Journal of Computational Physics*, 210(1):32–54, 2005.

X.-D. Liu, R. P. Fedkiw, and M. Kang. A boundary condition capturing method for poisson's equation on irregular domains. *Journal of computational Physics*, 160(1):151–178, 2000.

M. W. Losey, M. A. Schmidt, and K. F. Jensen. Microfabricated multiphase packed-bed reactors: characterization of mass transfer and reactions. *Industrial & engineering chemistry research*, 40(12):2555–2562, 2001.

J. Lu, S. Das, E. Peters, and J. Kuipers. Direct numerical simulation of fluid flow and mass transfer in dense fluid-particle systems with surface reactions. *Chemical Engineering Science*, 176:1–18, 2018.

Y. R. Lu and P. Nikrityuk. A fixed-bed reactor for energy storage in chemicals (e2c): Proof of concept. *Applied Energy*, 228:593–607, 2018.

J. Magnaudet, M. Rivero, and J. Fabre. Accelerated flows past a rigid sphere or a spherical bubble. part 1. steady straining flow. *Journal of fluid mechanics*, 284: 97–135, 1995.

S. Marella, S. Krishnan, H. Liu, and H. Udaykumar. Sharp interface cartesian grid method i: an easily implemented technique for 3d moving boundary computations. *Journal of Computational Physics*, 210(1):1–31, 2005.

J. C. Maxwell, W. Garnett, and P. Pesic. *An elementary treatise on electricity*. Courier Corporation, 2005.

R. Mikulandrić, D. Böhning, R. Böhme, L. Helsen, M. Beckmann, and D. Lončar. Dynamic modelling of biomass gasification in a co-current fixed bed gasifier. *Energy Conversion and Management*, 125(Supplement C):264 – 276, 2016. ISSN 0196-8904. doi: https://doi.org/10.1016/j.enconman.2016.04.067. URL http://www.sciencedirect.com/science/article/pii/S019689041630317X. Sustainable development of energy, water and environment systems for future energy technologies and concepts.

C. Montero, A. Remiro, P. L. Benito, J. Bilbao, and A. G. Gayubo. Optimum operating conditions in ethanol steam reforming over a ni/la 2 o 3-αal 2 o 3 catalyst in a fluidized bed reactor. *Fuel Processing Technology*, 169:207–216, 2018.

D. Y. Murzin and T. Salmi. *Catalytic kinetics*. Elsevier, 2005.

S. Mutyala, C. Fairbridge, J. J. Paré, J. M. Bélanger, S. Ng, and R. Hawkins. Microwave applications to oil sands and petroleum: A review. *Fuel Processing Technology*, 91(2):127–135, 2010.

S. N. Naik, V. V. Goud, P. K. Rout, and A. K. Dalai. Production of first and second generation biofuels: a comprehensive review. *Renewable and sustainable energy reviews*, 14(2):578–597, 2010.

D. Neves, A. Matos, L. Tarelho, H. Thunman, A. Larsson, and M. Seemann. Volatile gases from biomass pyrolysis under conditions relevant for fluidized bed gasifiers. *Journal of Analytical and Applied Pyrolysis*, 127(Supplement C):57 – 67, 2017. ISSN 0165-2370. doi: https://doi.org/10.1016/j.jaap.2017.09.002. URL http://www.sciencedirect.com/science/article/pii/S0165237017305090.

C. Ozhan, D. Fuster, and P. Da Costa. Multi-scale flow simulation of automotive catalytic converters. *Chemical Engineering Science*, 116:161–171, 2014.

B. Partopour and A. Dixon. An integrated workflow for resolved-particle packed bed models with complex particle shapes. *Powder Technology*, 322:258–272, 2017a.

B. Partopour and A. G. Dixon. Resolved-pore simulation of co oxidation on rh/al2o3 in a catalyst layer. *ChemEngineering*, 2(1):2, 2017b.

S. Piché, B. P. Grandjean, I. Iliuta, and F. Larachi. Interfacial mass transfer in randomly packed towers: a confident correlation for environmental applications. *Environmental science & technology*, 35(24):4817–4822, 2001.

F. Pigeonneau, M. Perrodin, and E. Climent. Mass-transfer enhancement by a reversible chemical reaction across the interface of a bubble rising under stokes flow. *AIChE Journal*, 60(9):3376–3388, 2014.

O. Plumb, G. Spolek, and B. Olmstead. Heat and mass transfer in wood during drying. *International Journal of Heat and Mass Transfer*, 28(9):1669–1678, 1985.

Z. Qi and E. Cussler. Microporous hollow fibers for gas absorption: I. mass transfer in the liquid. *Journal of membrane science*, 23(3):321–332, 1985.

Y. Qin, X. Gao, H. Zhang, S. Zhang, L. Zheng, Q. Li, Z. Mo, L. Duan, X. Zhang, and L. Song. Measurements and distinguishment of mass transfer processes in fluid catalytic cracking catalyst particles by uptake and frequency response methods. *Catalysis Today*, 245:147–154, 2015.

M. Qtaishat, T. Matsuura, B. Kruczek, and M. Khayet. Heat and mass transfer analysis in direct contact membrane distillation. *Desalination*, 219(1-3):272–292, 2008.

S. Radl, F. Municchi, S. Cloete, J. H. Cloete, S. Andersson, J. F. Morgado, T. Gurker, R. Q. Ferreira, C. Kloss, C. Goniva, et al. Closure development for multi-scale fluidized bed reactor models: A clr case study. 2018.

M. Rahmani and A. Wachs. Free falling and rising of spherical and angular particles. *Physics of Fluids*, 26(8):083301, 2014.

A. D. Rakotonirina and A. Wachs. Grains3d, a flexible dem approach for particles of arbitrary convex shape-part ii: Parallel implementation and scalable performance. *Powder Technology*, 324:18–35, 2018.

A. D. Rakotonirina, J.-Y. Delenne, F. Radjai, and A. Wachs. Grains3d, a flexible dem approach for particles of arbitrary convex shape—part iii: extension to non-convex particles modelled as glued convex particles. *Computational Particle Mechanics*, pages 1–30, 2018.

R. Ramachandran, C. Kleinstreuer, and T.-Y. Wang. Forced convection heat transfer of interacting spheres. *Numerical heat transfer*, 15(4):471–487, 1989.

W. Ranz, W. Marshall, et al. Evaporation from drops. *Chem. Eng. Prog*, 48(3): 141–146, 1952.

A. Reuvers, J. Van den Berg, and C. Smolders. Formation of membranes by means of immersion precipitation: Part i. a model to describe mass transfer during immersion precipitation. *Journal of membrane science*, 34(1):45–65, 1987.

D. J. Roddy and C. Manson-Whitton. Biomass gasification and pyrolysis. *Applied Energy*, 2012.

S. Romkes, F. Dautzenberg, C. Van den Bleek, and H. Calis. Cfd modelling and experimental validation of particle-to-fluid mass and heat transfer in a packed bed at very low channel to particle diameter ratio. *Chemical Engineering Journal*, 96 (1-3):3–13, 2003.

I. Rossetti. Continuous flow (micro-) reactors for heterogeneously catalyzed reactions: Main design and modelling issues. *Catalysis Today*, 2017.

E. Ruckenstein, V.-D. Dang, and W. N. Gill. Mass transfer with chemical reaction from spherical one or two component bubbles or drops. *Chemical Engineering Science*, 26(5):647–668, 1971.

S. G. Sahu, N. Chakraborty, and P. Sarkar. Coal–biomass co-combustion: An overview. *Renewable and Sustainable Energy Reviews*, 39:575–586, 2014.

R. Schofield, A. Fane, and C. Fell. Heat and mass transfer in membrane distillation. *Journal of Membrane Science*, 33(3):299–313, 1987.

J. Seader, E. J. Henley, and D. Keith. Roper. separation process principles: Chemical and biochemical operations, 2011.

M. T. Shah, V. K. Pareek, G. M. Evans, and R. P. Utikar. Effect of baffles on performance of fluid catalytic cracking riser. *Particuology*, 38:18–30, 2018.

X. Shao, Y. Shi, and Z. Yu. Combination of the fictitious domain method and the sharp interface method for direct numerical simulation of particulate flows with heat transfer. *International Journal of Heat and Mass Transfer*, 55(23): 6775–6785, 2012.

T. Sherwood and J. Wei. Interfacial phenomena in liquid extraction. *Industrial & Engineering Chemistry*, 49(6):1030–1034, 1957.

Y. Shi, Z. Yu, and X. Shao. Combination of the direct-forcing fictitious domain method and the sharp interface method for the three-dimensional dielectrophoresis of particles. *Powder technology*, 210(1):52–59, 2011.

Y. H. Shokrlu and T. Babadagli. Viscosity reduction of heavy oil/bitumen using micro-and nano-metal particles during aqueous and non-aqueous thermal applications. *Journal of Petroleum Science and Engineering*, 119:210–220, 2014.

R. Singh and E. Gbordzoe. Modeling fcc spent catalyst regeneration with computational fluid dynamics. *Powder Technology*, 316:560–568, 2017.

L. Song, Z. Sun, L. Duan, J. Gui, and G. S. McDougall. Adsorption and diffusion properties of hydrocarbons in zeolites. *Microporous and Mesoporous Materials*, 104(1-3):115–128, 2007.

M. Sulaiman, E. Climent, A. Hamoutti, and A. Wachs. Mass transfer towards a reactive particle in a fluid flow : numerical simulations and modeling. *Chemical Engineering Science*, 65(3):1055–1064, 2018a.

M. Sulaiman, A. Hamoutti, E. Climent, and A. Wachs. Coupling the fictitious domain and sharp interface methods for the simulation of convective mass transfer around reactive particles: towards a reactive sherwood number correlation for dilute systems. *Chemical Engineering Science*, 2(3):1055–1064, May 2018b.

B. Sun, S. Tenneti, and S. Subramaniam. Modeling average gas–solid heat transfer using particle-resolved direct numerical simulation. *International Journal of Heat and Mass Transfer*, 86:898–913, 2015.

B. Sun, S. Tenneti, S. Subramaniam, and D. L. Koch. Pseudo-turbulent heat flux and average gas–phase conduction during gas–solid heat transfer: flow past random fixed particle assemblies. *Journal of Fluid Mechanics*, 798:299–349, 2016.

S. Sundaram and L. R. Collins. Numerical considerations in simulating a turbulent suspension of finite-volume particles. *Journal of Computational Physics*, 124(2): 337–350, 1996.

M. Tatlıer, B. Tantekin-Ersolmaz, and A. Erdem-Şenatalar. A novel approach to enhance heat and mass transfer in adsorption heat pumps using the zeolite–water pair. *Microporous and Mesoporous Materials*, 27(1):1–10, 1999.

H. Tavassoli, S. Kriebitzsch, M. Van der Hoef, E. Peters, and J. Kuipers. Direct numerical simulation of particulate flow with heat transfer. *International Journal of Multiphase Flow*, 57:29–37, 2013.

E. W. Thiele. Relation between catalytic activity and size of particle. *Industrial & Engineering Chemistry*, 31(7):916–920, 1939.

A. Tremel and H. Spliethoff. Gasification kinetics during entrained flow gasification–part i; devolatilisation and char deactivation. *Fuel*, 103:663–671, 2013.

Y. Tsuji, T. Kawaguchi, and T. Tanaka. Discrete particle simulation of two-dimensional fluidized bed. *Powder technology*, 77(1):79–87, 1993.

S. Turn, C. Kinoshita, Z. Zhang, D. Ishimura, and J. Zhou. An experimental investigation of hydrogen production from biomass gasification. *International Journal of Hydrogen Energy*, 23(8):641–648, 1998.

H. Udaykumar and L. Mao. Sharp-interface simulation of dendritic solidification of solutions. *International journal of heat and mass transfer*, 45(24):4793–4808, 2002.

M. Uhlmann. An immersed boundary method with direct forcing for the simulation of particulate flows. *Journal of Computational Physics*, 209(2):448–476, 2005.

M. A. van der Hoef, M. van Sint Annaland, and J. Kuipers. Computational fluid dynamics for dense gas–solid fluidized beds: a multi-scale modeling strategy. *Chemical Engineering Science*, 59(22-23):5157–5165, 2004.

M. A. van der Hoef, M. van Sint Annaland, N. Deen, and J. Kuipers. Numerical simulation of dense gas-solid fluidized beds: a multiscale modeling strategy. *Annu. Rev. Fluid Mech.*, 40:47–70, 2008.

D. K. Verma and K. d. Tombe. Benzene in gasoline and crude oil: occupational and environmental implications. *AIHA Journal*, 63(2):225–230, 2002.

R. Voncken, I. Roghair, and M. van Sint Annaland. Mass transfer phenomena in fluidized beds with horizontally immersed membranes: a numerical investigation. *Chemical Engineering Science*, 2018.

A. Wachs. Peligriff, a parallel dem-dlm/fd direct numerical simulation tool for 3d particulate flows. *Journal of Engineering Mathematics*, 71(1):131–155, 2011a.

A. Wachs. Rising of 3d catalyst particles in a natural convection dominated flow by a parallel dns method. *Computers & Chemical Engineering*, 35(11):2169–2185, 2011b.

A. Wachs, L. Girolami, G. Vinay, and G. Ferrer. Grains3d, a flexible dem approach for particles of arbitrary convex shape—part i: Numerical model and validations. *Powder technology*, 224:374–389, 2012.

A. Wachs, A. Hammouti, G. Vinay, and M. Rahmani. Accuracy of finite volume/staggered grid distributed lagrange multiplier/fictitious domain simulations of particulate flows. *Computers & Fluids*, 115:154–172, 2015.

N. Wakao and T. Funazkri. Effect of fluid dispersion coefficients on particle-to-fluid mass transfer coefficients in packed beds: correlation of sherwood numbers. *Chemical Engineering Science*, 33(10):1375–1384, 1978.

L. Wang, Q. Liu, C. Jing, J. Yin, N. Mominou, and S. Li. Simultaneous removal of sulfides and benzene in fcc gasoline by in situ hydrogenation over nilain/zro2-r-al2o3. *Journal of hazardous materials*, 342:758–769, 2018.

G. D. Wehinger, T. Eppinger, and M. Kraume. Detailed numerical simulations of catalytic fixed-bed reactors: Heterogeneous dry reforming of methane. *Chemical Engineering Science*, 122:197–209, 2015.

G. D. Wehinger, F. Klippel, and M. Kraume. Modeling pore processes for particle-resolved cfd simulations of catalytic fixed-bed reactors. *Computers & Chemical Engineering*, 101:11–22, 2017.

M. Wenzel, L. Rihko-Struckmann, and K. Sundmacher. Continuous production of co from co2 by rwgs chemical looping in fixed and fluidized bed reactors. *Chemical Engineering Journal*, 336:278–296, 2018.

S. Whitaker. Forced convection heat transfer correlations for flow in pipes, past flat plates, single cylinders, single spheres, and for flow in packed beds and tube bundles. *AIChE Journal*, 18(2):361–371, 1972.

J. C. Wurzenberger, S. Wallner, H. Raupenstrauch, and J. G. Khinast. Thermal conversion of biomass: Comprehensive reactor and particle modeling. *AIChE Journal*, 48(10):2398–2411, 2002.

J. Xia, K. Luo, and J. Fan. A ghost-cell based high-order immersed boundary method for inter-phase heat transfer simulation. *International Journal of Heat and Mass Transfer*, 75:302–312, 2014.

S. Yaghoobi-Khankhajeh, R. Alizadeh, and R. Zarghami. Adsorption modeling of co2 in fluidized bed reactor. *Chemical Engineering Research and Design*, 129: 111–121, 2018.

H. Yang and H. Chen. State key laboratory of coal combustion, huazhong university of science and technology, wuhan, pr china. *Gasification for Synthetic Fuel Production: Fundamentals, Processes and Applications*, page 241, 2014.

Z. Yu, X. Shao, and A. Wachs. A fictitious domain method for particulate flows with heat transfer. *Journal of Computational Physics*, 217(2):424–452, 2006.

B. Zhang, L. Zhang, Z. Yang, Y. Yan, G. Pu, and M. Guo. Hydrogen-rich gas production from wet biomass steam gasification with cao/mgo. *International Journal of Hydrogen Energy*, 40(29):8816–8823, 2015.

B. Zhang, Z. Zhong, J. Zhang, and R. Ruan. Catalytic fast co-pyrolysis of biomass and fusel alcohol to enhance aromatic hydrocarbon production over zsm-5 catalyst in a fluidized bed reactor. *Journal of Analytical and Applied Pyrolysis*, 133:147–153, 2018.